OPEN ACCESS Freely available online

PLoS one

Emergent Properties of Tumor Microenvironment in a Real-Life Model of Multicell Tumor Spheroids

Edoardo Milotti[1,2]*, Roberto Chignola[2,3]

1 Dipartimento di Fisica, Università di Trieste, Trieste, Italy, 2 I.N.F.N.-Sezione di Trieste, Trieste, Italy, 3 Dipartimento di Biotecnologie, Università di Verona, Verona, Italy

Abstract

Multicellular tumor spheroids are an important in vitro model of the pre-vascular phase of solid tumors, for sizes well below the diagnostic limit: therefore a biophysical model of spheroids has the ability to shed light on the internal workings and organization of tumors at a critical phase of their development. To this end, we have developed a computer program that integrates the behavior of individual cells and their interactions with other cells and the surrounding environment. It is based on a quantitative description of metabolism, growth, proliferation and death of single tumor cells, and on equations that model biochemical and mechanical cell-cell and cell-environment interactions. The program reproduces existing experimental data on spheroids, and yields unique views of their microenvironment. Simulations show complex internal flows and motions of nutrients, metabolites and cells, that are otherwise unobservable with current experimental techniques, and give novel clues on tumor development and strong hints for future therapies.

Citation: Milotti E, Chignola R (2010) Emergent Properties of Tumor Microenvironment in a Real-Life Model of Multicell Tumor Spheroids. PLoS ONE 5(11): e13942. doi:10.1371/journal.pone.0013942

Editor: Terence Lee, University of Hong Kong, China

Received July 16, 2010; Accepted October 8, 2010; Published November 30, 2010

Funding: This work has been supported by the Italian Institute for Nuclear Physics (INFN) under the names VIRTUS, VBL and VBL-Rad. Relevant information can be found on the INFN website, http://www.infn.it/indexen.php. The funder had no role in study design, data collection and analysis, decision to publish, or preparation of the manuscript.

Competing Interests: The authors have declared that no competing interests exist.

* E-mail: edoardo.milotti@ts.infn.it

Introduction

Multicellular tumor spheroids (MTS) stand out as the most important in vitro model of pre-vascular solid tumors [1–8]. MTS often have a regular, almost spherical structure, and their apparent simplicity has led to repeated attempts to capture their features with neat mathematical models. However, the absence of vascularization and the near sphericity hide an internal complexity which is not easy to tame either with analytic mathematical models [9–12], or with numerical models based on rough simplifications of the biological settings such as cellular automata or other lattice-based models [13–16]. Moreover the presence of a growing necrotic core [1] and of an extracellular matrix [17], the appearance of convective cell motions [18], and the heterogeneous response to chemotherapics [19], point to the importance of MTS as an in vitro model of tumors, and most of all to their relevance to understand tumor heterogeneity, but they also point to the difficulties of producing a useful, predictive model of MTS.

The appearance of widely different resistance phenomena to antitumor therapies in similarly grown, isolated MTS of the same cell type [19] indicates that random fluctuation phenomena play an all-important role in the growth kinetics of MTS. It is well-known that the discrete events at the single-cell level (like transitions from one cell-cycle phase to the next, mitosis, cell death, etc.) do display some randomness, and one can pinpoint the source of large-scale variability on these fluctuations, as they are amplified and propagated by cell-cell and cell-environment interactions. Thus, the complexity of MTS development can only be captured by a fine-grained, multiscale model, and we need a mathematical description at the single-cell level. Since cells communicate with other cells and the environment, the other actors of this complex play are the concentration gradients of important molecular species that depend on the structure of the extracellular space and of the facilitated transport processes into and out of individual cells, and the mechanical forces that push and pull cells as they proliferate with repeated mitoses and then shrink after death [20]. These processes mix with complex nonlinear interactions between the biochemical and the mechanical part, and this highlights again the importance of an effective model at the single-cell level.

On the basis of such motivations, we have developed a numerical model of MTS that incorporates a working model of single cells [21,22]. We have first put forward a broad outline of its structure in reference [23], and it differs from other models developed in the past [9–16] because it captures at the same time both the basic features of cell metabolism, growth, proliferation and death, and provides a true lattice-free calculation of cell motions, as they are pushed and pulled by the forces exerted by dividing cells, by the growth of other cells, and by the shrinking of dead cells. We also wish to stress that the model parameters are either derived from experiment or are deduced from reasonable theoretical arguments, so that, essentially, there are no free parameters – there can only be some residual variability in biophysically meaningful ranges – the model is truly predictive, and the results are not merely qualitative but quantitative as well.

Here we illustrate in broad terms the structure of the program and report the results of the first simulations of single spheroids (technical implementation details are relegated to Text S1). We find that the simulations agree quite well with experimental measurements on real spheroids, and show unexpected and

important internal patterns. Moreover, we wish to stress that the methods delineated in this paper represent very general practical solutions to problems that are common to any simulation of cell clusters, and they are just as important.

Biochemical behavior of individual cells

The elementary building blocks in this model of MTS are the individual tumor cells that behave as partly stochastic automata [21,22]. Figure 1 summarizes the biochemical pathways that are included in the single-cell model: cell metabolism is driven by oxygen, glucose and glutamine, and transforms these substances into energy molecules, molecular building blocks and waste products, following the well-known biochemical reaction chains [24]. Further details can be found in the original papers [21,22] and in Text S1, which also includes important upgrades to the original model [21,22].

In the present version of the program, the stochasticity is mostly concentrated in the discrete events: for instance, mitochondria are partitioned at random between daughter cells at mitosis, and cells can die because of metabolite accretion, according to a Poissonian cytotoxicity model (see Text S1).

We remark that in this approach glutamine also stands for the wider class of aminoacids, and lactate is the paradigm of all metabolites: we use the concentrations of glutamine and lactate to represent these two classes of substances in phenomenological parameterizations wherever needed. Similarly we use the number of mitochondria and ATP content to model the dynamics of cell volume; the single-cell model also contains representative members of the cyclin protein class to compute the passage of checkpoints and entry into the different cell phases [21,22,25,26], and finally into mitosis (see also figure S1 for a sketch of the cell cycle in the simulation program).

The complete map of the biochemical pathways included in the simulation program is shown in figure S2. This map comprises only the most basic pathways, however we cannot afford to introduce a more complex network at this stage of program development. Indeed, our final aim is the simulation of MTS with a volume as large as 1 mm^3, which corresponds to more than one million cells, so that simulation results overlap actual experimental measurements [19,27,28]. Since the differential system involves 19 independent biochemical variables per cell, we must eventually integrate at least 19 million coupled nonlinear differential equations for the biochemical cell variables alone (this grows to at least 25 million equations when we include the position and velocity variables), and thus even this minimal single-cell model leads to a daunting computational task (see Text S1 for further details on the algorithmic complexity of the program).

Reaction-diffusion processes and the environment

Substances like oxygen are transported into and out of cells by normal diffusion while molecules like glucose require facilitated diffusion processes. This means that cell membranes play an important role for substances like glucose, and that in this case the diffusion of each such molecular species towards cells in the inside of a spheroid needs the free volume in the extracellular space to proceed, and that we must model this space as well as the cells to obtain a realistic simulation. We have shown how to do this in reference [29], where we have also discussed ways to tame the

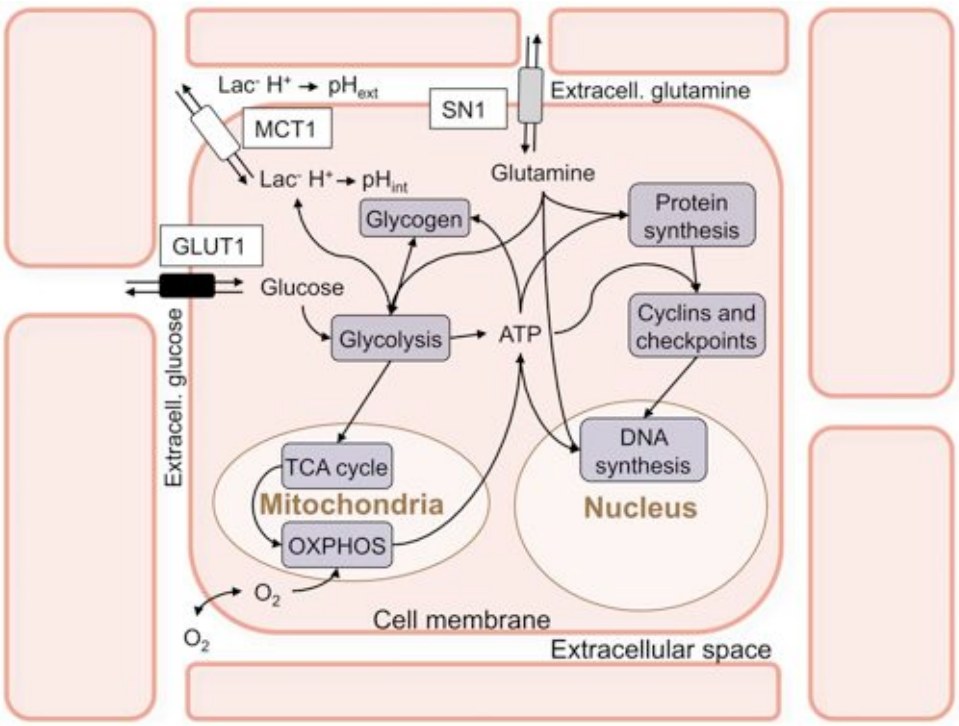

Figure 1. Rough sketch of the biochemical pathways incorporated in the model of single cells. We take into account the main metabolic pathways (glycolysis, oxidative phosphorylation through the TCA cycle and gluconeogenesis), including the role of mitochondria in the production of ATP. The model also includes protein and DNA synthesis, and checkpoints controlled by representative members of the cyclin family. The single-cell model has two spatial compartments (the inside of the cell and its immediate neighborhood, the extracellular space that surrounds it) and transport of substances between these compartments is regulated by transporters on the cell membrane that are also included in the model. The extracellular space of each cell communicates by simple diffusion with the neighboring extracellular spaces and with the environment. The complete map of the biochemical pathways is shown in figure S2.
doi:10.1371/journal.pone.0013942.g001

exceedingly high stiffness of the very large set of reaction-diffusion and transport equations that arise in this context (see also Text S1). The external environment itself is included in these equations, and evolves in time as well. In the present model, each cell contributes 15 internal variables and 4 extracellular variables: these extracellular variables are the masses of oxygen, glucose, glutamine and lactate in the extracellular volume surrounding the cell. Because of its smallness, the extracellular space has an extremely short characteristic filling time, which can be as fast as few tens of microseconds. On the other hand, the macroscopic features of MTS evolve over times as long as months (i.e., times of the order of 10^7s), and thus the numerical integrator must be able to handle phenomena that span 12 orders of magnitude in time [29]. The internal biochemical reactions included in the numerical model are much slower and their fastest characteristic times are only as low as 0:1s, much longer than the diffusion times [29,30]. The topology of diffusion in the extracellular spaces is obviously dictated by the cells themselves, and the program uses the network of cells centers as the scaffolding for the corresponding discretized diffusion problem. The links between the cells' centers – i.e., the proximity relations – are provided by a Delaunay triangulation [31,32], which is computed repeatedly [33] as the cluster of cells grows and rearranges itself under the pushes and pulls of volume growth, mitosis, and the shrinking of dead cells (see also figure S3). Moreover, the proliferation of cells means that both the number of cells and the total number of links steadily grow, and that the differential system of equations that model metabolism, transport and diffusion changes all the time, and becomes increasingly complex. The 3D Delaunay triangulation itself is not an exceedingly heavy computational burden for the program, as it turns out that efficient algorithms can compute it, on average, with O(N) time computational complexity [33–35], so that this algorithm is indeed feasible for very large clusters of cells.

Biomechanical evolution of the simulated MTS

Real cells have passive viscoelastic mechanical features, but they also move actively under the pushes of their own cytoskeleton, and to the best of our knowledge there is no comprehensive model of cellular biomechanics [36,37]. Thus, we resort once again to phenomenological simplifications, and the first and foremost is that our cells are stretchable spheres, characterized by their radius, and a few other parameters that specify their viscoelastic properties (see Text S1 for a more detailed description and the list of parameters). We also specify a pairwise interaction force between cells, repulsive when a cell pushes against a neighbor, and attractive when we try to detach it from its neighbor. For small deviations from the equilibrium distance, we assume that the interaction force is described by the Hertz model (explained in Text S1), while for large deformations due to compression we set the force to a fixed saturation value, and for large distances the attractive force decays to zero (see figure S4). The description of the interaction forces is tuned to hold also during mitosis (see Text S1 and figure S5). Even though this is a rough approximation of the overall mechanical behavior of cells, there are many details that must be managed to make it work, and they are all described in Text S1.

Here the Delaunay triangulation that we use as the scaffolding for the diffusion problem turns out to be useful once again: the same cell-cell links also define the set of neighbors of each cell, and therefore the global problem of computing the pairwise interactions between cells can be reduced to a single loop over all cells and the small limited number of their immediate neighbors, so that this operation has an O(N) computational complexity only – and it does not grow when we include the cost of the Delaunay triangulation [35] – instead of the $O(N^2)$ complexity of generic pairwise interactions.

Results

The first and most obvious result is the outstanding match of the growth curves of simulated spheroids with those of real spheroids: figure 2 shows a few stages of the growth of a simulated spheroid (a real spheroid is shown for comparison in figure 3), while figure 4 compares the growth curve of a single simulated spheroid with the growth curves of real spheroids grown *in vitro*. Here we see that the growth curves are very much alike, and we found that simulation runs with different parameters – in the biophysically meaningful ranges – produce very similar growth curves, in spite of structural internal changes: the growth curves are thus rather robust with respect to parameter changes.

Several experiments [37–42] have yielded many accurate measurements of oxygen and glucose concentrations and other quantities vs. spheroid radius; these values are part of the output of our simulation program as well (see figure 5 and figure 6), and a comparison with the experimental data is shown in table 1. On the whole the agreement of simulation data of single spheroids with the experimental values is quite good, and we wish to stress that this is not the result of a fit *a posteriori*, but rather of the *a priori* choice of model features and parameters. These results qualify as true predictions of the numerical model.

The necrotic core of spheroids is another important feature that is well reproduced in the simulations, and it is clearly visible in central slices of the simulated spheroid in figure 2. The simulations also provide detailed, quantitative snapshots of the necrotic core dynamics; the left column of figure 7 shows the percentage of dead cells vs. distance from the centroid of a simulated spheroid at different times. In these snapshots we can clearly observe the formation of the sharp step that marks the edge of the necrotic core.

These results indicate that the simulation program is reliable and robust and reproduces – both quantitatively and qualitatively – known experimental results. However, it yields much more than just successful comparisons: figure 8 shows two views of the spheroid microenvironment that at present would be unobtainable by other means at this level of resolution. The left panel of figure 8 is a plot of the flow of glucose in the extracellular spaces of a mature spheroid, superposed on a density plot of extracellular glucose concentration, and it shows – rather unexpectedly – that there is an outward flow of extracellular glucose from the central necrotic region. In the external, viable rim the flow is inward bound, and there is a spherical shell where the flow is stationary. The right panel of figure 8 shows the corresponding plot of cell velocities in the same central slice, and we see that the velocity vectors point outward in the viable rim, while there are well-formed vortices in the central region, and the region in-between displays distinctive chaotic motions: these three regions closely match the three regions in the left panel. The right column in figure 7 shows radial velocity vs. distance from the centroid of the simulated spheroid, and sheds some more light on the nature of this structure: as more and more cells die and the necrotic core forms, the dead cells shrink and the core contracts. The contraction of the necrotic core expels the residual glucose in the extracellular spaces and produces the observed outward flow. We found that this behavior is strongly dependent on the particular value of the diffusion coefficient and on the metabolic activity of cells. In some simulations – where we used a lower value for the effective diffusion coefficient of oxygen – we observed a similar structure with oxygen as well. We remark that in the case

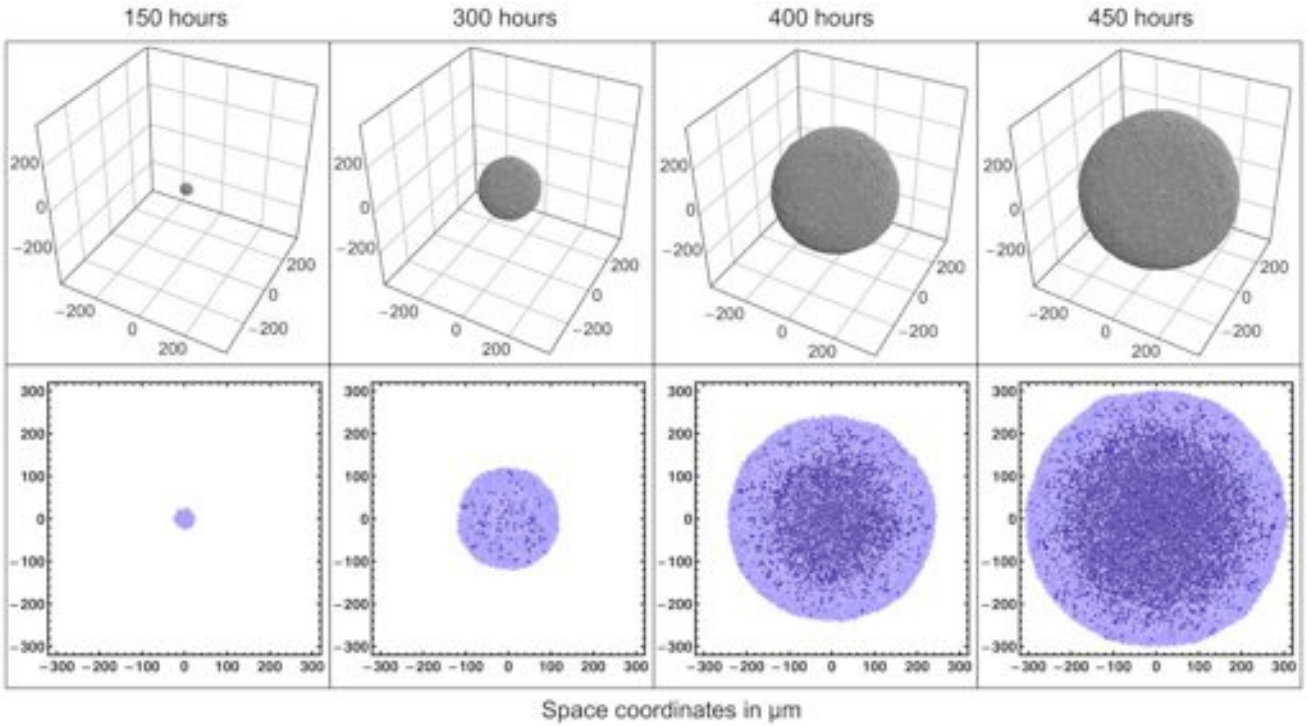

Figure 2. Snapshots of one simulated spheroid taken at different times. As the spheroid grows, a necrotic core develops in its central region, just as it happens in real spheroids. The size of the necrotic core and of the viable cell rim match real measurements.
doi:10.1371/journal.pone.0013942.g002

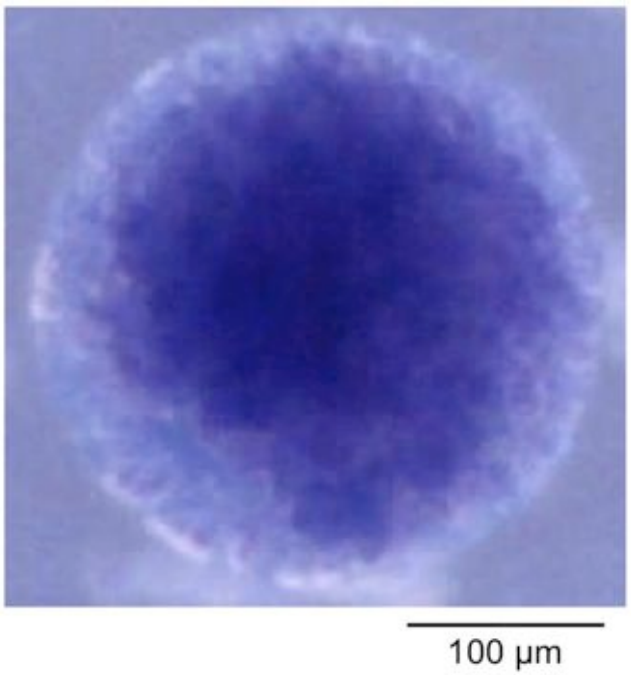

Figure 3. Photograph of a spheroid grown in vitro from HeLa cells in agar. The spheroid is colored with trypan blue to mark dead cells, where the necrotic core is clearly visible. The agar contains the spheroid and helps in obtaining a better spherical shape with HeLa cells, but also stifles spheroid growth because it reduces the effective diffusion coefficients in the nourishing medium, so that it cannot be directly compared to the simulated spheroid in the second column of figure 2 (which has the same size), while it is similar to the larger spheroid in third column.
doi:10.1371/journal.pone.0013942.g003

of lactate we found no such structure, and we obtained a pH value – derived from the distribution of lactate inside the spheroid – that is very close to experimental measurements: this indicates that the discretized reaction-diffusion scheme used in the simulation program performs correctly, and that the observed flows are not algorithmic artifacts.

Discussion

Although the program described in this paper is based on a model of individual cells that includes only the basic cell functions,

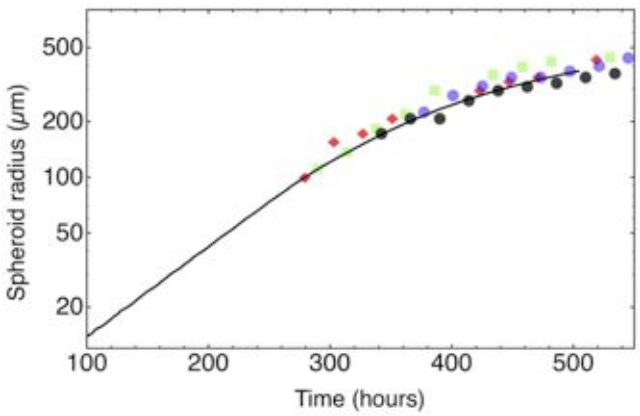

Figure 4. Growth curve of a simulated tumor spheroid (solid line). The run parameters used in this case are listed in Text S1. The symbols denote data points taken in different in vitro experiments: squares = FSA cells (methylcholantrene-transformed mouse fibroblasts) [45]; diamonds = MCF7 cells (human breast carcinoma) [19]; circles = 9L cells (rat glioblastoma) [27].
doi:10.1371/journal.pone.0013942.g004

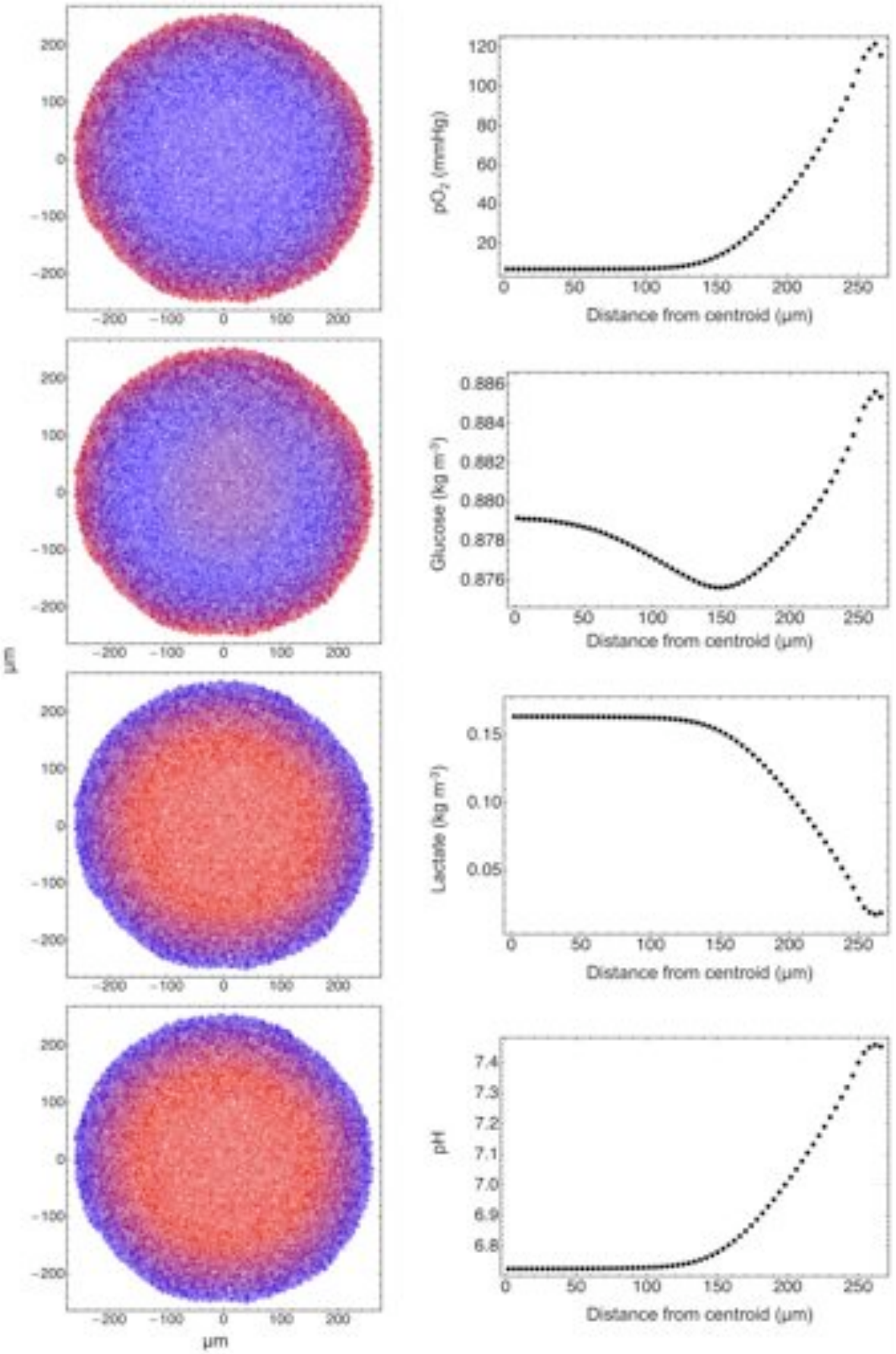
μm
μm
pO_2 (mmHg)
Distance from centroid (μm)
Glucose (kg m^{-3})
Distance from centroid (μm)
Lactate (kg m^{-3})
Distance from centroid (μm)
pH
Distance from centroid (μm)

Figure 5. Concentrations in the simulated spheroid. The color coded figures on the left show the partial pressure of oxygen, the concentrations of glucose and lactate in the extracellular spaces, and the pH of the extracellular environment (high values = red, low values = blue). The corresponding plots in the right column show the average values of these quantities vs. the distance from the centroid of the tumor spheroid. The small oscillations in the plots close to the spheroid surface are due to fluctuations in the averaging procedure, because the spheroid is slightly nonspherical.
doi:10.1371/journal.pone.0013942.g005

the simulation results compare very well with experimental measurements, and give strong hints on the sources of individual spheroid variability. Moreover, the images obtained in single runs reveal unexpected and interesting correlations and an elaborate structure of the tumor microenvironment that could never be observed before. This unexpected, complex microstructure – the formation of different regions, and the flows that characterize them, along with the complex velocity field – can be discerned in the flows of the other substances, though not all of them, according to their effective diffusion coefficient and their metabolism: the figures of these flows are shown at full-size as supporting information. Thus if we suppose that, in a more complete description, there are N substances that characterize the spheroid microenvironment, and assume that the spherical shell that divides the two main regions lies in the same position for all of these substances and that their effective diffusion coefficients are uncorrelated, then 2^N different spheroid structures are determined by diffusion alone. The variation of some critical parameter (e.g., a slight change in the metabolic activity due to local fluctuations in the number of dead cells, and thus a change in the effective diffusion coefficients) can potentially act as a switch and determine widely different fates for similar spheroids. This variability cannot be discerned from growth experiments: the simulations that we have performed to date indicate that the growth curve alone is not enough to distinguish between such different states, because it does not change much even when important substances, like oxygen, diffuse in markedly different ways. These different states represent different biochemical configurations of tumor microenvironment, that might exert distinct selective pressures on cells during tumor evolution.

The spheroid microstructure that is well evidenced in figure 8, and in figures S8, S9, S10, S11, S12, S13, S14, S15, S16, S17, S18, S19, S20, S21 and in Movies S1, S2, S3, shows highly correlated fluctuations that produce, e.g., islets of proliferating cells

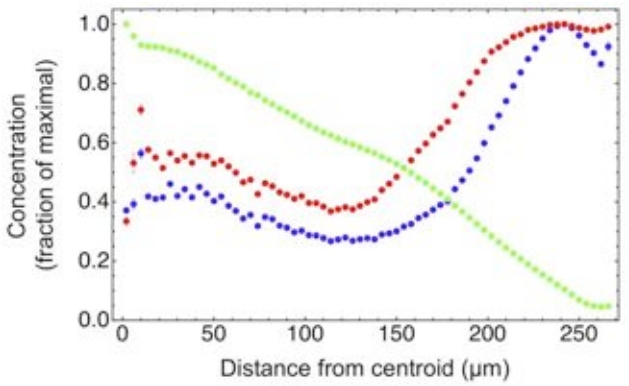

Figure 6. Plots of the normalized average intracellular concentration of lactate (green), glucose (blue), and ATP (red). These plots have been obtained in the same simulation and at the same time step as the plots of figure 5, and each concentration is normalized to its peak value. These plots indicate that cell death in the central region is due both to the accumulation of metabolites (lactate) and to metabolic stress (starvation).
doi:10.1371/journal.pone.0013942.g006

in the sea of dead cells of the core, and cell and mass flows that follow preferential channels. There is a sort of spheroid-specific self-organization of the internal structure due to these correlated fluctuations. Similar cell flows have been observed in the lab and a recent review has stressed the great significance of such findings [43]: the simulations suggest that the whole topic of cell flows and extracellular diffusion should be investigated further. On the basis of the simulation results, we also conjecture that the flow of therapeutic drugs may be diverted as well, and let some viable, proliferating tumor cells escape treatment. This means that the simulation program could eventually become an important tool to design novel treatment schedules, and possibly validate the effects of anti-tumor drugs.

Certainly the model is far from complete, and we plan to add soon several new features, like a basic model of intracellular acidity, now accounted for by a simple phenomenological parameterization, and the effects of pH and salt concentration on diffusion. However, already in its present form, we believe that this numerical model is a true testbed of biological complexity and a real virtual laboratory, and also a source of important biomedical clues.

Methods

The simulation program is written in ANSI C++: this programming language was a natural choice from the very start for distinct reasons:

- C++ is an object-oriented language, and in a simulation such as this, it is very natural to define objects that have a clear-cut biological meaning;
- at present, C++ programming is supported by a vast array of scientific libraries, and this helps reducing program development time;
- the availability of the flexible and powerful C++ library CGAL [33] that handles the computational geometry structures utilized by the program (convex hulls, Delaunay triangulations and alpha shapes);
- the availability of powerful development tools and highly optimized compilers.

The structure of the program reflects the organization explained in the paper: a layout is shown in figure 9. The functional blocks work as follows:

Initialization

At start, the environmental concentrations are set at their standard levels (see Text S1), and internal variables of all cells are set at approximate standard values (see Text S1 for the cells' variables and the physical values that are hard-coded in the program). During initialization, cells are allowed to grow and proliferate freely in an environment that is held fixed. The number of cells is also kept constant, and when a mitosis occurs one of the daughter cells is discarded. In this initial phase cells can have large oscillations of their metabolic parameters, and can occasionally step in parameter regions that would normally spell death: this does not occur here. Initialization lasts until the oscillations of

Table 1. Comparisons with experimental parameters.

Parameter	Simulation	Experiments	[7] Cell type	Ref.
[1]Glucose uptake (kg s^{-1} m^{-3})	$1.44 \cdot 10^{-3}$	$5.4 \pm 2.6 \cdot 10^{-3}$	Rat-T1, MR1	[37]
[1]Lactate release (kg s^{-1} m^{-3})	$1.35 \cdot 10^{-3}$	$5.4 \pm 0.9 \cdot 10^{-3}$	Rat-T1, MR1	[37]
[2]pO_2 (mmHg)	7	0–20	Rat-T1	[37]
		0–40	MR1	[37]
		20–60	EMT6/Ro	[38]
[3]pH	6.7	6.6	C6, H35	[39]
		6.96–6.99	U118-MG, HTh7	[40]
[4]DpH	0.77	0.41	U118-MG	[40]
		0.49±0.08	HTh7	[40]
[5]Viable cell rim thickness (mm)	155	200	EMT6/Ro	[38]
		142±16	HTh7	[40]
		310±28	U118-MG	[40]
		198±27	Col12	[41]
		225±26	HT29	[41]
[6]Hypoxic rim thickness (mm)	98	44±52	Col12	[41]
		44±52	HT29	[41]
Cell cycle distribution (%)	G0/G1 = 57.3	G0/G1 = 58±4	BMG-1	[42]
	S = 21.6	S = 19±1		
	G2/M = 21.1	G2/M = 23±1		

Metabolic and histologic parameters in spheroids of approximately 500 mm diameter: comparison between a single, large simulation, carried out with the parameters listed in Text S1, and experimental data.

Notes:

[1]Rate of glucose uptake or lactate release per viable spheroid volume (see [37]).

[2]Central pO_2 tension (experiments) or estimated in the centroid (simulations).

[3]pH has been determined in the central region of the spheroids. This corresponds to a sphere of radius $\approx$100mm about the centroid of the spheroid.

[4]Difference between environmental pH and pH 200 mm below the spheroid surface.

[5]In our simulations the viable cell rim thickness corresponds to the distance between the spheroid surface and the inner shell where only 5% of the cells are still alive. Experimental values have been determined by histology.

[6]These values corresponds to the radius of the necrotic core.

[7]Cell types are as follows: Rat-T1 = T24Ha-ras-transfected Rat1 cells (Rat1 = spontaneously immortalized rat embryo fibroblasts); MR1 = myc/ T24Ha-ras-cotransfected rat embryo fibroblasts; EMT6/Ro = mouse mammary tumor cells; C6 = rat glioma cells; H35 = rat hepatoma cells; U118-MG = human glioblastoma cells; HTh7 = human tyroid carcinoma cells; Col12 = moderately differentiated human colon adenocarcinoma ; HT29 = poorly differentiated human colon adenocarcinoma; BMG-1 = human glioma cells.

doi:10.1371/journal.pone.0013942.t001

metabolic parameters die out. We have determined the duration of the initialization phase observing the desynchronization of a population of initially synchronized cells: when oscillations of the relative fractions of cells in each cell-cycle phase become undetectable we estimate that cells have reached a stable state. It turns out that a simulated time of $3 \cdot 10^6$s (i.e. about 35 days of simulated time) is sufficient for initialization of cell with a period of about 20 hours. Usually the starting number of cells is quite small (normally just one cell to seed the growth of a single spheroid), and initialization executes in very short real time (a few seconds).

Metabolism, diffusion, transport, and growth

This part of the program solves the combined differential system of equations that describe internal cell metabolism and diffusion in the extracellular spaces (described in detail in Text S1), using the implicit Euler method. This leads to a system of nonlinear equations, that are solved in turn with a variant of the Newton-Raphson method. The functional scheme of this important part of the program is shown in figure 10. We wish to stress that although the number of variables can be quite large (more than 10^7 loop variables), convergence is reasonably fast, because the initial concentration values are invariably very close to the final ones.

Cell motion

Cell motion is also regulated by differential equations and the solution uses a strategy based on a semi-implicit method (described in detail in Text S1). Volume growth is regulated by the part that handles metabolism and diffusion, therefore it is loosely coupled to cell motion. However we have implemented an updating mechanism that effectively decouples the two parts of the program: this means that the program can use multithreading with shared memory and exploit the features of multicore processors.

Cellular events

This part of the program handles discrete events, like cell-cycle transitions, mitosis and cell death. In case of mitosis it also initializes the daughter cells – using the metabolic variables of the mother cell – and allocates memory for the new cells.

Geometry and topology of cell cluster

Geometrical and topological informations are updated here, using calls to CGAL methods [33] that compute the convex hull of the cluster of cells, the Delaunay triangulation of cell centers, and the alpha shape of the cluster – with an alpha parameter [33] equal to $(2r_0)^2$ where r_0 is the average cell radius. This part of the

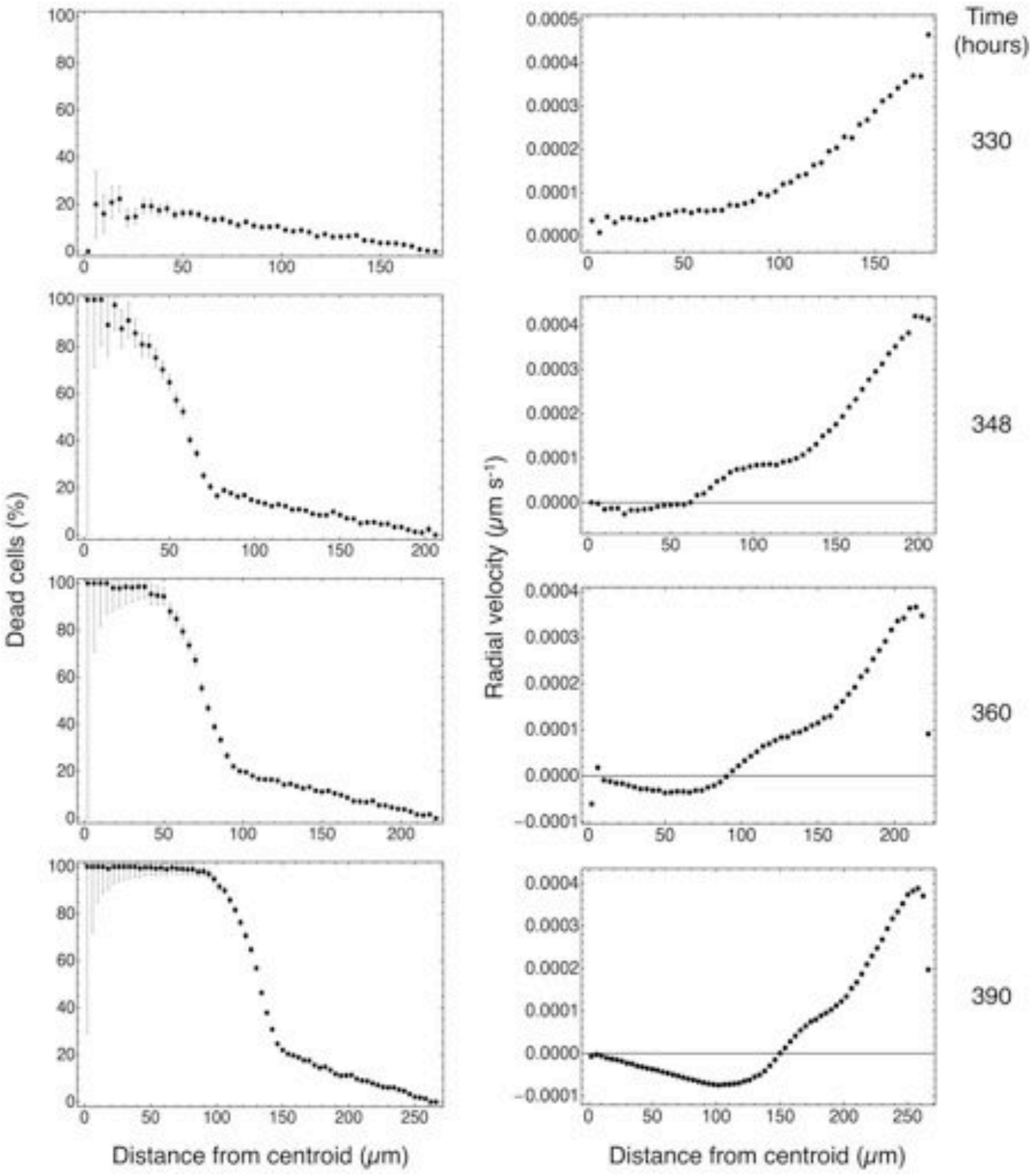

Figure 7. Fraction of dead cells (left column) and average radial velocity (right column) at different times. As the spheroid grows, the necrotic core becomes increasingly well defined, and as dead cells shrink, the radial velocity changes sign and a marked inward motion characterizes the central region.
doi:10.1371/journal.pone.0013942.g007

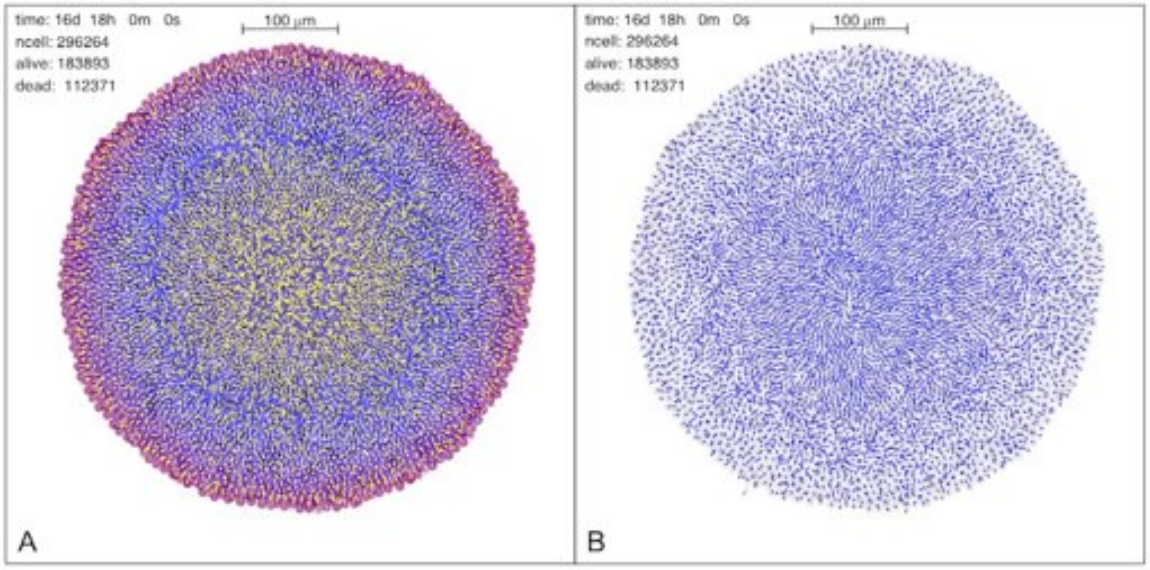

Figure 8. Two views of the microstructure of a simulated spheroid, with about 500mm diameter and 296264 cells (183893 live cells+112371 dead cells). (Left panel): flow of extracellular glucose along a central section of the tumor spheroid (yellow arrows) superposed on the plot of glucose concentration. The length of the arrows is proportional to the glucose flow intensity projected on the plane of the section. At this stage, the necrotic core is contracting as dead cells gradually shrink, and this leads to a slow outward flow of the glucose stored in the extracellular spaces in this central region. We observe that such a behavior depends on the effective diffusion coefficient of glucose, and it disappears completely when the diffusion coefficient is high enough. This also suggests that the flow of glucose and other substances, like therapeutic drugs, is strongly dependent on the biochemistry and structure of extracellular spaces, and even small changes can lead to markedly different internal spheroid morphologies. (Right panel): individual cell velocities in the simulated spheroid. This is the same central section as in the left panel, and the velocity vectors are projected on the plane of the section. The length of each vector is proportional to the projected speed. The velocities in the viable rim show a coherent outward motion, while the velocities in the necrotic core show a rather orderly inward motion, with some vortices due to local residual cell proliferation. The region in-between is somewhat chaotic and the global structure of this plot mirrors that of the glucose flow shown on the left. The supporting information includes higher-quality versions of these figures and those of other flows.
doi:10.1371/journal.pone.0013942.g008

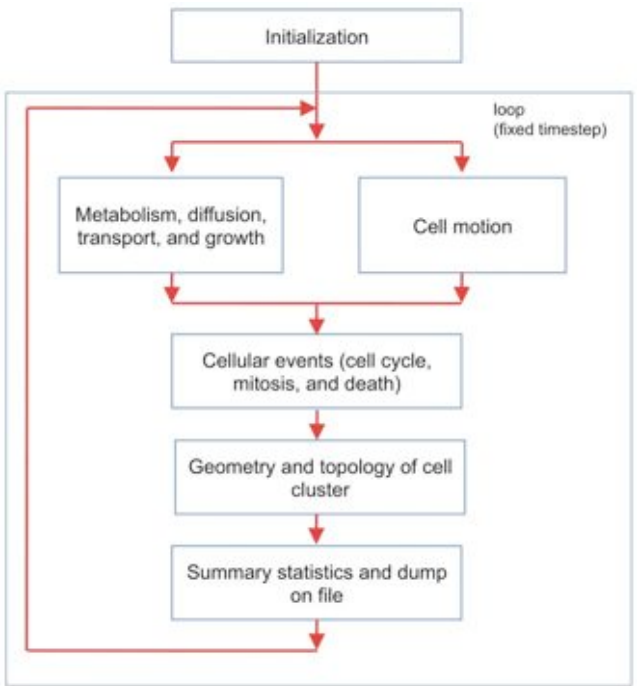

Figure 9. Functional blocks of the simulation program. Program initialization is followed by a loop that performs biochemical and biomechanical calculations. This is followed by a check of the status of individual cells – this is where we decide whether a cell advances in the cell cycle, undergoes mitosis, or dies. Next the program computes the geometry and the topology of the cell cluster, and finally it outputs intermediate statistics and results. The loop continues until a user-defined stop condition is met. Some parts of the program can proceed in parallel (like metabolism and cell motion), and we can use multithreaded code.
doi:10.1371/journal.pone.0013942.g009

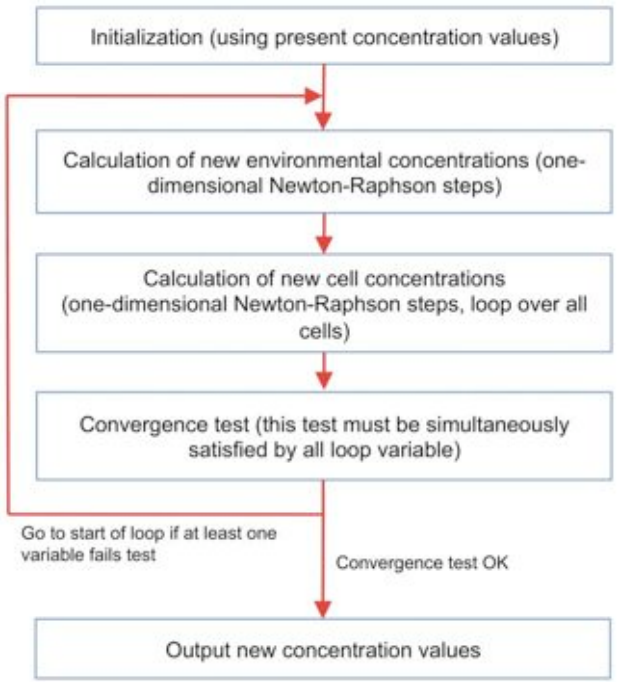

Figure 10. Functional blocks of the C++ method that computes metabolic and extracellular variables. This part performs a loop that computes the solution of the nonlinear equations found in the implicit Euler integration step [29] (see also Text S1). Although the number of variables can be quite large (more than 10^7 variables), convergence is fast, because the initial concentration values are invariably very close to the final ones.
doi:10.1371/journal.pone.0013942.g010

program uses this basic information to set all relevant geometrical and topological variables in the program.

Summary statistics and dump on file

The last step in the loop computes several statistics and outputs them on summary files. It also writes periodically the whole configuration of cells on file for further processing.

Program termination

The program repeats the loop until one of the stop conditions is met: either all cells are dead, or the program executed the required number of steps. Text S1 contains additional considerations on algorithmic complexity and on measured performance (see also figure S6 and figure S7).

Additional processing to extract useful informations from the simulation data is performed with several standard tools, like Mathematica [44].

Supporting Information

Text S1 Including tables and additional references.
Found at: doi:10.1371/journal.pone.0013942.s001 (0.89 MB DOC)

Figure S1 Sketch of the cell phases included in the simulation program. The arrow lengths suggest the relative duration of each phase. Phase G1 is divided in two parts: an initial subphase where cells are sensitive to variations in the environmental nutrient concentration (G1m) and a later subphase where cells are insensitive to deprivation of nutrients (G1p); in between these subphases there is an energetic checkpoint [1–3].
Found at: doi:10.1371/journal.pone.0013942.s002 (0.19 MB TIF)

Figure S2 Sketch of the metabolic network. Variables within circles represent molecular species and are expressed in units of concentration or mass. Non-obvious symbols are as follows (the suffixes ext and int denote, respectively, extracellular and intracellular variables): G = glucose, G6P = glucose-6-phosphate, STORE = glucose stored in the form of glycogen, AL = lactic acid, A = glutamine, ATPp = pool of ATP molecules, DNA = nuclear mass of DNA (normalized to 1 for the whole genome), mtDNA = mitochondrial DNA. Rates are represented by squares. The red circuit represents the oxygen sensor, whereas the green circuit represents the ATP sensor [1,2]. ''Cell cycle checkpoints'' denotes the molecular circuit of cell cycle control that has been modeled on the basis of previous studies on the dynamics of the allosteric effect [19,20]. The biological foundations of this simplified metabolic network have been given in references 1 and 2. Recent improvements with respect to our previous model include: internalization rates of glucose, glutamine and lactate are sensitive to extracellular pH and this dependence is now described by smoothed functions (see the text for details); synthesis of cellular proteins, nuclear DNA and mitochondrial DNA are now described by double-substrate Michaelis-Menten chemical reactions to take into account the dependence of protein and nucleic acid biosynthesis on glutamine (which stands phenomenologically for the wider class of aminoacids) and ATP availability.
Found at: doi:10.1371/journal.pone.0013942.s003 (0.77 MB TIF)

Figure S3 The geometry and topology of diffusion. a) Most substances are carried into and out of the cell by facilitated diffusion and there is an active mass exchange between cell and extracellular space. Each cell in the simulation program has its own extracellular space. b) Extracellular spaces are interconnected and there is a diffusion flow through the network of connections. c) The network of interconnected spaces is defined by a Delaunay triangulation. In this 2D representation, for any red dot we can define a Voronoy cell, i.e., the set of points in the plane that are closer to the given dot than to any other dot in the set. The dual structure is the Delaunay triangulation (Voronoy cells are black and Delaunay links are green). There is a Delaunay link between any two dots only if the respective Voronoy cells touch each other, therefore we can use the Delaunay triangulation to define proximity. This enables us to set up a discretized version of diffusion between extracellular spaces, like in b). In addition to the topology of contacts between cells we also keep into account geometry: g_{ab} in part b) is a geometric factor that modulates diffusion. d) The actual simulation is in 3D: here the Delaunay triangulation of a small cluster of cell centers shows up in transparency.
Found at: doi:10.1371/journal.pone.0013942.s004 (1.37 MB TIF)

Figure S4 Pictorial representation of the interaction force between two cells. The solid curve shows qualitatively the behavior of the interaction force, while the insects depict the corresponding situations (A. cells are compressed against each other, force is repulsive; B. cells are in contact, the total force vanishes; C. cell centers are slightly apart, force is attractive because of adhesive molecules on the cells' membranes; D. cells are no longer in contact, the total force vanishes again). The inset on the right corner shows the definitions of the basic geometric variables.
Found at: doi:10.1371/journal.pone.0013942.s005 (0.36 MB TIF)

Figure S5 The geometry of mitosis. R_0 is the radius of the initial cells, while R_1 and R_2 are the radii of the daughter cells: because of random asymmetries during mitosis, the daughter cells usually have different sizes. The program places the two daughter cells inside the region initially occupied by the mother, and the axis connecting the centers points in a random direction. This forces the two cells to push one against the other, and as cells separate the axis rotates, so that the new configuration fits the positions of neighboring cells. The cells' centers are separated by a distance which is roughly 0.4 R_0.
Found at: doi:10.1371/journal.pone.0013942.s006 (0.16 MB TIF)

Figure S6 CPU time needed to simulate 1 hour, vs. the number of cells in the spheroid. In this run, the precision of the solution of the global diffusion transport and metabolism problem is fixed at 1% and the timestep is 50 s (so that t_{CPU} is actually the CPU time needed to simulate 72 elementary timesteps). The solid curve shows the fit (S.69) in Text S1.
Found at: doi:10.1371/journal.pone.0013942.s007 (0.15 MB TIF)

Figure S7 Total CPU time vs. N. This figure shows the total CPU time vs. N in the same run as figure S6. The solid curve is a simple fit with a quadratic polynomial function.
Found at: doi:10.1371/journal.pone.0013942.s008 (0.14 MB TIF)

Figure S8 Oxygen concentration and flow at simulated time = 14 days. Cells are coloured to show the oxygen concentration (color mapping, blue = low concentration, red = high concentration), while the yellow arrows show the oxygen flow (arrow length proportional to flow intensity).
Found at: doi:10.1371/journal.pone.0013942.s009 (2.06 MB TIF)

Figure S9 Oxygen concentration and flow at simulated time = 16 days. Cells are coloured to show the oxygen concentration (color mapping, blue = low concentration, red = high concentration), while the yellow arrows show the oxygen flow (arrow length proportional to flow intensity).
Found at: doi:10.1371/journal.pone.0013942.s010 (1.14 MB TIF)

Figure S10 Oxygen concentration and flow at simulated time = 17 days. Cells are coloured to show the oxygen concentra-

tion (color mapping, blue = low concentration, red = high concentration), while the yellow arrows show the oxygen flow (arrow length proportional to flow intensity).
Found at: doi:10.1371/journal.pone.0013942.s011 (4.88 MB TIF)

Figure S11 Extracellular glucose concentration and flow at simulated time = 14 days. Cells are coloured to show the concentration of extracellular glucose (color mapping, blue = low concentration, red = high concentration), while the yellow arrows show the flow of extracellular glucose (arrow length proportional to flow intensity).
Found at: doi:10.1371/journal.pone.0013942.s012 (2.05 MB TIF)

Figure S12 Extracellular glucose concentration and flow at simulated time = 15 days. Cells are coloured to show the concentration of extracellular glucose (color mapping, blue = low concentration, red = high concentration), while the yellow arrows show the flow of extracellular glucose (arrow length proportional to flow intensity).
Found at: doi:10.1371/journal.pone.0013942.s013 (2.88 MB TIF)

Figure S13 Extracellular glucose concentration and flow at simulated time = 16 days. Cells are coloured to show the concentration of extracellular glucose (color mapping, blue = low concentration, red = high concentration), while the yellow arrows show the flow of extracellular glucose (arrow length proportional to flow intensity).
Found at: doi:10.1371/journal.pone.0013942.s014 (1.15 MB TIF)

Figure S14 Extracellular glucose concentration and flow at simulated time = 17 days. Cells are coloured to show the concentration of extracellular glucose (color mapping, blue = low concentration, red = high concentration), while the yellow arrows show the flow of extracellular glucose (arrow length proportional to flow intensity).
Found at: doi:10.1371/journal.pone.0013942.s015 (4.97 MB TIF)

Figure S15 Extracellular glutamine concentration and flow at simulated time = 14 days. Cells are coloured to show the concentration of extracellular glutamine (color mapping, blue = low concentration, red = high concentration), while the yellow arrows show the flow of extracellular glutamine (arrow length proportional to flow intensity).
Found at: doi:10.1371/journal.pone.0013942.s016 (2.06 MB TIF)

Figure S16 Extracellular glutamine concentration and flow at simulated time = 17 days. Cells are coloured to show the concentration of extracellular glutamine (color mapping, blue = low concentration, red = high concentration), while the yellow arrows show the flow of extracellular glutamine (arrow length proportional to flow intensity).
Found at: doi:10.1371/journal.pone.0013942.s017 (4.94 MB TIF)

Figure S17 Extracellular glutamine concentration and flow at simulated time = 18 days. Cells are coloured to show the concentration of extracellular glutamine (color mapping, blue = low concentration, red = high concentration), while the yellow arrows show the flow of extracellular glutamine (arrow length proportional to flow intensity).
Found at: doi:10.1371/journal.pone.0013942.s018 (6.11 MB TIF)

Figure S18 Extracellular lactate concentration and flow at simulated time = 18 days. Cells are coloured to show the concentration of extracellular lactate (color mapping, blue = low concentration, red = high concentration), while the yellow arrows show the flow of extracellular lactate (arrow length proportional to flow intensity). Lactate always flows outward in the simulation: this is a single snapshot taken after both glucose and glutamine have developed their split flow regime.
Found at: doi:10.1371/journal.pone.0013942.s019 (6.07 MB TIF)

Figure S19 Velocity vectors projected on the plane of the slice at simulated time = 14 days. The vectors show the cells' motions in the plane of the slice (yellow arrows, arrow length proportional to flow intensity). Cells in the core perform complex looping motions, while cells in the viable rim always push outward.
Found at: doi:10.1371/journal.pone.0013942.s020 (1.62 MB TIF)

Figure S20 Velocity vectors projected on the plane of the slice at simulated time = 16 days. The vectors show the cells' motions in the plane of the slice (yellow arrows, arrow length proportional to flow intensity). Cells in the core perform complex looping motions, while cells in the viable rim always push outward.
Found at: doi:10.1371/journal.pone.0013942.s021 (3.08 MB TIF)

Figure S21 Velocity vectors projected on the plane of the slice at simulated time = 18 days. The vectors show the cells' motions in the plane of the slice (yellow arrows, arrow length proportional to flow intensity). Cells in the core perform complex looping motions, while cells in the viable rim always push outward.
Found at: doi:10.1371/journal.pone.0013942.s022 (5.00 MB TIF)

Movie S1 Movie of a central slice of a simulated tumor spheroid showing the development of the necrotic core (red = live cells, black = dead cells).
Found at: doi:10.1371/journal.pone.0013942.s023 (5.99 MB MOV)

Movie S2 Movie of a central slice of a simulated tumor spheroid showing the flow of extracellular glucose (same coding as figures S11, S12, S13, S14).
Found at: doi:10.1371/journal.pone.0013942.s024 (21.18 MB MOV)

Movie S3 Movie of a central slice of a simulated tumor spheroid showing the map of projected cell velocities (same coding as figures S19, S20, S21).
Found at: doi:10.1371/journal.pone.0013942.s025 (28.40 MB MOV)

Author Contributions

Conceived and designed the experiments: EM RC. Performed the experiments: EM RC. Analyzed the data: EM RC. Contributed reagents/materials/analysis tools: EM RC. Wrote the paper: EM RC.

References

1. Sutherland RM (1988) Cell and environment interactions in tumor microregions: the multicell spheroid model. Science 240: 177–84.
2. Bjerkvig R (1992) Spheroid Culture in Cancer Research. Boca Raton, Fla.: CRC Press.
3. Mueller-Klieser W (1997) Three-dimensional cell cultures: from molecular mechanisms to clinical applications. Am J Physiol 273: C1109–23.
4. Mueller-Klieser W (2000) Tumor biology and experimental therapeutics. Crit Rev Oncol Hematol 36: 123–39.
5. Gottfried E, Kunz-Schughart LA, Andreesen R, Kreutz M (2006) Brave little world: spheroids as an in vitro model to study tumor-immune-cell interactions. Cell Cycle 5: 691–695.
6. Friedrich J, Ebner R, Kunz-Schughart LA (2007) Experimental anti-tumor therapy in 3-D: spheroids–old hat or new challenge? Int J Radiat Biol 83: 849–871.
7. Lin RZ, Chang HY (2008) Recent advances in three-dimensional multicellular spheroid culture for biomedical research. Biotechnology Journal 3: 1172.
8. Hirschhaeuser F, Menne H, Dittfeld C, West J, Mueller-Klieser W, et al. (2010) Multicellular tumor spheroids: an underestimated tool is catching up again. J Biotechnol 148: 3–15.
9. Casciari JJ, Sotirchos SV, Sutherland RM (1992) Mathematical modelling of microenvironment and growth in EMT6/Ro multicellular tumour spheroids. Cell Prolif 25: 1–22.

10. Venkatasubramanian R, Henson MA, Forbes NS (2006) Incorporating energy metabolism into a growth model of multicellular tumor spheroids. J Theor Biol 242: 440–53.
11. Sander LM, Deisboeck TS (2002) Growth patterns of microscopic brain tumors. Phys Rev E Stat Nonlin Soft Matter Phys 66: 051901.
12. Stein AM, Demuth T, Mobley D, Berens M, Sander LM (2007) A mathematical model of glioblastoma tumor spheroid invasion in a three-dimensional in vitro experiment. Biophys J 92: 356–65.
13. Jiang Y, Pjesivac-Grbovic J, Cantrell C, Freyer JP (2005) A multiscale model for avascular tumor growth. Biophys J 89: 3884–94.
14. Schaller G, Meyer-Hermann M (2005) Multicellular tumor spheroid in an off-lattice Voronoi-Delaunay cell model. Phys Rev E Stat Nonlin Soft Matter Phys 71: 051910.
15. Kim Y, Stolarska MA, Othmer HG (2007) A Hybrid Model For Tumor Spheroid Growth In Vitro I: Theoretical Development And Early Results. Mathematical Models and Methods in Applied Sciences 17, Suppl.: 1773–1798.
16. Engelberg JA, Ropella GEP, Hunt CA (2008) Essential operating principles for tumor spheroid growth. BMC Syst Biol 2: 110.
17. Nederman T, Norling B, Glimelius B, Carlsson J, Brunk U (1984) Demonstration of an extracellular matrix in multicellular tumor spheroids. Cancer Res 44: 3090–7.
18. Dorie MJ, Kallman RF, Rapacchietta DF, Van Antwerp D, Huang YR (1982) Migration and internalization of cells and polystyrene microsphere in tumor cell spheroids. Exp Cell Res 141: 201–9.
19. Chignola R, Foroni R, Franceschi A, Pasti M, Candiani C, et al. (1995) Heterogeneous response of individual multicellular tumour spheroids to immunotoxins and ricin toxin. Br J Cancer 72: 607–14.
20. Bortner CD, Cidlowski JA (2002) Apoptotic volume decrease and the incredible shrinking cell. Cell Death Differ 9: 1307–10.
21. Chignola R, Milotti E (2005) A phenomenological approach to the simulation of metabolism and proliferation dynamics of large tumour cell populations. Phys Biol 2: 8–22.
22. Chignola R, Del Fabbro A, Dalla Pellegrina C, Milotti E (2007) Ab initio phenomenological simulation of the growth of large tumor cell populations. Phys Biol 4: 114–33.
23. Chignola R, Milotti E (2004) Numerical simulation of tumor spheroid dynamics. Physica A: Statistical Mechanics and its Applications 338: 261–266.
24. Alberts B, Wilson JH, Hunt T (2008) Molecular Biology of the Cell. New York: Garland Science, 5th edition.
25. Chignola R, Dalla Pellegrina C, Del Fabbro A, Milotti E (2006) Thresholds, long delays and stability from generalized allosteric effect in protein networks. Physica A: Statistical and Theoretical Physics 371: 463–472.
26. Milotti E, Del Fabbro A, Dalla Pellegrina C, Chignola R (2007) Dynamics of allosteric action in multisite protein modification. Physica A: Statistical Mechanics and its Applications 379: 133–150.
27. Chignola R, Schenetti A, Andrighetto G, Chiesa E, Foroni R, et al. (2000) Forecasting the growth of multicell tumour spheroids: implications for the dynamic growth of solid tumours. Cell Prolif 33: 219–29.
28. Yu P, Mustata M, Turek JJ, French PMW, Melloch MR, et al. (2003) Holographic optical coherence imaging of tumor spheroids. Appl Phys Lett 83: 575–577.
29. Milotti E, Del Fabbro A, Chignola R (2009) Numerical integration methods for large-scale biophysical simulations. Computer Physics Communications 180: 2166–2174.
30. Cornish-Bowden A (1979) Fundamentals of enzyme kinetics. London: Butterworths.
31. O'Rourke J (1998) Computational geometry in C. Cambridge, UK: Cambridge University Press, 2nd ed edition.
32. de Berg M, Cheon O, van Kreveld M, Overmars M (2008) Computational Geometry: Algorithms and Applications. Berlin: Springer, 3rd ed edition.
33. CGAL, Computational Geometry Algorithms Library. Http://www.cgal.org.
34. Guibas LJ, Knuth DE, Sharir M (1992) Randomized incremental construction of Delaunay and Voronoi diagrams. Algorithmica 7: 381–413.
35. Dwyer RA (1991) Higher-dimensional Voronoi diagrams in linear expected time. Discrete and Computational Geometry 6: 343–367.
36. Flekkøy EG, Coveney PV, Fabritiis GD (2000) Foundations of dissipative particle dynamics. Phys Rev E 62: 2140–2157.
37. Walenta S, Doetsch J, Mueller-Klieser W, Kunz-Schughart LA (2000) Metabolic imaging in multicellular spheroids of oncogene-transfected fibroblasts. J Histochem Cytochem 48: 509–22.
38. Mueller-Klieser W, Freyer JP, Sutherland RM (1986) Influence of glucose and oxygen supply conditions on the oxygenation of multicellular spheroids. Br J Cancer 53: 345–53.
39. Alvarez-Pérez J, Ballesteros P, Cerdán S (2005) Microscopic images of intraspheroidal pH by 1H magnetic resonance chemical shift imaging of pH sensitive indicators. MAGMA 18: 293–301.
40. Acker H, Carlsson J, Holtermann G, Nederman T, Nylen T (1987) Influence of Glucose and Buffer Capacity in the Culture Medium on Growth and pH in Spheroids of Human Thyroid Carcinoma and Human Glioma Origin. Cancer Res 47: 3504–3508.
41. Sutherland RM, Sordat B, Bamat J, Gabbert H, Bourrat B, et al. (1986) Oxygenation and Differentiation in Multicellular Spheroids of Human Colon Carcinoma. Cancer Res 46: 5320–5329.
42. Khaitan D, Chandna S, Arya MB, Dwarakanath BS (2006) Establishment and characterization of multicellular spheroids from a human glioma cell line; implications for tumor therapy. J Transl Med 4: 12.
43. Deisboeck TS, Couzin ID (2009) Collective behavior in cancer cell populations. Bioessays 31: 190–7.
44. Wolfram Research I (2008) Mathematica. ChampaignIllinois: Wolfram Research, Inc., version 7.0 edition.
45. Yuhas JM, Li AP, Martinez AO, Ladman AJ (1977) A simplified method for production and growth of multicellular tumor spheroids. Cancer Res 37: 3639–43.

Supporting text for

Emergent Properties of Tumor Microenvironment in a Real-life Model of Multicell Tumor Spheroids

Edoardo Milotti[*] and Roberto Chignola

**To whom correspondence should be addressed. E-mail: milotti@ts.infn.it*

This Supporting text includes:

Materials and Methods

Tables S1 to S5

References

Introduction

This supplementary text contains a systematic overview of the mathematical and computational details of the model introduced in the main text, and is divided in six parts. We start with a review of the single-cell model which summarizes the internal biochemical machinery included in the simulated cells: although this has already been described before [1,2], here we include some recent improvements and in the second part we summarize the setup of the numerical method for diffusion and transport processes. This is followed by a review of the dynamical interactions whereby cells interact mechanically with one another. Finally we list all the parameters used in the simulation program and include broad considerations on the computational complexity of the model. The last section contains a selection of images obtained in the simulations.

A. Brief review of the single-cell model

The cells in the simulation program behave as automata that obey mostly deterministic rules, although they also include some circumscribed but important randomness. Each cell has many individual status variables that are listed in table S1, and steps through well-defined phases before dividing. After cell division the old cell is erased from the program's cell list, the daughter cells are added to the list and each of them starts a new independent cell cycle. The cell cycle is sketched in figure S1.

We approximate cells as soft spheres of radius r, surrounded by a thin layer that represents the extracellular space. The extracellular space is essential for a proper description of diffusion of molecules like glucose that are transported across the cell membranes by facilitated diffusion, and the variables that characterize the extracellular space around each cell are also included in the list of status variables.

The biochemistry of cells

The biochemical model of an isolated tumor cell developed in references [1] and [2] is outlined in figure S2 and comprises the following parts:

1. *Glucose uptake and retention by cells*
2. *Glucose-6-phosphate utilization by cells*
3. *Glycogen storage*
4. *Glutamine (aminoacid) uptake*
5. *Oxygen uptake*
6. *ATP production and consumption*
7. *Lactate production*
8. *DNA synthesis*
9. *Protein synthesis*
10. *Mitochondrial proliferation*
11. *Dynamics of cell volume*
12. *Checkpoints and phase changes*
13. *Corrections due to internal and environmental pH*
14. *Other corrections*

Now we describe in detail each item in the list.

Glucose uptake and retention by cells

The equations that regulate the metabolism and transport of glucose are

$$\frac{dm_{G,C}}{dt} = M_G\left[m_{G,C}(t)\right] + T_G\left[m_{G,c}(t), m_{G,C}(t)\right] \qquad \textit{(S.1a)}$$

$$\frac{dm_{G,c}}{dt} = D_G \sum_{\langle b \rangle}\left(\frac{m_{G,b}(t)}{V_b(t)} - \frac{m_{G,c}(t)}{V_c(t)}\right) g_{bc} - T_G\left[m_{G,c}(t), m_{G,C}(t)\right] \qquad \textit{(S.1b)}$$

where $m_{G,C}$ *and* $m_{G,c}$ *denote respectively the mass of glucose inside the cell (C) and inside the surrounding extracellular volume (c).*

The metabolic (M_G*) and the transport (*T_G*) functions are respectively*

$$M_G\left(m_{G,C}\right) = -\frac{v_{\max,2} m_{G,C}^2}{\left(V_C K_2 + m_{G,C}\right)\left(V_C K_a + m_{G,C}\right)} - \frac{v_{\max,22} m_{G,C}^2}{\left(V_C K_{22} + m_{G,C}\right)\left(V_C K_a + m_{G,C}\right)} \qquad \textit{(S.2a)}$$

$$T_G\left(m_{G,C}, m_{G,c}\right) = a2c \cdot \frac{v_{\max,1} m_{G,c}}{V_c K_1 + m_{G,c}} - c2a \frac{v_{\max,1} m_{G,C}}{V_C K_1 + m_{G,C}} \qquad \textit{(S.2b)}$$

where

$v_{\max,1} = VMAX1 \cdot h \cdot S$

h, a2c, c2a are correction factors that shall be specified later on, S is the cell surface, V_C is the cell volume, V_c is the extracellular volume, and finally the values $v_{\max,2} = VMAX2$; $v_{\max,22} = VMAX22$; *K_1, K_2, K_{22}, are cellular parameters (see below).*

The metabolic function (M_G) in equation (S.1a) corresponds to hexokinase and glucokinase activity[1].

The first term on the rhs of equation (S.1b) describes diffusion on the disordered lattice of extracellular volumes; here D_G is the glucose diffusion coefficient either in the extracellular space or in the enviroment (water) (see table S5), the g_{bc}'s are numerical coefficients that belong to the discretization of the diffusion problem on the cell network (see section B), and the triangular bracket $\langle b \rangle$ *denotes the set of the adjacent extracellular spaces. This diffusion part is necessary for the consistency of the whole procedure: diffusion in the cell cluster and transport into and out of the cell are inescapably related (see section B and ref. 4).*

Glucose-6-phosphate (G6P) utilization by cells

The equation that regulates the G6P content of the cell is

$$\frac{dm_{G6P,C}}{dt} = -M_G\left(m_{G,C}\right) - \left(g_1 + g_2 + g_3\right) \qquad \textit{(S.3)}$$

where $m_{G6P,C}$ *is the mass of G6P inside cell C, and the rates* g_i *denote different paths of G6P utilization (see also figure S2 and reference [1])*

$$g_1 = \left(t_{pH} \cdot coeffg1\right) m_{(G6P),C} \qquad \textit{(S.4a)}$$

$$g_2 = \left(coeffg2 \cdot SensO2\right) m_{(G6P),C} \qquad \textit{(S.4b)}$$

$$g_3 = \left(coeffg3\right) m_{(G6P),C} \qquad \textit{(S.4c)}$$

The underlying utilization model is straighforward, all the rates g_i *are simply proportional to G6P content of the cell, as this fits quite well the existing experimental data [1].*
Moreover t_{pH} *and SensO2 are correction terms (see below) and coeffg1, coeffg2, coeffg3 are cellular parameters (see below).*

The metabolic function (M_G*) has been defined above for glucose, and corresponds to glucose transformation into G6P.*

Glycogen storage

Glucose is partly stored as glycogen. Its production/consumption, follows the equation

$$\frac{d}{dt} Store = \left(g_3 + p_{11}\right) - \left(r_1 + r_2 + r_3\right) \qquad \textit{(S.5)}$$

where Store is the glycogen mass inside the cell, the rates r_i *correspond to different paths of Store utilization, the rate* p_{11} *corresponds to glycogen*

production via the glutamine pathway (defined below), and finally the rate g_3 is associated to the glycogen production path from G6P conversion

$$r_1 = \left(t_{pH} \cdot coeffr1\right) \frac{Store}{V_C \cdot Kmc + Store} \qquad (S.6a)$$

$$r_2 = g_3 \cdot SensO2 \frac{Store}{V_C \cdot Kmc + Store} \qquad (S.6b)$$

$$r_3 = SensO2 \cdot SensATP \cdot \frac{1}{30} \cdot \frac{PM_G}{PM_{ATP}} \cdot \left(ATP_{St} - ATPOx\right) \frac{Store}{V_C \cdot Kmc + Store} \qquad (S.6c)$$

$$p_{11} = t_{p11}\left(t_{pH} \cdot coeffr1\right) \cdot \frac{m_{A,C}}{V_C \cdot Kmd + m_{A,C}} \cdot \left(1 - SensATP\right) \qquad (S.6d)$$

Notice that these rates are modeled with simple Michaelis-Menten functions, where the substrate is the Store itself (for consumption) or glutamine (for production).

In addition to the symbols already defined in the previous sections, there are also other correction factors, t_{p11}, SensATP, and SensO2 (defined later). There is also a couple of additional parameters, Kmd and Kmc, and two molecular weights, PM_G and PM_{ATP} (all quantities identified by symbols like PM_X are molecular weights): they are all listed in table S2. There are also two quantities related to ATP, ATP_{St} and ATPOx, which are defined in the section on ATP.

Glutamine (aminoacid) uptake

The equations that regulate the metabolism and transport of glutamine are

$$\frac{dm_{A,C}}{dt} = M_A\left[m_{A,C}(t)\right] + T_A\left[m_{A,c}(t), m_{A,C}(t)\right] \qquad (S.7a)$$

$$\frac{dm_{A,c}}{dt} = D_A \sum_{\langle b \rangle} \left(\frac{m_{A,b}(t)}{V_b(t)} - \frac{m_{A,c}(t)}{V_c(t)} \right) g_{bc} - T_A\left[m_{A,c}(t), m_{A,C}(t) \right] \qquad \textit{(S.7c)}$$

where $m_{A,C}$ and $m_{A,c}$ denote respectively the mass of glutamine inside the cell (C) and inside the surrounding extracellular volume (c). As for glucose, equation (S.7c) includes a diffusion term and D_A is the diffusion constant of glutamine either in the extracellular space or in the enviroment (water) (see table S5).

The metabolic (M_A) and the transport (T_A) functions are respectively

$$M_A\left(m_{A,C}\right) = -\left(p_{11} + p_{22}\right) - \frac{VMAXP_A ATPp \cdot m_{A,C}}{V_C^2 Kmp + ATPp \cdot m_{A,C}} - \frac{VMAXDNA_A ATPp \cdot m_{A,C}}{V_C^2 KmDNA + ATPp \cdot m_{A,C}} - \frac{VMAXM_A \cdot ATPp \cdot m_{A,C}}{V_C^2 KmM + ATPp \cdot m_{A,C}} \qquad \textit{(S.8a)}$$

$$T_A\left(m_{A,C}, m_{A,c}\right) = a2cA \cdot \frac{v_{\max,A} m_{A,c}}{V_c KmA + m_{A,c}} - c2aA \cdot \frac{v_{\max,A} m_{A,C}}{V_C KmA + m_{A,C}} \qquad \textit{(S.8b)}$$

where $v_{\max,A} = VMAXA \cdot S$, and

$$p_{22} = 3 \cdot SensO2 \cdot SensATP \cdot \frac{1}{30} \cdot \frac{PM_G}{PM_{ATP}} \cdot \left(ATP_{St} - ATPOx\right) \frac{m_{A,C}}{V_C \cdot Kmd + m_{A,C}} \qquad \textit{(S.9)}$$

is the rate of glutamine consumption for ATP production (see below), and the three double-substrate Michaelis-Menten rates correspond to protein production, DNA synthesis, and glutamine consumption for mitochondrial proliferation. In these formulas there are two additional correction factors, a2cA and c2aA, defined below, and several parameters, VMAXA, $VMAXP_A$, $VMAXDNA_A$, $VMAXM_A$, Kmp, KmDNA, KmM, all listed below.

Oxygen uptake

The equation for oxygen metabolism and diffusion is

$$\frac{dm_{O2,C}}{dt} = D_{O2}\sum_{\langle B\rangle}\left(\frac{m_{O2,B}(t)}{V_B(t)} - \frac{m_{O2,C}(t)}{V_C(t)}\right)g_{BC} + M_{O2}\left[m_{O2,C}(t)\right] \qquad (S.10)$$

where D_{O2} is the oxygen diffusion coefficient either in water or in the cluster of cells (see table S5), and the metabolic function is

$$M_{O2}\left(m_{O2,C}\right) = -6\frac{PM_{O2}}{PM_G}\left(g_2 + r_2 + r_3 + p_{22}\right) \qquad (S.11)$$

There is no extracellular quantity here, as oxygen diffuses normally over the cell and there is no specific transport process.

ATP production and consumption

The differential equation for ATP is

$$\frac{d}{dt}ATPp = ATPtot \qquad (S.12)$$

where ATPp is the total ATP mass in the cell, and ATPtot is the total variation rate. ATPtot is a sum of several contributions:

- *ATPOx (ATP production rate from oxidative phosphorylation)*
- *ATPNOx (ATP production rate from anaerobic glycolysis)*
- *ATP2 (ATP production rate from glycogen (Store))*
- *ATP3 (ATP production rate from aminoacids (glutamine))*
- *ConsATP (ATP consumption rate due to gluconeogenesis)*
- *$ConsATP_1$ (parameterization of the ATP consumption proportional to cellular volume)*
- *$ConsATP_2$ (ATP consumption rate for protein synthesis)*
- *$ConsATP_3$ (ATP consumption rate for DNA synthesis)*
- *$ConsATP_5$ (ATP consumption rate for mitochondrial proliferation)*

which are defined by the equations

$$ATPOx = 30\frac{PM_{ATP}}{PM_G}\left(g_2 + r_2\right) \qquad \textit{(S.13.a)}$$

$$ATPNOx = 2\frac{PM_{ATP}}{PM_G}\left(g_1 + r_1\right) \qquad \textit{(S.13.b)}$$

$$ATP2 = 30\frac{PM_{ATP}}{PM_G}r_3 \qquad \textit{(S.13.c)}$$

$$ATP3 = 28\frac{PM_{ATP}}{PM_G}p_{22} \qquad \textit{(S.13.d)}$$

$$ConsATP = 2\frac{PM_{ATP}}{PM_G}p_{11} \qquad \textit{(S.13.e)}$$

$$ConsATP_1 = v_{work}C1\cdot ATPp \qquad \textit{(S.13.f)}$$

$$ConsATP_2 = \frac{VMAXP_{ATP}ATPp\cdot m_{A,C}}{V_C^2 Kmp + ATPp\cdot m_{A,C}} \qquad \textit{(S.13.g)}$$

$$ConsATP_3 = \frac{VMAXDNA_{ATP}ATPp\cdot m_{A,C}}{V_C^2 KmDNA + ATPp\cdot m_{A,C}} \qquad \textit{(S.13.h)}$$

$$ConsATP_5 = \frac{VMAXM_{ATP}\cdot ATPp\cdot m_{A,C}}{V_C^2 KmM + ATPp\cdot m_{A,C}} \qquad \textit{(S.13.i)}$$

$$\begin{aligned} ATPtot = {} & ATPOx + ATPNox + ATP2 + ATP3 \\ & -ConsATP - ConsATP_1 - ConsATP_2 - ConsATP_3 - ConsATP_5 \end{aligned} \qquad \textit{(S.13.j)}$$

In these equations there are a few additional parameters, v_{work}, $C1$, $VMAXP_{ATP}$, $VMAXDNA_{ATP}$, *and* $VMAXM_{ATP}$, *which are specified below.*

Here we remark that some of these terms are representative of large classes of processes, in particular $ConsATP_1$ represents all those processes that utilize ATP and are extensively distributed over the cellular volume[1].

Lactate production

The equations that regulate the production and transport of lactate are

$$\frac{dm_{AcL,C}}{dt} = M_{AcL}\left[m_{AcL,C}(t)\right] + T_{AcL}\left[m_{AcL,c}(t), m_{AcL,C}(t)\right] \qquad \textit{(S.14a)}$$

$$\frac{dm_{AcL,c}}{dt} = D_{AcL}\sum_{\langle b\rangle}\left(\frac{m_{AcL,b}(t)}{V_b(t)} - \frac{m_{AcL,c}(t)}{V_c(t)}\right)g_{bc} - T_{AcL}\left[m_{AcL,c}(t), m_{AcL,C}(t)\right] \qquad \textit{(S.14.b)}$$

where D_{AcL} is the lactate diffusion coefficient either in the extracellular space or in the enviroment (water) (see table S5), and

$$M_{AcL}\left(m_{AcL,C}\right) = 2g_1 + 2r_1 \qquad \textit{(S.15a)}$$

$$T_{AcL}\left(m_{AcL,C}, m_{AcL,c}\right) = a2cAcL\cdot\frac{v_{\max,AcL}m_{AcL,c}}{V_c\cdot KmAcL + m_{AcL,c}} - c2aAcL\cdot\frac{v_{\max,AcL}m_{AcL,C}}{V_C\cdot KmAcL + m_{AcL,C}} \qquad \textit{(S.15b)}$$

where $v_{\max,AcL} = VMAXAcL\cdot S$, and, as before, a2cAcL and c2aAcL are correction factors, while VMAXAcL and KmAcL are cellular parameters.

DNA synthesis

The equation for DNA synthesis is

---

[1] Notice also that a term $ConsATP_4$ is missing: the name is reserved to a class of processes not yet included in the program.

$$\frac{dDNA}{dt} = v_{DNA} \qquad (S.16)$$

where DNA is the fraction of a complete DNA molecule, and v_{DNA} *is the rate of DNA synthesis from a double-substrate Michaelis-Menten term:*

$$v_{DNA} = \frac{VMAXDNA \cdot m_{ATP} \cdot m_A}{V_C^2 KmDNA + m_{ATP} \cdot m_A} \qquad (S.17)$$

Here the glutamine mass (m_A*) represents the contribution of the other aminoacids as well.*

Protein synthesis

The equation for protein production is similar to (S.16), with the difference that now it represents a whole class of substances (all the proteins):

$$\frac{dm_p}{dt} = v_p \qquad (S.18)$$

where m_p *is the total protein mass in the cell, and*v_p *is the rate of protein production from a double-substrate Michaelis-Menten term:*

$$v_p = \frac{VMAXP \cdot ATPp \cdot m_A}{V_C^2 Kmp + ATPp \cdot m_A} \qquad (S.19)$$

The protein mass determines also the amounts (masses) of some specific proteins, pRb (retinoblastoma protein) and three cyclins (D, E, X = A+B):

pRb_fraction = 1.5e-2 times m_p

cyclinD_fraction = 10.e-3 times m_p

cyclinE_fraction = 3.e-3 times m_p

cyclinX_fraction = 14.e-3 times m_p

The amount of pRb that is carried over to daughter cells in mitosis is important because this indirectly determines the duration of the G1-phase, and we model the fluctuating duration of the G1-phase assuming that pRb is bound to parts of the nucleus that are partitioned binomially at mitosis. This modeling requires one additional cell parameter, NUCLEAR_OBJ, which is the (fictitious) number of parts to which pRb is bound.

Mitochondrial proliferation

The number of mitochondria is described by the continuous variable M, which follows the differential equation

$$\frac{dM}{dt} = v_M \qquad \textit{(S.20)}$$

where v_M *is the rate of mitochondrial proliferation and is associated to a double-substrate Michaelis-Menten term which is proportional to the production of mitochondrial DNA:*

$$v_M = \frac{VMAXM \cdot ATPp \cdot m_{A,C}}{V_C^2 KmM + ATPp \cdot m_{A,C}} \qquad \textit{(S.21)}$$

where VMAXM is yet another cellular parameter.

Mitochondria are partitioned randomly between the daughter cells at mitosis. Experimental observations indicate that this partitioning follows a binomial distribution [5,6], however, in order to better reproduce the observed desynchronization of disperse cell populations [7], mitochodria are clustered in small groups – a noteworthy fact that is experimentally observed [8] – and it is these groups that are actually shared between cells; the clustering factor ClusteringFactor belongs to the list of cell parameters as well.

Dynamics of cell volume

Cellular volume is a notoriously complicated cellular variable [9,10], and in particular it is related to osmotic pressure, and thus to the concentration of many substances inside cells. Here we take the total ATP mass as representative of this vast array of substances, and we assume that the cellular volume is partly determined by the total ATP mass. In addition, there are fixed volume contributions from the cell nucleus and from the organelles. The organelles themselves are variable in number, and again, we take the number of mitochondria as representative of the whole class of cellular organelles. These considerations yield the following - extremely simplified - formula for the volume of living cells:

$$V_C = V_{\min}\left(1 + DNA\right) + C2 \cdot Mit + C1 \cdot ATPp \qquad (S.22)$$

where DNA is the fraction of synthetized DNA molecule as in eq. (S.16), while C1, C2 and V_{min} are cellular parameters. Since V_{min} is the nuclear volume, eq. (S.22) takes into account the effective doubling of nuclear volume during the S-phase.

In the program we also assume that a cell can become apoptotic - for reasons explained below, in the section on cell-phase transitions - and after death the volume gradually shrinks [11] according to the equation

$$\frac{dV_C}{dt} = -DVap \cdot V_C \qquad (S.23)$$

which has the exact solution

$$V_C = V_0 \exp\left(-DVap \cdot t\right) \qquad (S.24)$$

where DVap is yet another cellular parameter, and V_0 is the cell's volume at death. This shrinking continues until $V_C = V_{\min}$ and then stops: thus the cluster of cells eventually contains a sizeble volume of dead cells' residues.

Corrections due to internal and environmental pH

The equations above include several correction factors that modify the enzyme activity according to the internal and the extracellular pH

pH_C = *pH inside cell C*

pH_c = *pH in the extracellular space*

We plan to include in the program a rather complete model of cellular acidity, but at the moment the internal pH is fixed and the external pH is computed from a simple model of the buffering capacity of the standard nutrient solutions [2]. If [AcL] is the lactate concentration, then the pH of the enviroment and of the extracellular spaces is

$$pH = 7.5443 - \frac{[AcL]}{BufCapEnv} \qquad (S.25)$$

where[2,12] *BufCapEnv = 0.19953 kg/m*^{3}.

The pH value is used to compute the following correction factors [2,13-16]:

t_{pH} = *correction of metabolic rates (depends on internal pH, and thus at the moment it is fixed)*

t_{p11} = *fine tuning of* p_{11} *(depends on internal pH, and thus at the moment it is fixed)*

$a2c$ = *correction to transport of glucose from extracellullar space into cell*

$c2a$ = *correction to transport of glucose from cell to extracellullar space*

$a2cA$ = *correction to transport of glutamine from extracellullar space into cell*

$c2aA$ = *correction to transport of glutamine from cell to extracellullar space*

$a2cAcL$ = *correction to transport of lactate from extracellullar space into cell*

$c2aAcL$ = *correction to transport of lactate from cell to extracellullar space*

The defining equations are:

$$t_{pH} = \frac{1}{2}\left[1 + \tanh\left(tpH\_slope \cdot pH_C - tpH\_thr\right)\right] \quad \textit{(S.26a)}$$

$$t_{p11} = \frac{1}{2}\left[1 + \tanh\left(tp11\_slope \cdot pH_C - tp11\_thr\right)\right] \quad \textit{(S.26b)}$$

$$a2c = \frac{1}{2}\left[1 + \tanh\left(a2c\_slope \cdot pH_c - a2c\_thr\right)\right] \quad \textit{(S.26c)}$$

$$c2a = \frac{1}{2}\left[1 + \tanh\left(c2a\_slope \cdot pH_C - c2a\_thr\right)\right] \quad \textit{(S.26d)}$$

$$a2cA = \frac{1}{2}\left[1 + \tanh\left(a2cA\_slope \cdot pH_c - a2cA\_thr\right)\right] \quad \textit{(S.26e)}$$

$$c2aA = \frac{1}{2}\left[1 + \tanh\left(c2aA\_slope \cdot pH_C - c2aA\_thr\right)\right] \quad \textit{(S.26f)}$$

$$a2cAcL = 2 - \tanh\left(a2cAcL\_slope \cdot pH_c - a2cAcL\_thr\right) \quad \textit{(S.26g)}$$

$$c2aAcL = 2 - \tanh\left(c2aAcL\_slope \cdot pH_C - c2aAcL\_thr\right) \quad \textit{(S.26h)}$$

These equations are smoothed versions of piecewise linear approximations of experimental data [2,13-16].

Other corrections

There are a few additional correction factors related to oxygen and ATP [1,2]:

h = *correction to glucose transport due to oxygen concentration*
$SensO2$ = *correction to glucose metabolism due to oxygen concentration*
$SensATP$ = *this factor is used to switch ATP production between oxidative phosphorylation and anaerobic glycolysis*

The equations that define these correction factors are [1,2]:

$$h = 0.5\left[1.3\left(1-\frac{m_{O2,C}}{V_C O2st}\right)+1\right]\cdot\left\{1+\tanh\left[100\left(1-\frac{m_{O2,C}}{V_C O2st}\right)\right]\right\} \\ +0.5\left\{1-\tanh\left[100\left(1-\frac{m_{O2,C}}{V_C O2st}\right)\right]\right\} \qquad (S.27)$$

$$SensO2 = \frac{m_{O2,C}}{V_C K_{O2} + m_{O2,C}} \qquad (S.28)$$

$$SensATP = \frac{1}{2}\left[1-\tanh\left(100\cdot\frac{\left(ATPOx - ATP_{St}\right)}{ATP_{St}}\right)\right] = \frac{1}{2}\left\{1-\tanh\left[100\cdot\left(\frac{ATPOx}{ATP_{St}}-1\right)\right]\right\} \qquad (S.29)$$

The equations for h and SensATP are smoothed versions of piecewise linear approximations, and ATP_{St} is a standard rate (this is a cellular parameter as well), that acts as a threshold that separates the two regimes of oxidative phosphorylation and anaerobic glycolysis. There are a two more parameters in these definitions, O2St, the standard oxygen concentration, and K_{O2}. ATPOx is the rate of ATP production from oxidative phosphorylation (defined above, in the section on ATP). The hyperbolic tangents that occur in the formulas do not have any special meaning, they are only practical approximations of smoothed step functions.

Cell phase transitions

The transitions from one cell phase to the next are regulated by a complex biochemical machinery that we include only in small part, and as it interacts in deep ways with cell metabolism.

Each cell in the simulation is in a certain phase of the cell's cycle, and there are specific rules that determine the transition from one phase to the next.

We define the following phases (sketched in fig. S1):

1. *G1m phase: G1 phase prior to the commitment to enter S phase (variable duration);*
2. *G1p phase: G1 phase after the commitment to enter S phase (variable duration);*
3. *S phase (variable duration);*
4. *G2 phase (variable duration);*
5. *M phase (fixed duration);*
6. *Death (indefinite duration);*

The dynamics of the G1m-G1p and of the G1p-S transitions is regulated by the pRb protein: pRb forms a complex with an enzyme E and carries 16 putative phosphorylation sites [17,18]. In this context, the enzymatic reaction catalyzed by E is a phenomenological model of the reactions controlled by the transcription factor E2F that associates with pRb in real cells.

The pRB-E complex is synthesized in the G2 phase and it is partitioned at random between the daughter cells at mitosis. At the beginning of the G1m phase the cyclin D protein (CycD) is expressed and it phosphorylates the pRB-E complex upon rapid association with specific cyclin-dependent kinases [17,18]. The phosphorylation event is assumed to occur following the reversible bimolecular interaction between cyclin D and the pRb complex: a detailed study has shown that the precise mechanism of pRb phosphorylation is irrelevant with respect to the dynamics of the system's response [17]. Upon partial phosphorylation of the pRb protein, a fraction of E molecules are released and catalyze a reaction whereby a substrate S is converted into a product P. When the concentration of S falls below the threshold $Thresh\_S\_start$ *the expression of the cyclin E protein (CycE) is activated and this marks the progression of the cell from the G1m phase to the following G1p-phase. CycE participates to pRb phosphorylation upon instantaneous association with specific cyclin-dependent kinases and leads to the hyperphosphorylation of the pRb with full E detachment. When the concentration of S falls below the threshold* $Thresh\_S\_stop$ *the cell progresses to the S-phase. At the end of the G1m- and G1p-phases, the cyclins CycD and CycE are destroyed by a proteolytic degradation that is assumed to occur faster than the considered reaction kinetics. The nature of pRb phosphorylation naturally*

introduces a threshold and a time delay in the reaction catalyzed by E with characteristic times comparable with the cell progression through the various cell cycle phases [19,20].

The program computes first the attachment probabability

$$p = \frac{1}{2N[A]_0}\left\{\left(N[A]_0 + [B]_0 + \frac{k_-}{k_+}\right) - \sqrt{\left(N[A]_0 + [B]_0 + \frac{k_-}{k_+}\right)^2 - 4N[A]_0[B]_0}\right\} \qquad (S.30)$$

and then the fraction and the number of molecules with at least k occupied phosphorylation sites:

$$P_k = P(\text{occupied sites} \geq k) = \sum_{l=k}^{N}\binom{N}{l}p^l(1-p)^{N-l} \qquad (S.31)$$

$$(N_A V[A])\cdot P_k = N_A V[A]\sum_{l=k}^{N}\binom{N}{l}p^l(1-p)^{N-l} \qquad (S.32)$$

where $[A]$ is the concentration of the pRb protein, and $[B]$ is the concentration of the phosphorylating complex, which - as explained above - we identify with the sum of the D and E cyclins (that we assume to be phosphorylated, in a cytoplasm with plenty of ATP). Here N and k are cell parameters (although in this case we do not expect them to change in different cell lines - see below).

Finally pRb_ONOFFratio is the ratio of the detachment-attachment rates (of the mediated phosphorylation process of pRb):

$\frac{k_-}{k_+}$ = *pRb_ONOFFratio*

We remark that all the quantities related to pRb phosphorylation process depend directly on pRb concentration, and thus on protein mass, and they do not require additional differential equations.

The concentration of the enzyme E (E2F) released by the configurational switch of the pRb protein is given by

$$[E]_0 = [A]_0 \sum_{l=k}^{N} \binom{N}{l} p^l (1-p)^{N-l} \qquad \textit{(S.33)}$$

and this determines the variation of the concentration of substrate S which leads to the threshold mechanism for the G1m-G1p commitment point

$$\frac{d[S]}{dt} \approx -\frac{k3MM \cdot [E]_0 [S]}{KmMM + [S]} \qquad \textit{(S.34)}$$

(where k3MM and kmMM are two additional cell parameters). The cell crosses the G1m-G1p commitment point when the concentration of the substrate S reaches a low value Thresh_S_start. A still lower value Thresh_S_stop corresponds to the G1-S checkpoint transition.

DNA synthesis takes place during the S-phase only, and the program contains a variable that takes care of synthesized DNA (measured in units of complete molecule). When this counter equals 1 the S-phase ends and the cell enters phase G2.

The G2-phase ends when there is a sufficient amount of cyclin A + cyclin B (at least CycXThr). Finally the M-phase has a fixed duration (M_T_MEAN).

In the program we also define a special cell phase which corresponds to death. We introduce an average death rate due to metabolites in the environment:

$$\textit{death rate} = a_R [AcL]_C \qquad \textit{(S.35)}$$

where $[AcL]_C$ is the lactate concentration inside the cell, so that the probability that a given cell survives during a timestep Δt is

$$\exp\left(-a_R [AcL]_C \cdot \Delta t\right) \qquad \textit{(S.36)}$$

(this is the just the conventional expression for the survival probability in toxicology[21]).

A cell can also die if there are not enough nutrients: we check for this condition at the start of each phase, and if the ATP content of the cell is less than a minimum mass ATPmin, the cell dies. The value ATPmin is calculated assuming that any residual cytoplasmic volume – which in our minimal model of the cell's volume depends on the total ATP content of the cell – must be at least as large as the total mitocondrial volume, then from the volume formula (S.22), we find

$$ATPmin = \frac{C2 \cdot Mit}{C1} \qquad (S.37)$$

B. Combined numerical solution of the diffusion and transport problem

In the previous section we have introduced several non-linear differential equations: these equations are used to simultaneously model both internal cell metabolism, and transport and diffusion. The equations have a rather conventional structure, as it often happens in biology, where the models are often concerned with enzyme action in the synthesis and destruction of molecular species, and in the regulation of transport of molecules into and out of the cell or cellular compartments.

The modeling of transport and diffusion is achieved by discretization of the diffusion problem: the cells' centers provide a natural discretization scaffolding and we use a Delaunay triangulation to define proximity relations [22-28]. Figure S3 shows schematically the cells and their extracellular spaces, together with two simple examples of triangulation, both in 2D and in 3D. The molecular species in the program can be grouped in three different classes. The first class includes substances that are neither transported outside the cell nor diffuse to neighboring cells, and obey differential equations with the generic form

$$\frac{dm_C}{dt} = M\left(m_C\right) \qquad \textit{(S.38)}$$

where m_C *is the mass of the substance in cell C, and* $M\left(m_C\right)$ *is a function that depends on the current state of the cell (e.g., in the case of stored glycogen, this function is implicitly defined by equation (S.5) and is equal to* $\left(g_3 + p_{11}\right) - \left(r_1 + r_2 + r_3\right)$*). In this case, the algorithmically stable solution derived from the implicit Euler method is*

$$m_C^{n+1} = m_C^n + \Delta t \cdot M\left(m_C^{n+1}\right) \qquad \textit{(S.39)}$$

where m_C^n *is the mass of substance in the cell at the n-th timestep.*

The second class of substances behaves like oxygen, which is metabolized by the cell, but is free to diffuse from cell to cell, and obeys equations with the generic form

$$\frac{dm_C}{dt} = M\left(m_C\right) + D\sum_{\langle B\rangle}\left(\frac{m_B}{V_B} - \frac{m_C}{V_C}\right)g_{BC} \qquad (S.40)$$

where in addition to the metabolic term there is a diffusion term as well (and the sum runs over all adjacent cells B – here adjacency is defined by the Delaunay triangulation). Now the algorithmically stable solution derived from the implicit Euler method is equivalent to the Backward Differentiation Method method for partial differential equations [29], and writes

$$m_C^{n+1} = m_C^n + \Delta t\left[M\left(m_C^{n+1}\right) + D\sum_{\langle B\rangle}\left(\frac{m_B^{n+1}}{V_B} - \frac{m_C^{n+1}}{V_C}\right)g_{BC}\right] \qquad (S.41)$$

The last class of substances is like glucose, which is transported across the cell membrane by facilitated diffusion. This case requires two equations per cell

$$\frac{dm_C}{dt} = M\left(m_C\right) + T\left(m_c, m_C\right) \qquad (S.42a)$$

$$\frac{dm_c}{dt} = -T\left(m_c, m_C\right) + D\sum_{\langle b\rangle}\left(\frac{m_b}{V_b} - \frac{m_c}{V_c}\right)g_{bc} \qquad (S.42b)$$

where the first equation describes internal metabolism and transport across the cell membrane into (or from) extracellular space, while the second equation describes the mass balance in the extracellular space, which exchanges mass with the cell and is linked to the rest of the system by diffusion (the extracellular space corresponding to cell C is denoted by a lowercase c, and the sum num runs over the adjacent extracellular spaces b). Now the algorithmically stable solution derived from the implicit Euler method produces the pair of equations

$$m_C^{n+1} = m_C^n + \Delta t\left[M\left(m_C^{n+1}\right) + T\left(m_c^{n+1}, m_C^{n+1}\right)\right] \qquad \textit{(S.43a)}$$

$$m_c^{n+1} = m_c^n + \Delta t\left[-T\left(m_c^{n+1}, m_C^{n+1}\right) + D\sum_{\langle b\rangle}\left(\frac{m_b^{n+1}}{V_b} - \frac{m_c^{n+1}}{V_c}\right) g_{bc}\right] \qquad \textit{(S.43b)}$$

Finally, taking into account all substances, we are left with a large set of nonlinear equations like (S.39), (S.41), (S.43a) and (S.43b). These equations are solved iteratively with Newton-Raphson steps [30]; these steps usually converge, but may occasionally fail if the mass is very close to zero, and in this case they are substituted by steps performed with the secant method [30]. The convergence condition is that for all masses the inequality

$$\left|m^{n+1} - m^n\right| < \varepsilon \cdot \frac{m^{n+1} + m^n}{2} \qquad \textit{(S.44)}$$

holds, where ε is a given precision, i.e., the difference between two successive values in the iteration must be less than a given fraction of the estimated mass.

C. Biomechanical modeling

Mechanical interactions between cells are - if possible - even more complex than the biochemical network described above, and we know that cells are viscoelastic structures which are actively shaped by the cytoskeleton [31].

The simulation work faces the following difficulties:

- *existing theoretical models capture only part of the actual features of cells and are not really applicable to the complex reality of cells in clusters (e.g., reference [32] describes an interesting model of erythrocytes, which are however both simpler and different from other human cells; the model is also inapplicable here, because it would lead to an exceedingly high computational complexity);*

- *many measurements are inapplicable to the simulation of cells (pipette aspiration techniques [33-35], as well as optical and magnetic tweezers measurements [36,37] and experiments that utilize atomic force microscopes [38-45], provide interesting data, but in a contexts that are different from those that we want to simulate);*
- *cells adapt their shape both to environment and to internal events (the most notable of which is obviously the mitosis)*
- *cells live in a high-viscosity environment where both the internal viscosity of cells and the external viscosity of the extracellular environment matter.*

Clearly, phenomenological approximations and parameterizations carry even more weight in this context. We approximate the mechanical behavior of cells as follows:

- *cells are (soft) spheres, and are characterized by the position of their center (a 3D vector) and by their radius;*
- *we assume that cells are close-packed, and this leads to the introduction of an effective radius that is important in repulsive interactions with other cells;*
- *adhesion forces are usually very short-ranged, but here we assume a much larger range, and in this way we account for the cell's extensibility and deformation;*
- *we assume that cells are surrounded by viscous material similar to that found in the extracellular matrix [46];*

In the following paragraphs we explain all this in further detail.

Cell-cell forces

We use a parameterization of the cell-cell forces that is somewhat similar to that used in references [47] and [48]. For small deformations of the cell

membrane, it is reasonable to assume that it behaves as in the Hertz problem (interaction of two spherical membranes) or as in the Boussinesq problem (axisymmetric pressure on a flat membrane) [49,50]: in both cases the force is proportional to $k_C |x|^{3/2}$*, where x is the relative deviation from the equilibrium position and* k_C *is a constant related to the problem parameters. In the Hertz problem the intensity of the force is*

$$F_{12} = \frac{\sqrt{R_1 R_2}\left(R_1 + R_2\right)}{\frac{3}{4}\left(\frac{1-\nu_1^2}{E_1} + \frac{1-\nu_2^2}{E_2}\right)}\left(\frac{R_1 + R_2 - d}{R_1 + R_2}\right)^{3/2} \qquad (S.45)$$

where R denotes the radius, d is the distance of the two spheres' centers, E is Young's modulus, ν *is Poisson's ratio, and the subscripts denote sphere 1 or 2, so that in this case*

$$k_C = \frac{\sqrt{R_1 R_2}\left(R_1 + R_2\right)}{\frac{3}{4}\left(\frac{1-\nu_1^2}{E_1} + \frac{1-\nu_2^2}{E_2}\right)} \qquad (S.46)$$

and

$$x = \frac{d - \left(R_1 + R_2\right)}{\left(R_1 + R_2\right)} \qquad (S.47)$$

Under compression the repulsive force (S.45) can be quite large, especially after mitosis: such large forces are not observed in real cells, and thus we assume that at small enough separations d the force flattens out and has a constant modulus. We set the position of this flattening so that we obtain the observed duration of mitosis.

When cells are drawn apart the force is attractive, because of adhesion molecules on the cell membrane [51]. The force range of the adhesion molecules is quite small (tens of nanometers) but here we assume a far larger range, as

large as a few microns: in this way we account – albeit phenomenologically – for shape deformations in the case of attractive forces. Cell-cell adhesion depends on the number of links between adhesion molecules on both cell membranes [52], and is a probabilistic process: if we assume a roughly Gaussian probability density which depends on the relative deviation ***x****, then*

$$p(x)=\frac{1}{\sqrt{2\pi\sigma^2}}\exp\left(-\frac{(x-x_0)^2}{2\sigma^2}\right) \qquad \textit{(S.48)}$$

is the probability density that a link is detached at relative distance ***x****, where* x_0 *and* σ^2 *are parameters that must be adjusted. This means that the average number of detached links at relative distance* ***x*** *is proportional to the cumulative probability*

$$P(x)=\int_0^x p(x')dx'=\int_0^x \frac{1}{\sqrt{2\pi\sigma^2}}\exp\left(-\frac{(x'-x_0)^2}{2\sigma^2}\right)dx'\approx\frac{1}{2}\left[1+\operatorname{erf}\left(\frac{x-x_0}{\sqrt{2}\sigma}\right)\right] \qquad \textit{(S.49)}$$

Computing the error function in the simulation program leads to an increase of the computational load, and thus we replace the expression (S.49) with the approximate formula

$$P(x)\approx\frac{1}{2}\left[1+\tanh\left(\sqrt{\frac{2}{\pi\sigma^2}}(x-x_0)\right)\right] \qquad \textit{(S.50)}$$

(the hyperbolic tangent approximates the error function everywhere to better than 2% precision). Finally we take a force that is proportional both to the number of links and to the previously calculated shape $k_C|x|^{3/2}$*:*

$$F_a(x)\approx\frac{1}{2}\left[1+\tanh\left(\sqrt{\frac{2}{\pi\sigma^2}}(x-x_0)\right)\right]k_C|x|^{3/2} \qquad \textit{(S.51)}$$

The values of the parameters E, ν, $\sqrt{\frac{2}{\pi\sigma^2}}$, and x_0 are listed in table S4 and the modulus of the force is shown in figure S4; the direction of the force is always along the line that connects the cell centers.

Brownian motion

Cells are small and Brownian motion, i.e. random molecular forces, could play an important role, however in the high viscosity medium of a cell spheroid we find that Brownian motion is negligible. It is easy to estimate this from the 1D Langevin equation for Brownian motion along x:

$$m\frac{d^2x}{dt^2} = -\gamma\frac{dx}{dt} + n(t) \qquad \textit{(S.52)}$$

where m is the cell's mass, γ is the friction coefficient, and $n(t)$ is a white noise process which is associated to the molecular thermal motion. It can easily be shown that the mean square fluctuation [53] is

$$\left\langle x^2(t)\right\rangle = 2\frac{kT}{\gamma}t \qquad \textit{(S.53)}$$

and does not depend on the particle mass. Now if we take cells in a high-viscosity environment, $\eta \approx 1\ \mathrm{Pa{\cdot}s}$, and estimate the friction coefficient using the Stokes-Einstein formula for a cell with radius r ≈ 5 μm, we find $\gamma = 6\pi\eta r \approx 9.4{\cdot}10^{-5}\ \mathrm{N{\cdot}s/m}$, then at T ≈ 300 K the mean square fluctuation and the RMS fluctuation are

$$\left\langle x^2(t)\right\rangle \approx \left(8.8{\cdot}10^{-17}\ \mathrm{m^2/s}\right)t \qquad \textit{(S.54a)}$$

$$\sqrt{\left\langle x^2(t)\right\rangle} \approx \left(9.4\ \mathrm{nm}/\sqrt{\mathrm{s}}\right)\sqrt{t} \qquad \textit{(S.54b)}$$

so that it takes a time $t \approx 10^4$ s for an RMS fluctuation of 1 μm to develop. It follows that the Brownian motion of cells is negligible in the case a simulation of tumor spheroids with reasonable time steps (the time step cannot in any case be longer than the duration of the shortest phase, which is the M-phase and lasts ~ 2000 s. moreover time steps should be shorter than ~ 100 s to provide a good sampling schedule of most biochemical processes).

Dynamical equations

The dynamical equations for the motion of cells are similar to those of dissipative particle dynamics [54,55], without stochastic terms (since Brownian motion is negligible):

$$m_n \frac{d\mathbf{v}_n}{dt} = -\gamma \mathbf{v}_n - \sum_k \gamma_{n,k} \frac{(\mathbf{v}_n - \mathbf{v}_k)\cdot(\mathbf{r}_n - \mathbf{r}_k)}{|\mathbf{r}_n - \mathbf{r}_k|^2}(\mathbf{r}_n - \mathbf{r}_k) + \mathbf{F}_n + \sum_k \mathbf{F}_{n,k} \qquad (S.55)$$

where the indices n and k denote cells, the sums $\sum_k$ are over all neighboring cells, m_n denotes the mass, $\mathbf{r}_n$ and $\mathbf{v}_n$ are position and velocity vectors of the cell, γ is the environmental friction coefficient, $\gamma_{n,k}$ is the friction between the n-th and the k-th cell, $\mathbf{F}_n$ is an external force (like gravity), and finally $\mathbf{F}_{n,k}$ is the force that cell k exerts on cell n.

Analysis of the simplified dynamical equations

The equations (S.55) include a cell-cell friction that acts only along the line that joins the cells' centers, and if we relax this constraint, the equations become somewhat simpler and easier to analyze:

$$m_n \frac{d\mathbf{v}_n}{dt} = -\gamma \mathbf{v}_n - \sum_k \gamma_{n,k}\left(\mathbf{v}_n - \mathbf{v}_k\right) + \mathbf{F}_n + \sum_k \mathbf{F}_{n,k} \qquad \textit{(S.56)}$$

If there are N cells, then the system of equations (S.56) is a linear system of 3N ordinary differential equations, and we can solve it using an implicit-explicit Euler method [56,57] (implicit over velocities, explicit over intercellular forces which are assumed to change slowly), so that the discretized version of the differential equation now writes

$$\begin{aligned}\mathbf{v}_n(t+\Delta t) = \mathbf{v}_n(t) + \Bigg\{ &-\frac{\gamma}{m_n}\mathbf{v}_n(t+\Delta t) - \frac{1}{m_n}\sum_k \gamma_{n,k}\left(\mathbf{v}_n(t+\Delta t) - \mathbf{v}_k(t+\Delta t)\right) \\ &+ \frac{1}{m_n}\left[\mathbf{F}_n(t) + \sum_k \mathbf{F}_{n,k}(t)\right]\Bigg\}\Delta t\end{aligned} \qquad \textit{(S.57a)}$$

$$\mathbf{r}_n(t+\Delta t) = \mathbf{r}_n(t) + \mathbf{v}_n(t+\Delta t)\Delta t \qquad \textit{(S.57b)}$$

Equations (S.57a) are a linear system that could in principle be solved using one of the standard methods [29], however the computational complexity of the standard exact solutions is $\mathrm{O}\left((3N)^3\right)$*, and since N can be of the order of several hundreds of thousands or a few millions of cells, the computational burden of the exact solutions is huge. For this reason we resort to an approximate, iterative method (this holds for the solution of the complete differential system (S.55) as well). Formally solving the equations (S.57a) for* $\mathbf{v}_n(t+\Delta t)$*, we find*

$$\mathbf{v}_n(t+\Delta t) = \frac{\mathbf{v}_n(t) + \left\{\sum_k \gamma_{n,k}\mathbf{v}_k(t+\Delta t) + \left[\mathbf{F}_n(t) + \sum_k \mathbf{F}_{n,k}(t)\right]\right\}\frac{\Delta t}{m_n}}{1 + \left(\gamma + \sum_k \gamma_{n,k}\right)\frac{\Delta t}{m_n}} \qquad \textit{(S.58)}$$

and we can rewrite this as

$$\mathbf{v}_n^{(i+1)}(t+\Delta t)=\frac{\mathbf{v}_n(t)+\left\{\sum_k \gamma_{n,k}\mathbf{v}_k^{(i)}(t+\Delta t)+\left[\mathbf{F}_n(t)+\sum_k \mathbf{F}_{n,k}(t)\right]\right\}\frac{\Delta t}{m_n}}{1+\left(\gamma+\sum_k \gamma_{n,k}\right)\frac{\Delta t}{m_n}}$$
$$=\frac{\sum_k \gamma_{n,k}\mathbf{v}_k^{(i)}(t+\Delta t)\frac{\Delta t}{m_n}}{1+\left(\gamma+\sum_k \gamma_{n,k}\right)\frac{\Delta t}{m_n}}+\frac{\mathbf{v}_n(t)+\left[\mathbf{F}_n(t)+\sum_k \mathbf{F}_{n,k}(t)\right]\frac{\Delta t}{m_n}}{1+\left(\gamma+\sum_k \gamma_{n,k}\right)\frac{\Delta t}{m_n}} \qquad (S.59)$$

where the index i identifies the i-th iteration. It is easy to see that the iterative algorithm converges: we start by subtracting two successive iterations

$$\mathbf{v}_n^{(i+2)}(t+\Delta t)-\mathbf{v}_n^{(i+1)}(t+\Delta t)=\frac{\sum_k \gamma_{n,k}\left[\mathbf{v}_k^{(i+1)}(t+\Delta t)-\mathbf{v}_k^{(i)}(t+\Delta t)\right]\frac{\Delta t}{m_n}}{1+\left(\gamma+\sum_k \gamma_{n,k}\right)\frac{\Delta t}{m_n}} \qquad (S.60)$$

from which we obtain the series of inequalities

$$\max_n\left|\mathbf{v}_n^{(i+2)}(t+\Delta t)-\mathbf{v}_n^{(i+1)}(t+\Delta t)\right|\le\max_n\frac{\sum_k \gamma_{n,k}\left|\mathbf{v}_k^{(i+1)}(t+\Delta t)-\mathbf{v}_k^{(i)}(t+\Delta t)\right|\frac{\Delta t}{m_n}}{1+\left(\gamma+\sum_k \gamma_{n,k}\right)\frac{\Delta t}{m_n}}$$
$$\le\max_n\frac{\sum_k \gamma_{n,k}\frac{\Delta t}{m_n}}{1+\left(\gamma+\sum_k \gamma_{n,k}\right)\frac{\Delta t}{m_n}}\cdot\max_n\left|\mathbf{v}_k^{(i+1)}(t+\Delta t)-\mathbf{v}_k^{(i)}(t+\Delta t)\right|$$
$$=c\cdot\max_n\left|\mathbf{v}_k^{(i+1)}(t+\Delta t)-\mathbf{v}_k^{(i)}(t+\Delta t)\right| \qquad (S.61)$$

and convergence follows when we notice that

$$c=\max_n\frac{\sum_k \gamma_{n,k}\frac{\Delta t}{m_n}}{1+\left(\gamma+\sum_k \gamma_{n,k}\right)\frac{\Delta t}{m_n}}<1 \qquad (S.62)$$

i.e., the maximum difference $\max_n \left| \mathbf{v}_k^{(i+1)}(t+\Delta t) - \mathbf{v}_k^{(i)}(t+\Delta t) \right|$ *between successive iterations approaches zero for large i.*

In the section on Brownian motion we have already taken a rather high environmental viscosity $\eta \approx 1\ \text{Pa·s}$*, which corresponds to the viscosity of the hyaluronate and collagen in extracellular spaces [58,59]; the viscosity of cell-cell interactions is even higher [31-45], of the order of* $\eta \approx 200\ \text{Pa·s}$*. If we take cells with radius r ≈ 5 μm, so that m ≈ 5·10*$^{-13}$ *kg, we note that* $\gamma \approx 9.4 \cdot 10^{-5}\ \text{N·s/m}$ *and that* $\sum_k \gamma_{n,k} \approx 0.02\ \text{N·s/m}$*, and we let* Δt *= 100 s, then we find* $c \approx 0.995$*. Using this value we can estimate the worst-case convergence speed: from equation (S.62) we see that we achieve a ten-fold accuracy improvement after s steps, so that* $c^s = 1/10$*, i.e.,* $s = -1/\log_{10} c \approx 500$*. We remark here that this estimate depends critically on the environmental viscosity: we assume the viscosity of hyaluronate, but if we took a lower viscosity environment, like water with* $\eta \approx 0.001\ \text{Pa·s}$*, we would find* $\gamma \approx 9.4 \cdot 10^{-8}\ \text{N·s/m}$ *and* $c \approx 0.999995$*, so that s ≈ 500000. In the case of a water environment, convergence of the iterative algorithm is so slow that it becomes totally impractical, but fortunately we can stick to the other, more favourable case.*

Solution of the complete nonlinear system of dynamical equations

The simplified equations (S.56) are useful to analyze algorithmic convergence, but the program utilizes the full equations (S.55). In this case the equations obtained from the implicit-explicit Euler method for the x-component of the velocity vector are

$$
\begin{aligned}
v_{n,x}(t+\Delta t)&\left[1+\frac{\Delta t}{m_n}\left(\gamma+\sum_k \gamma_{n,k}\frac{(r_{n,x}-r_{k,x})}{|\mathbf{r}_n-\mathbf{r}_k|^2}(r_{n,x}-r_{k,x})\right)\right]\\
&+v_{n,y}(t+\Delta t)\frac{\Delta t}{m_n}\sum_k \gamma_{n,k}\frac{(r_{n,y}-r_{k,y})}{|\mathbf{r}_n-\mathbf{r}_k|^2}(r_{n,x}-r_{k,x})\\
&+v_{n,z}(t+\Delta t)\frac{\Delta t}{m_n}\sum_k \gamma_{n,k}\frac{(r_{n,z}-r_{k,z})}{|\mathbf{r}_n-\mathbf{r}_k|^2}(r_{n,x}-r_{k,x})\\
&=v_{n,x}(t)+\frac{\Delta t}{m_n}\left[\sum_k \gamma_{n,k}\frac{\mathbf{v}_k(t+\Delta t)\cdot(\mathbf{r}_n-\mathbf{r}_k)}{|\mathbf{r}_n-\mathbf{r}_k|^2}(r_{n,x}-r_{k,x})+F_{n,x}+\sum_k F_{n,k;x}\right]
\end{aligned}
\qquad (S.63)
$$

(similar equations hold for the y and z component of the velocity). These equations can also be put into matrix form

$$
\mathbf{M}\cdot\mathbf{v}_n(t+\Delta t)=\mathbf{b} \qquad (S.64)
$$

where

$$
\mathbf{b}=\mathbf{v}_n(t)+\frac{\Delta t}{m_n}\left(\sum_k \gamma_{n,k}\frac{\mathbf{v}_k(t+\Delta t)\cdot(\mathbf{r}_n-\mathbf{r}_k)}{|\mathbf{r}_n-\mathbf{r}_k|^2}(\mathbf{r}_n-\mathbf{r}_k)+\mathbf{F}_n+\sum_k \mathbf{F}_{n,k}\right) \qquad (S.65)
$$

and

$$
\mathbf{M}=\begin{pmatrix}
1+\frac{\Delta t}{m_n}\left(\gamma+\sum_k \gamma_{n,k}\frac{(r_{n,x}-r_{k,x})^2}{|\mathbf{r}_n-\mathbf{r}_k|^2}\right) & \frac{\Delta t}{m_n}\sum_k \gamma_{n,k}\frac{(r_{n,y}-r_{k,y})}{|\mathbf{r}_n-\mathbf{r}_k|^2}(r_{n,x}-r_{k,x}) & \frac{\Delta t}{m_n}\sum_k \gamma_{n,k}\frac{(r_{n,z}-r_{k,z})}{|\mathbf{r}_n-\mathbf{r}_k|^2}(r_{n,x}-r_{k,x})\\
\frac{\Delta t}{m_n}\sum_k \gamma_{n,k}\frac{(r_{n,x}-r_{k,x})}{|\mathbf{r}_n-\mathbf{r}_k|^2}(r_{n,y}-r_{k,y}) & 1+\frac{\Delta t}{m_n}\left(\gamma+\sum_k \gamma_{n,k}\frac{(r_{n,y}-r_{k,y})^2}{|\mathbf{r}_n-\mathbf{r}_k|^2}\right) & \frac{\Delta t}{m_n}\sum_k \gamma_{n,k}\frac{(r_{n,z}-r_{k,z})}{|\mathbf{r}_n-\mathbf{r}_k|^2}(r_{n,y}-r_{k,y})\\
\frac{\Delta t}{m_n}\sum_k \gamma_{n,k}\frac{(r_{n,x}-r_{k,x})}{|\mathbf{r}_n-\mathbf{r}_k|^2}(r_{n,z}-r_{k,z}) & \frac{\Delta t}{m_n}\sum_k \gamma_{n,k}\frac{(r_{n,y}-r_{k,y})}{|\mathbf{r}_n-\mathbf{r}_k|^2}(r_{n,z}-r_{k,z}) & 1+\frac{\Delta t}{m_n}\left(\gamma+\sum_k \gamma_{n,k}\frac{(r_{n,z}-r_{k,z})^2}{|\mathbf{r}_n-\mathbf{r}_k|^2}\right)
\end{pmatrix}
\qquad (S.66)
$$

The formal solution of the equations (S.64) is

$$\mathbf{v}_n(t+\Delta t) = \mathbf{M}^{-1}\cdot\mathbf{b} = \mathbf{M}^{-1}\cdot\left[\mathbf{v}_n(t) + \frac{\Delta t}{m_n}\left(\sum_k \gamma_{n,k}\frac{\mathbf{v}_k(t+\Delta t)\cdot(\mathbf{r}_n-\mathbf{r}_k)}{|\mathbf{r}_n-\mathbf{r}_k|^2}(\mathbf{r}_n-\mathbf{r}_k) + \mathbf{F}_n + \sum_k \mathbf{F}_{n,k}\right)\right] \quad (S.67)$$

and this equation can be recast in the iterative form

$$\mathbf{v}_n^{(i+1)}(t+\Delta t) = \mathbf{M}^{-1}\cdot\mathbf{b} = \mathbf{M}^{-1}\cdot\left[\mathbf{v}_n(t) + \frac{\Delta t}{m_n}\left(\sum_k \gamma_{n,k}\frac{\mathbf{v}_k^{(i)}(t+\Delta t)\cdot(\mathbf{r}_n-\mathbf{r}_k)}{|\mathbf{r}_n-\mathbf{r}_k|^2}(\mathbf{r}_n-\mathbf{r}_k) + \mathbf{F}_n + \sum_k \mathbf{F}_{n,k}\right)\right] \quad (S.68)$$

where once again the index i identifies the i-th iteration.

Mitosis

When a cell completes the M-phase it is replaced by two daughter cells. The program selects a random direction for the axis that joins the centers of the daughter cells, and then it computes the positions of their centers. Since the total volume of the daughter cells is equal to the volume of the mother, the radius of each daughter cell is roughly equal to 80% of the radius R_0 *of the mother, i.e., the distance between the new centers is about* $0.4\,R_0$ *(see figure S5). Here the centers are only representative of an "average" cell position and are used to compute forces; the new cells are actually compressed and deformed to fit in the original volume.*

The distance $0.4\,R_0$ *also sets the maximum value of the repulsive force: indeed when the daughter cells are not surrounded by other cells, the distance of their centers must increase from about* $0.4\,R_0$ *to* $1.6R_0$ *in a time equal to the duration of the M-phase. For cells with radius* $R_0 \approx 5\ \mu\mathrm{m}$ *this means that the distance traveled by each cell is about 3 μm. If we take the total duration of the M-phase about 2000 s, then the average speed of each cell is about 1.5 nm/s, and the*

average repulsive force is $F = \gamma v \approx$ *30 pN, taking a cell-cell viscosity* $\eta \approx 200$ Pa·s *as above.*

D. List of biophysical constants, parameter values

Table S1: list of cell status variables in the simulation program.

basic informations	
name	*cell name (identifier)*
mark	*optional label to select a subset of cells (i.e., cells with a marker of some kind)*
type	*cell phenotype (cell-specific list of parameters)*
T	*local cell temperature (not used now)*
cell state	
phase	*cell phase*
death_condition	*label that records the reason of death (valid for dead cells only)*
age	*cell age (since birth)*
phase_age	*age of present cell phase*
age_mother	*age of mother at mitosis*
n_mitosis	*number of cell generations since start of simulation*
geometric and topological informations	
x,y,z	*cell position vector*
vx, vy, vz	*cell velocity vector*
r	*cell radius*
surface	*cell surface*
volume	*cell volume*
mass	*cell mass*
volume_extra	*volume of extracellular space surrounding cell*
neigh	*number of neighbors*
vneigh	*list of neighboring cells*
vdist	*distances to neighboring cells*
vcsurf	*contact surfaces with neighboring cells*
gnk	*vector of geometric factors*
contact_surf	*total contact area with neighboring cells*
isonCH	*boolean variable that is true if the cell is in contact with the environment*
env_surf	*cell-environment contact area*
metabolic variables	
pHi	*internal pH*
M	*number of mitochondria*
G	*mass of glucose inside cell*
G6P	*mass of G6P inside cell*
O2	*mass of oxygen inside cell*
store	*mass of glycogen inside cell*
A	*mass of glutamine inside cell*
AcL	*mass of lactic acid inside cell*
protein	*total mass of proteins inside cell*
prot_rate	*total protein production rate*
DNA	*total amount of DNA produced by replication*
DNA_rate	*DNA replication rate*

Table S1: list of cell status variables in the simulation program. (ctd.)

rates	
GAbsRate	*glucose absorption rate*
GConsRate	*glucose consumption rate*
AAbsRate	*glutamine absorption rate*
AConsRate	*glutamine consumption rate*
StoreFillRate	*glycogen production rate*
StoreConsRate	*glycogen consumption rate*
AcLRate	*lactic acid production rate*
AcLOutRate	*lactic acid expulsion rate*
ATP-related variables	
ATP_St	*standard ATP*
ATP_Ox	*ATP production rate (by oxidative phosphorylation)*
ATP_NOx	*ATP production rate (by anaerobic glycolysis)*
ATP2	*ATP production rate from the glycogen store*
ATP3	*ATP production rate from glutamine*
ConsATP	*total ATP consumption rate due to metabolic activity*
ConsATP_1	*ATP consumption rate associated to mitochondrial activity and other volume-dependent processes*
ConsATP_2	*ATP consumption rate associated to the production of proteins*
ConsATP_3	*ATP consumption rate associated to DNA production*
ConsATP_4	*(reserved for future use)*
ConsATP_5	*ATP consumption rate associated to mitochondrial proliferation*
ATPtot	*total ATP variation rate (this is the sum of all production and consumption rates)*
ATPp	*ATP pool (total mass of ATP inside cell)*
ATPmin	*minimum tolerable ATPp level (it depends on the size of cell: larger cells have a larger ATPmin level)*
ATPstart	*this variable stores the initial value of ATPp in the newly born cell*
ATPprod	*ATP produced in cell during the last simulation step*
ATPcons	*ATP consumed in cell during the last simulation step*
variables that characterize the extracellular space around a cell	
pH	*pH in extracellular space*
G_extra	*mass of glucose in extracellular space*
A_extra	*mass of glutamine in extracellular space*
AcL_extra	*mass of lactic acid in extracellular space*
other variables	
SensO2	*fraction of oxygen available with respect to request*
ConsO	*oxygen consumption rate*
proteins and DNA	
DNA_spread	*individual variation of DNA production rate (this is a quite rough modeling of variable DNA synthesis because of individual DNA damages)*
M_T	*average duration of M-phase*
pRb	*total pRb mass inside cell*
ConcS	*molar concentration of substrate needed for thresholds*
cyclinD	*total cyclin D mass inside cell*
cyclinE	*total cyclin E mass inside cell*
cyclinX	*total mass of A and B cyclins inside cell*
NpRbk	*total number of active pRb molecules*

Table S2 : list of the biophysical constants that are hard-coded in the program

Name of constant	*Value*	*Description*
N_{AV}	*6.022e23*	*Avogadro constant*
Faraday	*96485.34 Coulomb*	*Faraday constant*
PM_G	*0.18 kg*	*Molecular weight of glucose*
PM_{ATP}	*0.507 kg*	*Molecular weight of ATP*
PM_{O2}	*0.032 kg*	*Molecular weight of O_2*
PM_{AcL}	*0.090 kg*	*Molecular weight of lactate*
PM_{G6P}	*0.270 kg*	*Molecular weight of G6P*
PM_{pRb}	*110. kg*	*Molecular weight of pRb*
PM_A	*0.146 kg*	*Molecular weight of glutamine*
PM_{prot}	*66.476 kg*	*Average molecular weight of proteins*
$PM_{cyclinD}$	*33.729 kg*	*Molecular weight of cycline D*
$PM_{cyclinE}$	*47.077 kg*	*Molecular weight of cycline E*
$PM_{cyclinX}$	*52. kg*	*Molecular weight of cycline A+B*
$Gibbs_{ATP}$	*$3.1 \cdot 10^4$ J/mol*	*Gibbs free energy from ATP hydrolysis*

The following tables list the parameters that represent the the environment and the cell phenotype, and that the program reads from external files, and the diffusion and viscosity constants, that are still hard-coded in the simulation program:

Table S3: Starting values for the environmental concentrations (standard atmospheric pressure and culture medium)

Substance	*Environmental concentration*
O_2	*0.007 kg/m^3*
glucose	*0.9 kg/m^3*
glutamine	*0.4 kg/m^3*

Table S4: Phenotype (cell parameters)

Parameter name	Value	Notes and references
VMAX1	$2\cdot10^{-9}$ kg·s^{-1}·m^{-2}	[60].
VMAX2	$1.2\cdot10^{-19}$ kg·s^{-1}	[61].
VMAX22	$1.2\cdot10^{-18}$ kg·s^{-1}	[61].
VMAXA	$1\cdot10^{-9}$ kg·s^{-1}·m^{-2}	[62].
VMAXP	$3\cdot10^{-19}$ kg·s^{-1}	Estimated in this work by considering that the average protein content of a cell is approx. $2.6\cdot10^{-14}$ kg
$VMAXP_A$	$1.018\cdot10^{-20}$ kg·s^{-1}	Estimated in this work by considering that glutamine mass is approx. 5% of the total protein mass in the cell. See also [63].
$VMAXP_{ATP}$	$1.81\cdot10^{-18}$ kg·s^{-1}	Estimated in this work by considering albumin (585 aminoacids, 584 aminoacid bonds) as the "average protein" and that 2 molecules of ATP are required for each bond.
VMAXDNA	$5\cdot10^{-5}$ molecules/s	Estimated in this work taking $3\cdot10^{9}$ base pairs/cell and assuming that on average the S-phase lasts 25000 s
$VMAXDNA_A$	$5.847\cdot10^{-20}$ kg·s^{-1}	Estimated in this work by considering that the entire duplication of the DNA requires $6\cdot10^{9}$ glutamine molecules. See also [64].
$VMAXDNA_{ATP}$	$9.01\cdot10^{-20}$ kg·s^{-1}	Estimated in this work by considering that, on average, the free energy of each phosphodiester bond in DNA is 5.3 kcal/mole. See, e.g., [65].
VMAXM	$2\cdot10^{-3}$ mitochondria/s	Estimated in this work, assuming an average number of 150 mitochondria per cell. See, e.g., [66,67].
$VMAXM_A$	$7.3\cdot10^{-23}$ kg·s^{-1}	Estimated in this work by considering that, on average, there are 1000 molecules of mitochondrial DNA/cell and that each molecule is 16000 bp. See, e.g., [66].
$VMAXM_{ATP}$	$1.125\cdot10^{-22}$ kg·s^{-1}	Estimated in this work as for $VMAXDNA_{ATP}$. See above.
K_1	0.27024 kg·m^{-3}	[60].
K_2	1.80 kg·m^{-3}	[61].
K_{22}	$1.80\cdot10^{-2}$ kg·m^{-3}	[61].
KmA	0.023798 kg·m^{-3}	[68].
Ka	0.054 kg·m^{-3}	Derived from fitting the model to data in [69]. See also [1].
Kmc	0.096 kg·m^{-3}	Derived from fitting the model to data in [69]. See also [1].
Kmd	$1.8\cdot10^{-2}$ kg·m^{-3}	Derived from fitting the model to data in [69]. See also [1].
KmO2	$7\cdot10^{-4}$ kg·m^{-3}	Derived from fitting the model to data in [69]. See also [1].
Kmp	$6.7\cdot10^{-3}$ kg·m^{-3}	See ref. 2. In the present case, however, the value is expressed in concentration units.
KmDNA	$4.5\cdot10^{-4}$ (kg·m^{-3})^2	See [2]. In the present case, however, the value is expressed in concentration units.
KmM	$1.46\cdot10^{-2}$ (kg·m^{-3})^2	Estimated in this work as for $VMAXM_A$ (see above). This value is calculated at equilibrium for standard concentrations.
coeffg1	$7.5\cdot10^{-3}$ s^{-1}	Derived from fitting the model to data in [69]. See also [1].
coeffg2	$1.08\cdot10^{-3}$ s^{-1}	Derived from fitting the model to data in [69]. See also [1].
coeffg3	$6.7\cdot10^{-4}$ s-1	Derived from fitting the model to data in [69]. See also [1].
coeffr1	$3\cdot10^{-20}$ kg·s-1	Derived from fitting the model to data in [69]. See also [1].
ATP_{St}	$2.3\cdot10^{-18}$ kg·s-1	Derived from fitting the model to data in [69]. See also [1].
V_{min}	$0.9\cdot10^{-16}$ m^3	Derived from data in [70] considering that the cell nucleus occupies between 4% and 14% of cell volume. See also [1].
DVap	$3\cdot10^{-6}$ s^{-1}	Estimated in this work. See also [11].
VMAXAcL	$9.58\cdot10^{-8}$ kg·s^{-1}·m^{-2}	[71-73].
KmAcL	0.40536 kg·m^{-3}	[71-73].
M_T_MEAN	1800. s	[1].
v_{work}	$1.5\cdot10^{-2}$ kg· s^{-1}·m^{-3}	Estimated in this work by fitting of tumor cell growth data

Table S4: Phenotype (cell parameters). (ctd.)

Parameter name	Value	Notes and references

k_pRb	*10*	*[17].*
N_pRb	*16*	*[17].*
pRb_ONOFFratio	$1 \cdot 10^{-6}$	*[74].*
pRb_fraction	$1.5 \cdot 10^{-2}$	*This paper by data fitting. See also [2].*
cyclinD_fraction	$1 \cdot 10^{-2}$	*This paper by data fitting. See also [2].*
cyclinE_fraction	$3 \cdot 10^{-3}$	*This paper by data fitting. See also [2].*
cyclinX_fraction	$1.4 \cdot 10^{-2}$	*This paper by data fitting. See also [2].*
ConcS_0	$1 \cdot 10^{-3}$ *mol/l*	*[19,20].*
Thresh_S_start	*0.8*	*[2].*
Thresh_S_stop	*0.05*	*[2].*
k3MM	$1 \cdot 10^{4}$ s^{-1}	*[19,20].*
KmMM	$1 \cdot 10^{-3}$ *mol/l*	*[19,20].*
NUCLEAR_OBJ	*46*	*Estimated in this work by fitting of tumor cell growth data*
ClusteringFactor	*15*	*Estimated in this work by fitting of tumor cell growth data*
CycXThr	$0.8 \cdot 10^{-16}$ *kg*	*[2].*
C1	0.074 m^3 kg^{-1}	*Inverse of standard ATP concentration (see above)*
C2	$2 \cdot 10^{-19}$ m^{-3}	*Average volume of mitochondria. See [75].*
a_R	$1.2 \cdot 10^{-5}$ $m^3 \cdot kg^{-1} \cdot s^{-1}$	*Estimated in this work by fitting of tumor cell growth data*
YoungMod	*1000. Pa*	*Young's modulus. The elastic properties of cells are quite variable: according to [38], Young's modulus of living cells spans a very large range (1-100 kPa). Here we choose a value which is at lowest extreme of this range, and agrees with measurements in ref. [41,42,44,45].*
PoissonRatio	*0.5*	*Poisson's ratio. This number relates axial and transverse strain and lies in the range (-1,0.5) [76]. Here we choose the highest possible value, 0.5, which corresponds to incompressible cells (as in [44]).*
density	1070. $kg \cdot m^{-3}$	*[77,78].*
viscosity	*200. Pa·s*	*Cytoplasmatic viscosity, see [34,79].*
adhesion_range	*-0.5·(cell radius)*	*This work, by fitting of tumor cell growth data.*
adhesion_decay	*2.*	*This work, by fitting of tumor cell growth data.*
packing_factor	*0.9047*	*Adimensional correction that takes into account the interstitial volume (linear packing factor for an arrangement of spheres [80,81])*
extension_coeff	*1.1*	*Correction factor that makes cells a little softer (shall be removed in a future version of the program with a better definition of the Poisson's ratio). This work by fitting of tumor cell growth data.*
extvolume_thickness	$1.0 \cdot 10^{-7}$ *m*	*Thickness of extracellular space surrounding each cell. Direct measurements from micrographs of tumor spheroids.*
extvolume_fraction	*0.3*	*This is the fraction of external volume that is actually accessible to diffusing molecules [82-84].*
tph_slope	*2.73*	*This work, by fitting of tumor cell growth data. See also [2, 13-16].*
tph_thr	*6.55*	*This work, by fitting of tumor cell growth data. See also [2, 13-16].*
tp11_slope	*10.91*	*This work, by fitting of tumor cell growth data. See also [2, 13-16].*
tp11_thr	*6.9625*	*This work, by fitting of tumor cell growth data. See also [2, 13-16].*
a2c_slope	*2.42*	*This work, by fitting of tumor cell growth data. See also [2, 13-16].*
a2c_thr	*6.92*	*This work, by fitting of tumor cell growth data. See also [2, 13-16].*
c2a_slope	*2.42*	*This work, by fitting of tumor cell growth data. See also [2, 13-16].*
c2a_thr	*6.92*	*This work, by fitting of tumor cell growth data. See also [2, 13-16].*
a2cA_slope	*2.42*	*This work, by fitting of tumor cell growth data. See also [2, 13-16].*
a2cA_thr	*6.92*	*This work, by fitting of tumor cell growth data. See also [2, 13-16].*
c2aA_slope	*2.42*	*This work, by fitting of tumor cell growth data. See also [2,*

		13-16].
c2aA_thr	*6.92*	*This work, by fitting of tumor cell growth data. See also [2, 13-16].*
Ja2cAcL_slope	*1.5*	*This work, by fitting of tumor cell growth data. See also [2, 13-16].*
a2cAcL_thr	*7.*	*This work, by fitting of tumor cell growth data. See also [2, 13-16].*
c2aAcL_slope	*1.5*	*This work, by fitting of tumor cell growth data. See also [2, 13-16].*
c2aAcL_thr	*7.*	*This work, by fitting of tumor cell growth data. See also [2, 13-16].*

Table S5: Other parameters that at present are hard-coded in the program.

Name	*Value*	*Notes and references*
Diff_W_G	$7 \cdot 10^{-10}\ m^2/s$	*glucose in water [82].*
Diff_ES_G	$2 \cdot 10^{-10}\ m^2/s$	*glucose in the extracellular spaces [82,85].*
Diff_W_A	$3 \cdot 10^{-10}\ m^2/s$	*glutamine in water [82].*
Diff_ES_A	$7 \cdot 10^{-11}\ m^2/s$	*glutamine in the extracellular spaces [86].*
Diff_W_AcL	$3 \cdot 10^{-10}\ m^2/s$	*lactate in water [82].*
Diff_ES_AcL	$1.4 \cdot 10^{-11}\ m^2/s$	*lactate in the extracellular spaces [87].*
Diff_W_O2	$3.2 \cdot 10^{-9}\ m^2/s$	*oxygen in water [48].*
Diff_ES_O2	$7 \cdot 10^{-11}\ m^2/s$	*oxygen in the extracellular spaces. This work, by fitting of tumor cell growth data.*
VISCOSITY_ENV	*1. Pa·s*	*viscosity of the extracellular space [58].*

E. Some considerations on the computational complexity of the program

This kind of simulation is a real computational challenge. Although the present version of the program is not completely optimized, it has been designed with computational complexity in mind. On average, the time complexity of each individual time step is $\approx \mathrm{O}(N)$*, where N is the number of cells, and this is determined by the Delaunay triangulation [88-91].*

However the number of cells grows exponentially, at least in the initial phase of spheroid growth, and thus the computational complexity of each simulation step is proportional to $\exp\left(\frac{t}{T}\ln 2\right)$*, where t is the simulated time and T is the average duplication time of cells. The CPU time* Δt_{CPU} *required to simulate the time span* Δt_{SIM} *is modeled by the expression*

$$\Delta t_{CPU} = \tau_1 \cdot N \ln N + \tau_0 N \qquad \textit{(S.69)}$$

where τ_0 and τ_1 are experimental parameters that we determine from actual simulation runs, and where we introduce a slightly superlinear term – suggested by the maximum complexity of Delaunay triangulations in the plane – to account for a superlinear growth term with respect to N. Mature spheroids slow down their growth rate and we find that at this later stage Δt_{CPU} is roughly proportional to the number of cells:

$$\Delta t_{CPU} \approx \tau_2 N + \Delta t_0 \qquad \textit{(S.70)}$$

where τ_2 and Δt_0 are yet other parameters that we determine from actual runs. This also means that on the whole the total computing time is roughly proportional to N^2.

The actual values of τ_0, τ_1, τ_2, and Δt_0 depend on the simulation parameters: figure S6 shows the CPU time t_{CPU} (s) it takes for one hour of simulated time vs. N, in a run where the precision of the global solution of the problem of diffusion, transport and metabolism is fixed at 1%, and the simulation time step is Δt_{SIM} = 50 s. This run has been carried out on a MacPro computer (with an Intel Xeon 3500/W3520 quad processor at 2.66 GHz – and where a single core has been used, the program is not yet multithreaded). Figure S7 shows the total CPU time vs. N: fitting this curve we can estimate the total CPU time needed to simulate larger spheroids.

F. Snapshots from a simulation with the parameters of section E.

The final supplementary figures are higher-resolution pictures of central slices from a simulation with the parameters listed in the previous section. The figures correspond to different simulated times.

- *figures S8-10: oxygen concentration (color mapping, blue=low concentration, red=high concentration) and flow (yellow arrows, arrow length proportional to flow intensity). Each figure shows a steady inward flow of oxygen.*
- *figures S11-14: extracellular glucose concentration (color mapping, blue=low concentration, red=high concentration) and flow (yellow arrows, arrow length proportional to flow intensity). Initially the flow of extracellular glucose points only inward, but glucose diffusion is slow, and as the spheroid grows and dead cells in the core contract, an internal region with an outward flow of extracellular glucose slowly develops.*
- *figures S15-17: extracellular glutamine concentration (color mapping, blue=low concentration, red=high concentration) and flow (yellow arrows, arrow length proportional to flow intensity). Glutamine behaves much like glucose, and these snapshots show the glutamine flow before and after the development of the split flow.*
- *figure S18: lactate concentration (color mapping, blue=low concentration, red=high concentration) and flow (yellow arrows, arrow length proportional to flow intensity). Lactate always flows outward in the simulation: this is a single snapshot taken after both glucose and glutamine have developed their split flow regime.*
- *figures S19-21: velocity in the plane of the slice (yellow arrows, arrow length proportional to flow intensity). Cells in the core perform complex looping motions, while cells in the viable rim always push outward.*

Short movies showing features of the same central slice are also available as additional supplementary information:

- *S1: development of the necrotic core (red = live cells, black = dead cells).*
- *S2: flow of extracellular glucose (same coding as figures S11-14);*
- *S3: map of projected cell velocities (same coding as figures S19-21).*

References

[1] Chignola R, Milotti E (2005) A phenomenological approach to the simulation of metabolism and proliferation dynamics of large tumor cell populations. Phys. Biol. 2: 8-22.

[2] Chignola R, Del Fabbro A, Dalla Pellegrina C, Milotti E (2007) Ab initio phenomenological simulation of the growth of large tumor cell populations. Phys. Biol. 4: 114-133.

[3] Zetterberg A, Larsson O (1985) Kinetic analysis of regulatory events in G1 leading to proliferation or quiescence of Swiss 3T3 cells. Proc. Natl Acad. Sci. USA 82: 5365-5369.

[4] Milotti E, Del Fabbro A, Chignola R (2009) Numerical integration methods for large-scale biophysical simulations. Comp. Phys. Comm. 180: 2166-2174.

[5] Catlett NL, Weisman LS (2000) Divide and multiply: organelle partitioning in yeast. Curr. Opin. Cell Biol. 12: 509-516.

[6] Bergeland T, Widerberg J, Bakke O, Nordeng TW (2001) Mitotic partitioning of endosomes and lysosomes. Curr. Biol. 11: 644-651.

[7] Milotti E, Del Fabbro A, Dalla Pellegrina C, Chignola R (2008) Statistical approach to the analysis of cell desynchronization data. Physica A 387: 4204-4214.

[8] Johnson LV, Walsh ML, Chen LB (1980) Localization of mitochondria in living cells with rhodamine 123. Proc. Natl. Acad. Sci. USA 77: 990-994.

[9] Lang F, Waldegger S (1997) Regulating cell volume. Am. Sci. 85: 440-447.

[10] Wehner F, Olsen H, Tinel H, Kinne-Saffran E, Kinne RKH (2003) Cell volume regulation: osmolytes, osmolyte transport, and signal transduction. Rev. Physiol. Biochem. Pharmacol. 148: 1-80.

[11] Bortner CD, Cidlowski JA (2002) Apoptotic volume decrease and the incredible shrinking cell. Cell Death Diff. 9: 1307-1310.

[12] Newell K, Franchi A, Pouyssegur J, Tannock I (1993) Studies with glycolysis-deficient cells suggest that production of lactic acid is not the only cause of tumor acidity. Proc. Natl. Acad. Sci. USA 90: 1127-1131.

[13] Kaminskas E (1978) The pH-dependence of sugar transport and of glycolysis in cultured Ehrlich ascites-tumor cells. Biochem. J. 172: 453-459.

[14] Tildon JT, McKenna MC, Stevenson J, Couto R (1993) Transport of L-lactate by cultured rat brain astrocytes. Neurochem. Res. 18: 177-184.

[15] McKenna MC, Tildon JT, Stevenson JH, Hopkins IB, Huang X, Couto R (1998) Lactate transport by cortical synaptosomes from adult rat brain: characterization of kinetics and inhibitor specificity. Dev. Neurosci. 20: 300-310.

[16] Bröer A, Albers A, Setiawan I, Edwards RH, Chaudhry FA, Lang F, Wagner S, Bröer CA (2002) Regulation of the glutamine transporter SN1 by extracellular pH and intracellular sodium ions. J. Physiol. 539: 3-14.

[17] Ezhevsky SA, Ho A, Becker-Hapak M, Davis PK, Dowdy SF (2001) Differential regulation of retinoblastoma tumor suppressor protein by G1 cyclin-dependent kinases complexes in vivo. Mol. Cell Biol. 21: 4773-4784.

[18] Seville LL, Shah N, Westwell AD, Chan WC (2005) Modulation of pRb/E2F functions in the regulation of cell cycle and in cancer cell. Curr. Cancer. Drug Targets 5: 159-170.

[19] Chignola R, Del Fabbro A, Dalla Pellegrina C, Milotti E (2006) Thresholds, long delays and stability from generalized allosteric effect in protein networks. Physica A 371: 463-472.

[20] Milotti E, Del Fabbro A, Dalla Pellegrina C, Chignola R (2007) Dynamics of allosteric action in multisite protein modification. Physica A 379: 133-150.

[21] Chapman JD (2003) Single-hit mechanism of tumor cell killing by radiation. Int. J. Rad. Biol. 79: 71-81.

[22] The Delaunay triangulation and its dual, the Voronoi diagram, bears a strong resemblance to actual cellular structures, and for this reason it has been repeatedly used in models of cell clusters. In addition to standard references on these geometrical structures we include a few references to biological applications that are however just a small sample of the extended literature on this topic.

[23] de Berg M, Cheong O, van Kreveld M, Overmars M (2008) Computational Geometry: Algorithms and Applications. Berlin: Springer Verlag, 3rd edition.

[24] O'Rourke J (1996) Computational Geometry in C. New York: Cambridge Univ. Press, 2nd edition.

[25] Kansal AR, Torquato S, Harsh IV GR, Chiocca EA, Deisboeck TS (2000) Simulated brain tumor growth dynamics using a three-dimensional cellular automaton. J. Theor. Biol. 203: 367-382.

[26] Honda H, Tanemura M, Yoshida A (2000) Differentiation of wing epidermal scale cells in a butterfly under the lateral inhibition model - appearance of large cells in a polygonal pattern. Acta Biotheor. 48: 121-136.

[27] Beyer T, Meyer-Hermann M (2007) Modeling emergent tissue organization involving high-speed migrating cells in a flow equilibrium. Phys. Rev. E 76: 021929.

[28] Li X, Cristini V, Nie Q, Lowengrub JS (2007) Nonlinear three-dimensional simulation of solid tumor growth. Discr. Cont. Dyn. Sys. - Ser. B 7: 581-607.

[29] Gershenfeld N (1999) The nature of mathematical modeling. New York: Cambridge Univ. Press.

[30] See, e.g., Press WH, Teulkosky SA, Vetterling WT, Flannery BP (2007) Numerical Recipes: The Art of Scientific Computing. New York: Cambridge Univ. Press, 3rd ed.

[31] Verdier C (2003) Rheological properties of living materials. From cells to tissues. J. Theor. Med. 5: 67-91.

[32] Discher DE, Boal DH, Boey SK (1988) Simulations of the erythrocyte cytoskeleton at large deformation. II. Micropipette aspiration. Biophys. J. 75: 1584-1597.

[33] Yeung A, Evans E (1989) Cortical shell-liquid core model for passive flow of liquid-like spherical cells into micropipets. Biophys. J. 56: 139-149.

[34] Hochmuth RM, Ting-Beall HP, Beaty BB, Needham D, Tran-Son-Tay R (1993) Viscosity of passive human neutrophils undergoing small deformations. Biophys. J. 64: 1596-1601.

[35] Heinrich V, Ritchie K, Mohandas N, Evans E (2001) Elastic thickness compressibility of the red cell membrane. Biophys. J. 81: 1452-1463.

[36] Bausch AR, Möller W, Sackmann E (1999) Measurement of local viscoelasticity and forces in living cells by magnetic tweezers. Biophys. J. 76: 573-579.

[37] Sleep J, Wilson D, Simmons R, Gratzer W (1999) Elasticity of the red cell membrane and its relation to hemolytic disorders: an optical tweezers study. Biophys. J. 77: 3085-3095.

[38] Radmacher M (1997) Measuring the elastic properties of biological samples with the AFM. IEEE Eng. Med. Biol. Mag. 16: 47-57.

[39] A-Hassan E (1998) et al. Relative microelastic mapping of living cells by atomic force microscopy. Biophys. J. 74: 1564-1578.

[40] Takeuchi M, Miyamoto H, Sako Y, Komizu H, Ksumi A (1998) Structure of the erythrocyte membrane skeleton as observed by atomic force microscopy. Biophys. J. 74: 2171-2183.

[41] Lekka M et al (1999), Local elastic properties of cells studied by SFM. Appl. Surf. Sci. 141: 345-349.

[42] Lekka M et al (1999), Elasticity of normal and cancerous human bladder cells studied by scanning force microscopy. Eur. Biophys. J. 28: 312-316.

[43] Sen S, Subramanian S, Discher DE (2005) Indentation and adhesive probing of a cell membrane with AFM: theoretical model and experiments. Biophys. J. 89: 3203-3213.

[44] Rosenbluth MJ, Lam WA, Fletcher DA (2006) Force microscopy of nonadherent cells: A comparison of leukemia cell deformability. Biophys. J. 90: 2994-3003.

[45] Roca-Cusachs P et al (2006) Rheology of passive and adhesion-activated neutrophils probed by atomic force microscopy. Biophys. J. 91: 3508-3518.

[46] Fukumura D, Jain RK (2007) Tumor microenvironment abnormalities: causes, consequences, and strategies to normalize. J. Cell. Biochem. 101: 937-949.

[47] Palsson E (2001) A three-dimensional model of cell movement in multicellular systems. Future Gen. Comp. Sy. 17: 835-852.

[48] Galbusera F, Cioffi M, Raimondi MT (2008) An in silico bioreactor for simulating laboratory experiments in tissue engineering. Biomed. Microdev. 10: 547-554.

[49] Wei C, Lintilhac PM, Tanguay JJ (2001) An insight into cell elasticity and load-bearing ability. Measurement and theory. Plant Physiol. 126: 1120-1138.

[50] Galle J, Loeffler M, Drasdo D (2005) Modeling the effect of deregulated proliferation and apoptosis on the growth dynamics of epithelial cell populations in vitro. Biophys. J. 88: 62-75.

[51] Zhu C (2000) Kinetics and mechanics of cell adhesion. J. Biomech. 33: 23-33.

[52] Bell G, Dembo M, Bongrand P (1984) Cell adhesion. Competition between nonspecific repulsion and specific bonding. Biophys. J. 45: 1051-1064.

[53] Chandrasekhar S (1943) Stochastic problems in physics and astronomy. Rev. Mod. Phys. 15: 1-89.

[54] Flekkøy EG, Coveney PV, De Fabritiis G (2000) Foundations of dissipative particle dynamics. Phys. Rev. E 62: 2140-2157.

[55] Dzwinel W, Yuen DA, Boryczko K (2002) Mesoscopic dynamics of colloids simulated with dissipative particle dynamics and fluid particle model. J. Mol. Model. 8: 33-43.

[56] Butcher JC (2008) Numerical methods for ordinary differential equations. Chichester: Wiley.

[57] Ascher U, Ruuth S, Spiteri RJ (1997) Implicit-explicit Runge-Kutta methods for time dependent partial differential equations. Appl. Numer. Math. 25: 151-167.

[58] Maleki A, Kjøniksen A-L, Nyström B (2007) Anomalous viscosity behavior in aqueous solutions of hyaluronic acid. Polym. Bull. 59: 217-226.

[59] Newman S, Cloître M, Allain C, Forgacs G, Beysens D (1997) Viscosity and elasticity during collagen assembly in vitro: relevance to matrix-driven translocation. Biopolymers 41: 337-347.

[60] Regina A, Roux F, Revest PA (1997) Glucose transport in immortalized rat brain capillary endothelial cells in vitro: transport activity and GLUT1 expression. Biochim. Biophys. Acta 1335: 135-143.

[61] Heimberg H et al (1996) The glucose sensor protein glucokinase is expressed in glucagon-producing alfa-cells. Proc. Natl. Acad. Sci. USA 93: 7036-7041.

[62] Mazurek S, Zwerschke W, Jansen-Dürr P, Eigenbrodt E (2001) Effects of the human papilloma virus HPV-16 E7 oncoprotein on glycolysis and glutaminolysis: role of pyruvate kinase type M2 and the glycolytic-enzyme complex. Biochem. J. 356: 247-256.

[63] Levintow L, Eagle H, Piez KA (1955) The role of glutamine in protein biosynthesis in tissue culture. J. Biol. Chem. 215: 441-460.

[64] Salzman NP, Eagle H, Sebring ED (1958) The utilization of glutamine, glutamic acid, and ammonia for the biosynthesis of nucleic acid bases in mammalian cell cultures. J. Biol. Chem. 230: 1001-1012.

[65] Voet D, Voet J (2002) Biochemistry New York: Wiley, 2nd ed.

[66] Robin ED, Wong R (1988) Mitochondrial DNA molecules and virtual number of mitochindria per cell in mammalian cells. J. Cell Physiol. 136: 507-513.

[67] James TW, Bohman R (1981) Proliferation of mitochondria during the cell cycle of the human cell line (HL-60). J. Cell Biol. 89: 256-260.

[68] Masafumi W, Wang HS, Okada A (2002) Characterization of L-glutamine transport by human neuroblastoma cell line. Am. J. Physiol. Cell. Physiol. 282: C1246-C1253.

[69] Rodriguez-Enriquez S, Torres-Marquez ME, Moreno-Sanchez R (2000) Substrate oxydation and ATP supply in AS-300 hepatoma cells. Arch. Biochem. Biophys. 375: 21-30.

[70] Porwol T, Merten E, Opitz N, Acker H (1996) Three-dimensional imaging of rodhamine 123 fluorescence distribution in human melanoma cells by means of confocal laser scanning microscopy. Acta Anat. (Basel) 157: 116-125.

[71] Halestrap AP, Price NT (1999) The proton-linked monocarboxylate transporter (MCT) family: structure, function and regulation. Biochem. J. 343: 281-299.

[72] Spencer TL, Lehninger AL (1976) L-lactate transport in Erlich ascites-tumour cells. Biochem. J. 154: 405-414.

[73] von Grumbckow L, Elsner P, Hellsten Y, Quistroff B, Juel C (1999) Kinetics of lactate and pyruvate transport in cultured rat myotubes. Biochim. Biophys. Acta 1417: 267-275.

[74] Clare PM et al (2001) The cyclin-dependent kinases cdk2 and cdk5 act by a random anticooperative kinetic mechanism. J. Biol. Chem. 276: 48292-48295.

[75] Bertoni-Freddari C et al (2007) Preservation of mitochondrial volume homeostasis at the early stages of age-related synaptic deterioration. Ann. N.Y. Acad. Sci. 1096: 138-146.

[76] a very readable introductory text on elasticity theory is ch. 38 in Feynman RP, Leighton RB, Sands M (1964) The Feynman Lectures on Physics, vol. 2, Reading: Addison-Wesley.

[77] Ng CE, Inch WR (1978) Comparison of the densities of clonogenic cells from EMT6 fibrosarcoma monolayer cultures, multicell spheroids, and solid tumors in ficoll density gradients. J. Natl. Cancer Inst. 60: 1017-1022.

[78] Nilsson B, Olofsson T (1985) Density distribution of chronic myeloid leukaemia and normal colony-forming cells in diffusion chambers (CFU-D) and agar (CFU-GM). Scand. J. Haematol. 34: 317-322.

[79] Evans E, Yeung A (1989) Apparent viscosity and cortical tension of blood granulocytes determined by micropipet aspiration. Biophys. J. 56: 151-160.

[80] Sloane NJA (1998) The Sphere Packing Problem. Documenta Mathematika, III: 387-396.

[81] Sloane NJA (1998) Kepler's Conjecture Confirmed. Nature 395: 435-436.

[82] Jain RK (1987) Transport of Molecules in the Tumor Interstitium: A Review. Cancer Res. 47: 3039-3051.

[83] Krol A, Maresca J, Dewhirst MW, Yuan F (1999) Available Volume Fraction of Macromolecules in the Extravascular Space of a Fibrosarcoma: Implications for Drug Delivery. Cancer Res. 59: 4136-4141.

[84] Kim YR, Savellano MD, Savellano DH, Weissleder R, Bogdanov Jr. A (2004) Measurement of Tumor Interstitial Volume Fraction: Method and Implication for Drug Delivery, Magnetic Resonance in Medicine 52: 485-494.

[85] Casciari JJ, Sotirchos SV, Sutherland RM (1988) Glucose Diffusivity in Multicellular Tumor Spheroids, Cancer Res. 48: 3905-3909.

[86] Nielsen TA, DiGregorio DA, Angus Silver R (2004) Glutamate Mobility Reveals the Mechanism Underlying Slow-Rising AMPAR EPSCs and the Diffusion Coefficient in the Synaptic Cleft. Neuron 42: 757-771.

[87] Vega C, Poitry-Yamate CL, Jirounek P, Tsacopoulos M, Coles JA (1998) Lactate Is Released and Taken Up by Isolated Rabbit Vagus Nerve During Aerobic Metabolism, J. Neurochem. 71: 330-337.

[88] Dwyer RA (1989) Higher-dimensional Voronoi diagrams in linear expected time. In Proc. 5th Annu. ACM Sympos. Comput. Geom., 326-333.

[89] Dwyer RA (1991) Higher-dimensional Voronoi diagrams in linear expected time. Discr. and Comp. Geom. 6: 343-367.

[90] Guibas LJ, Knuth DE, Sharir M (1992), Randomized incremental construction of Delaunay and Voronoi diagram. Algorithmica 7: 381-413.

[91] We use the randomized incremental construction of reference [90] as implemented in the computational geometry library CGAL (http://www.cgal.org).

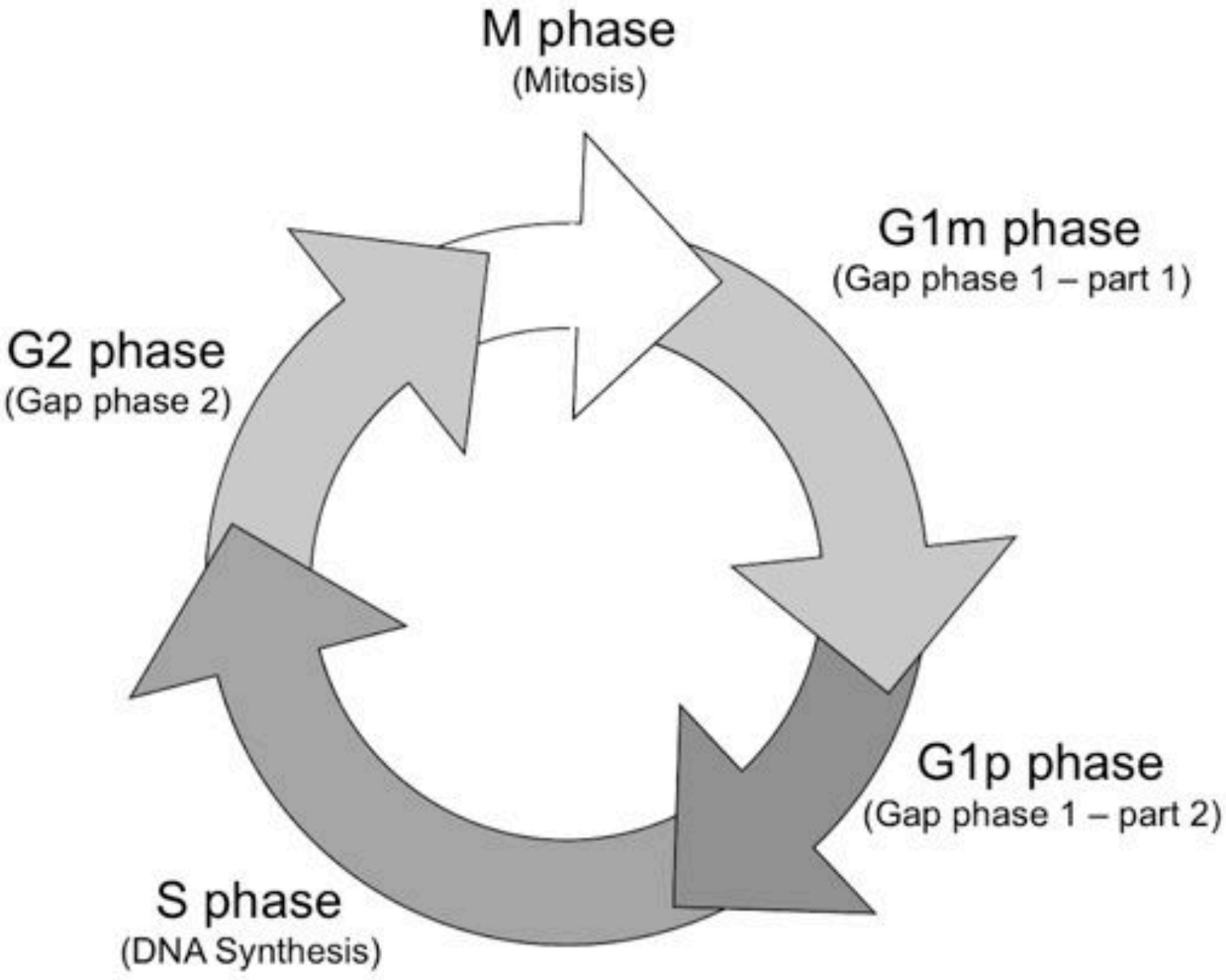
M phase
(Mitosis)
G1m phase
(Gap phase 1 – part 1)
G2 phase
(Gap phase 2)
G1p phase
(Gap phase 1 – part 2)
S phase
(DNA Synthesis)

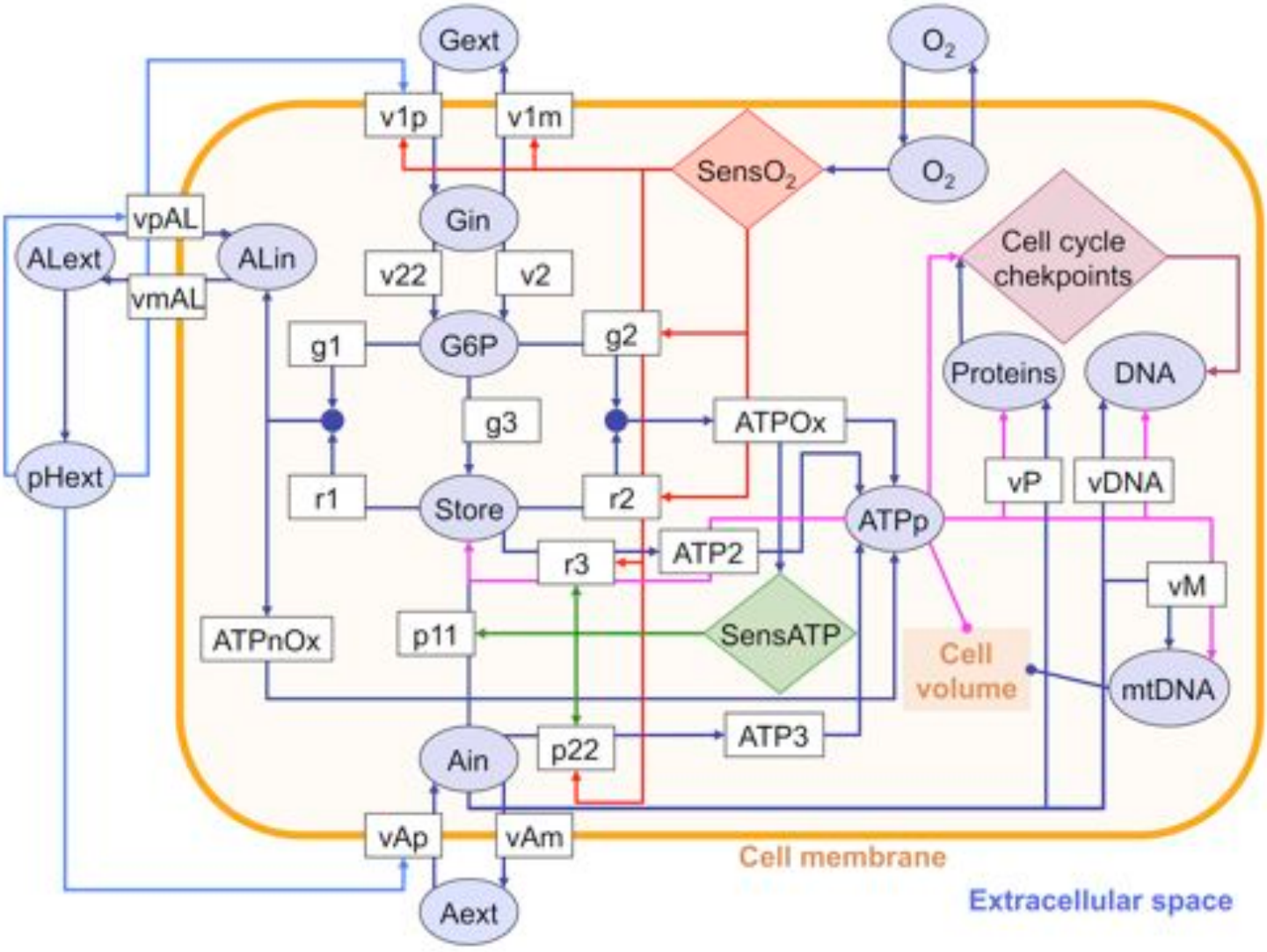
Gext
O2
v1p
v1m
SensO2
O2
vpAL
Gin
Cell cycle chekpoints
ALext
ALin
v22
v2
vmAL
g1
G6P
g2
Proteins
DNA
g3
ATPOx
pHext
vP
vDNA
r1
Store
r2
ATPp
r3
ATP2
vM
ATPnOx
p11
SensATP
Cell volume
mtDNA
Ain
p22
ATP3
vAp
vAm
Cell membrane
Extracellular space
Aext

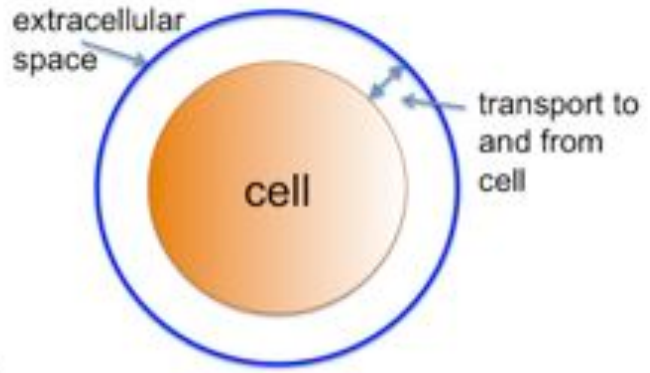

A

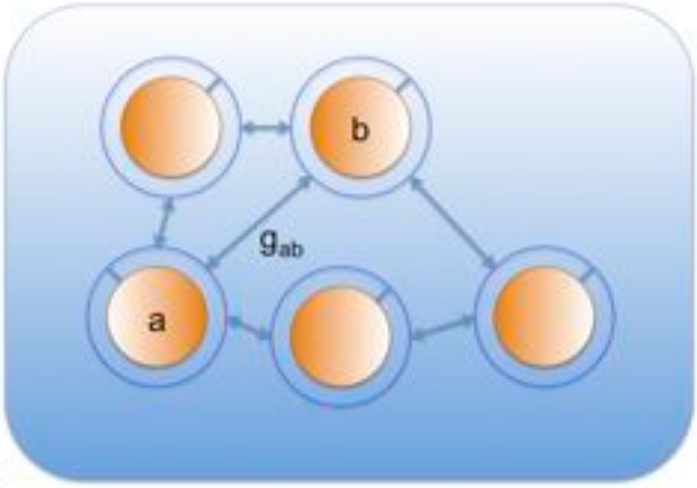

B

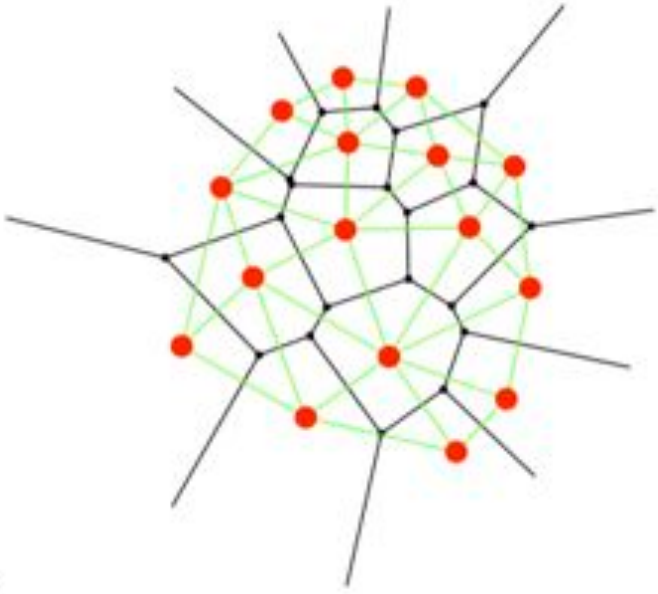

C

D

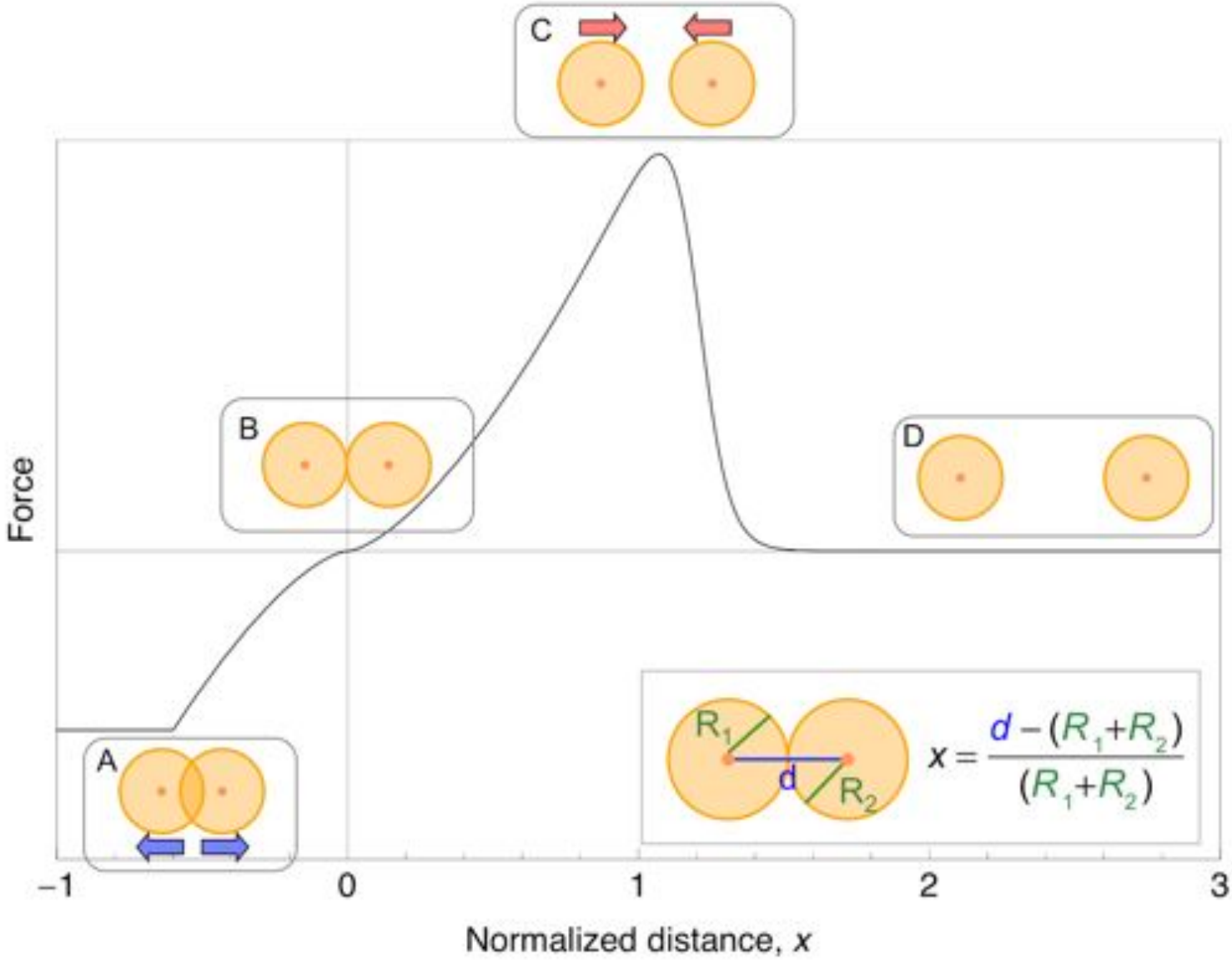
C
B
D
A
Force
−1
0
1
2
3
Normalized distance, x
R1
d
R2
x = d − (R1+R2) / (R1+R2)

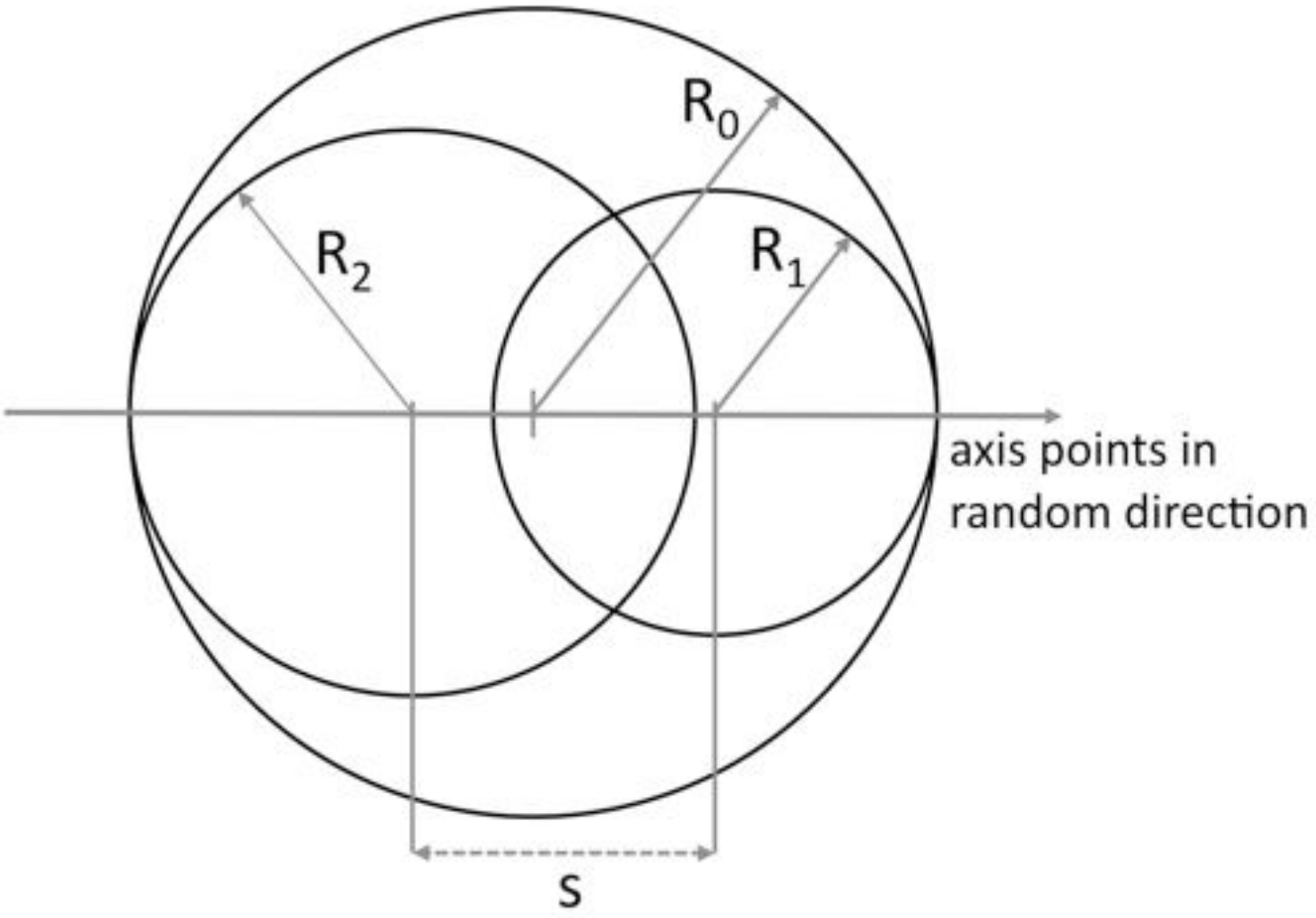
R0
R2
R1
axis points in
random direction
s

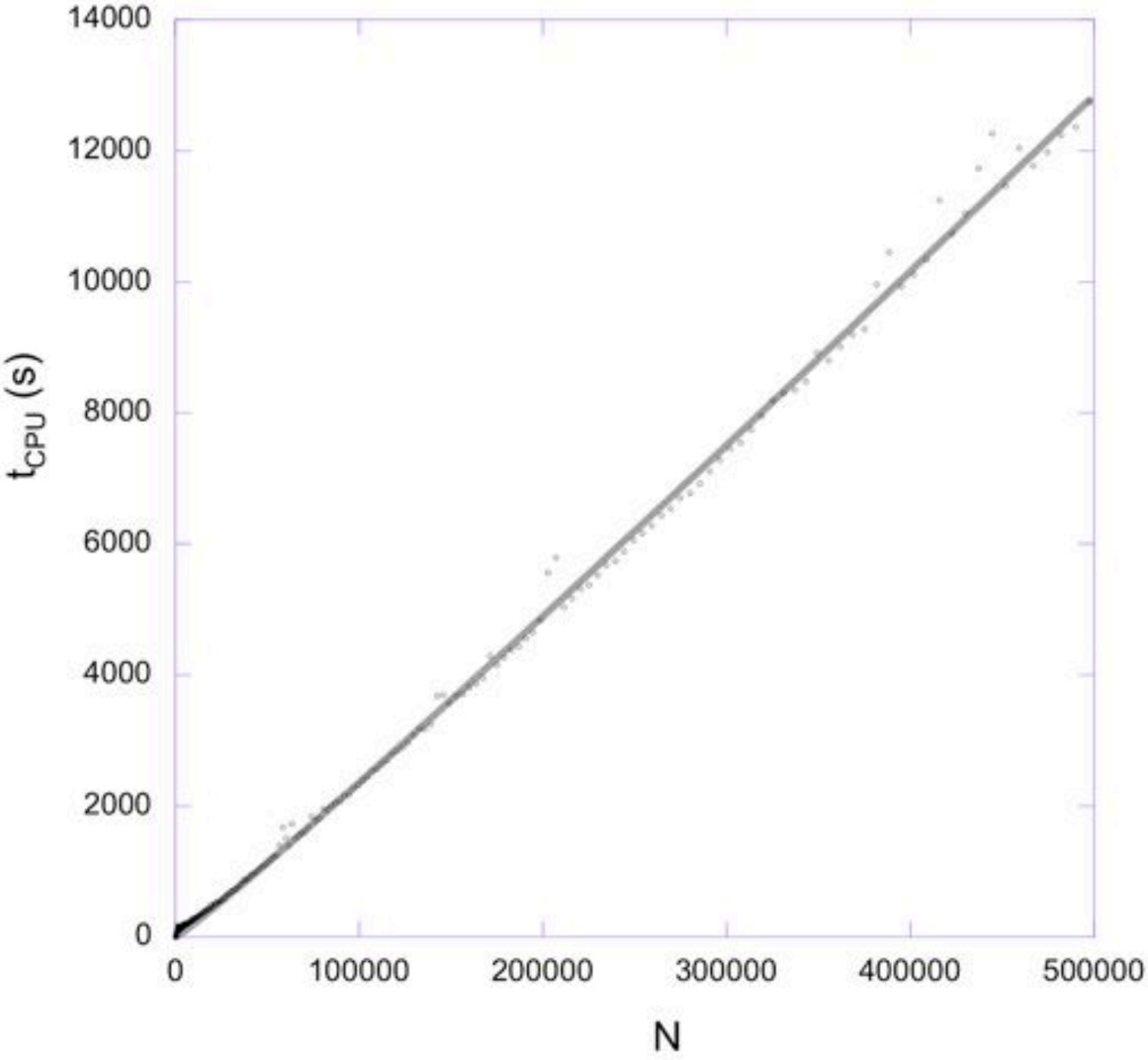
14000
12000
10000
8000
6000
4000
2000
0
t_{CPU} (s)
0
100000
200000
300000
400000
500000
N

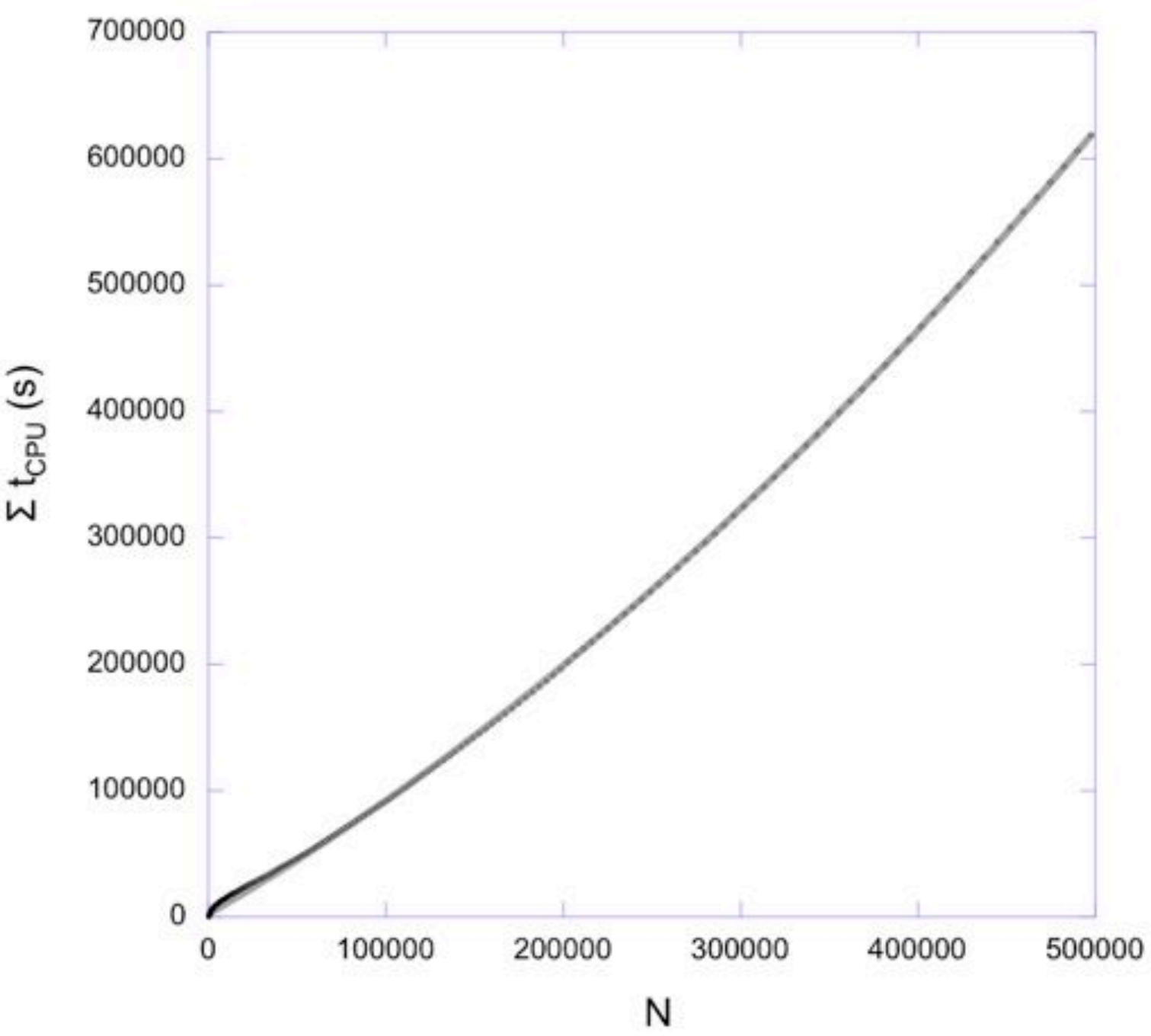
700000
600000
500000
400000
300000
200000
100000
0
Σ t_CPU (s)
0
100000
200000
300000
400000
500000
N

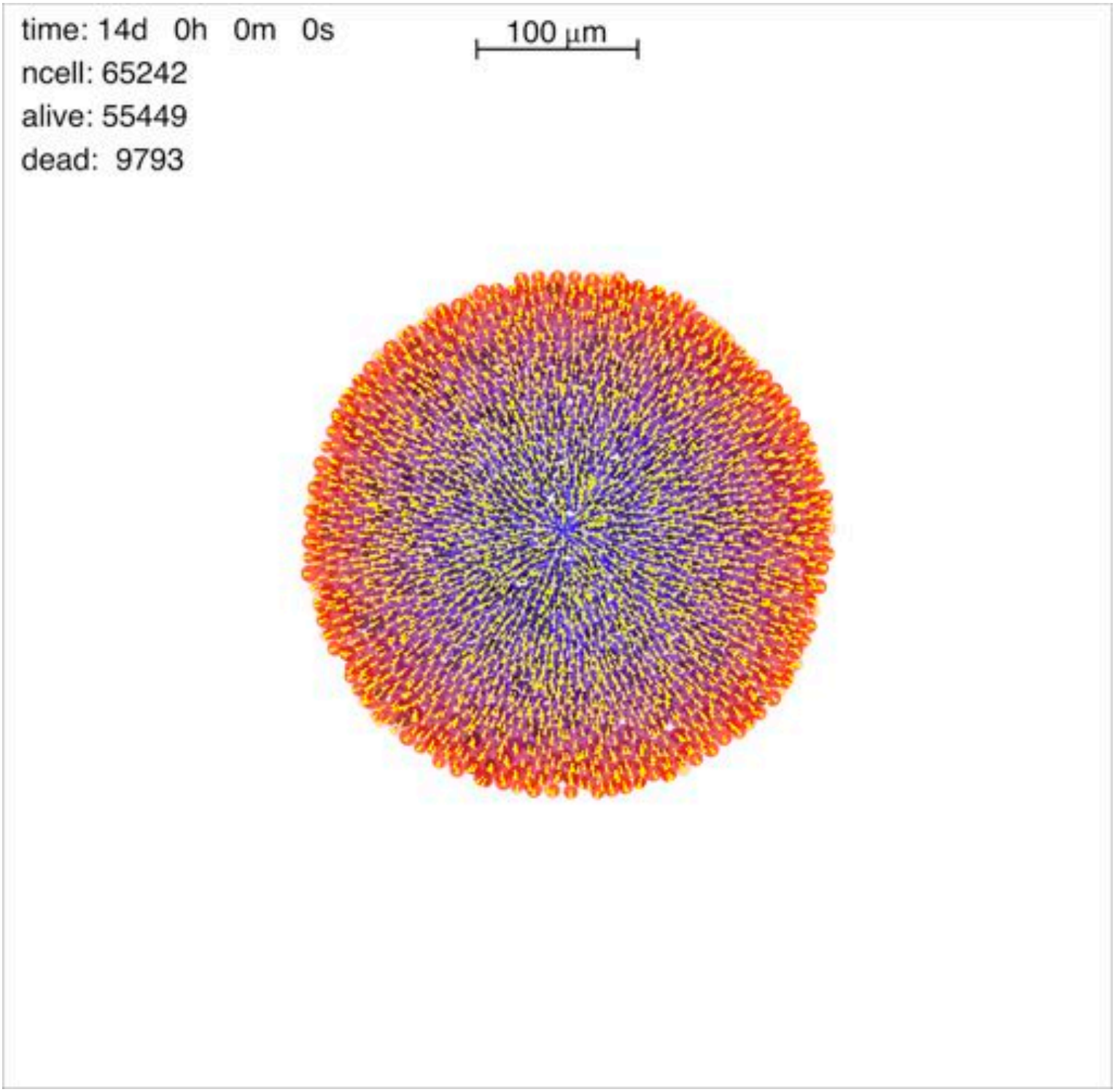
time: 14d 0h 0m 0s
ncell: 65242
alive: 55449
dead: 9793
100 μm

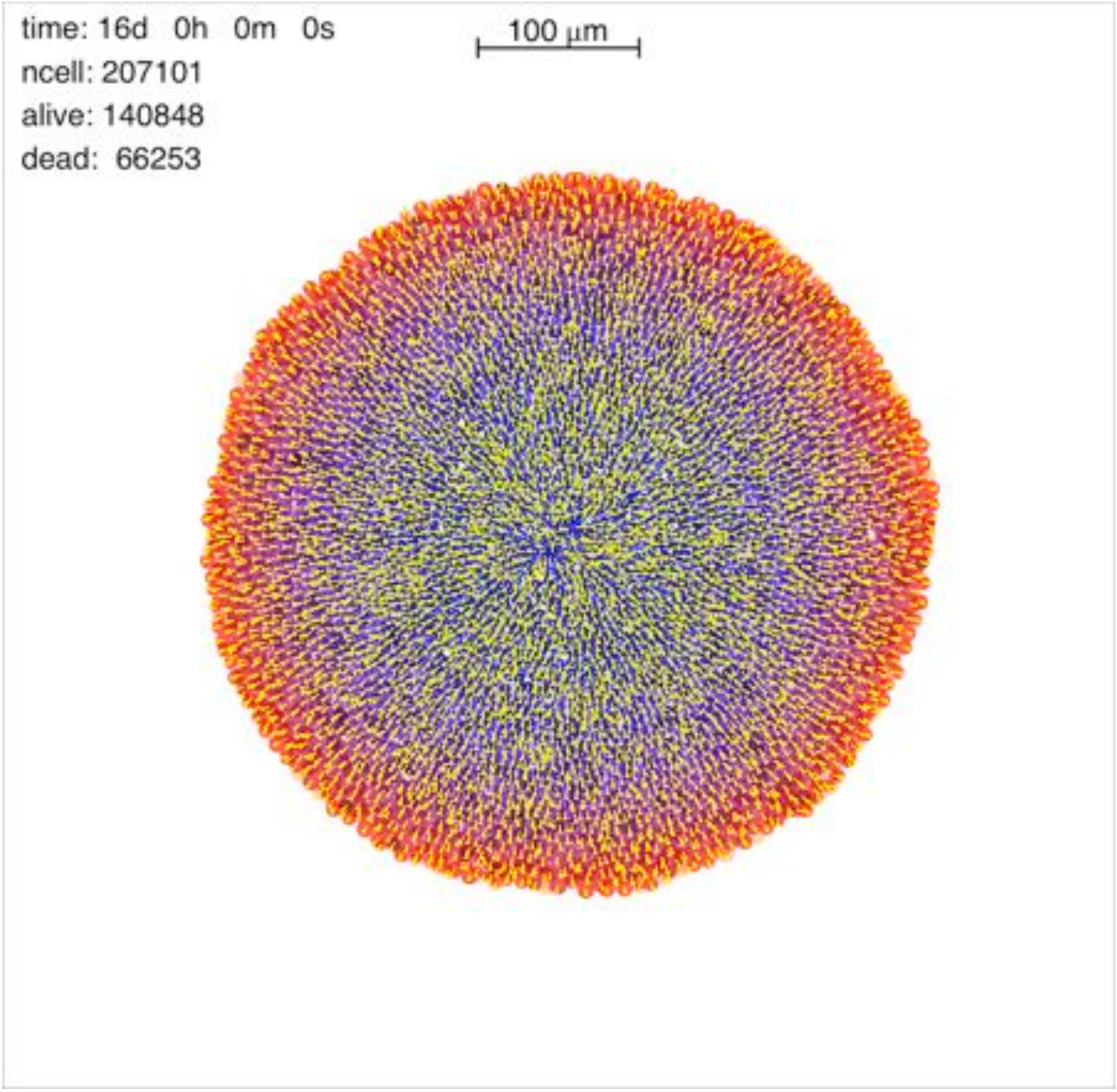
time: 16d 0h 0m 0s
ncell: 207101
alive: 140848
dead: 66253
100 μm

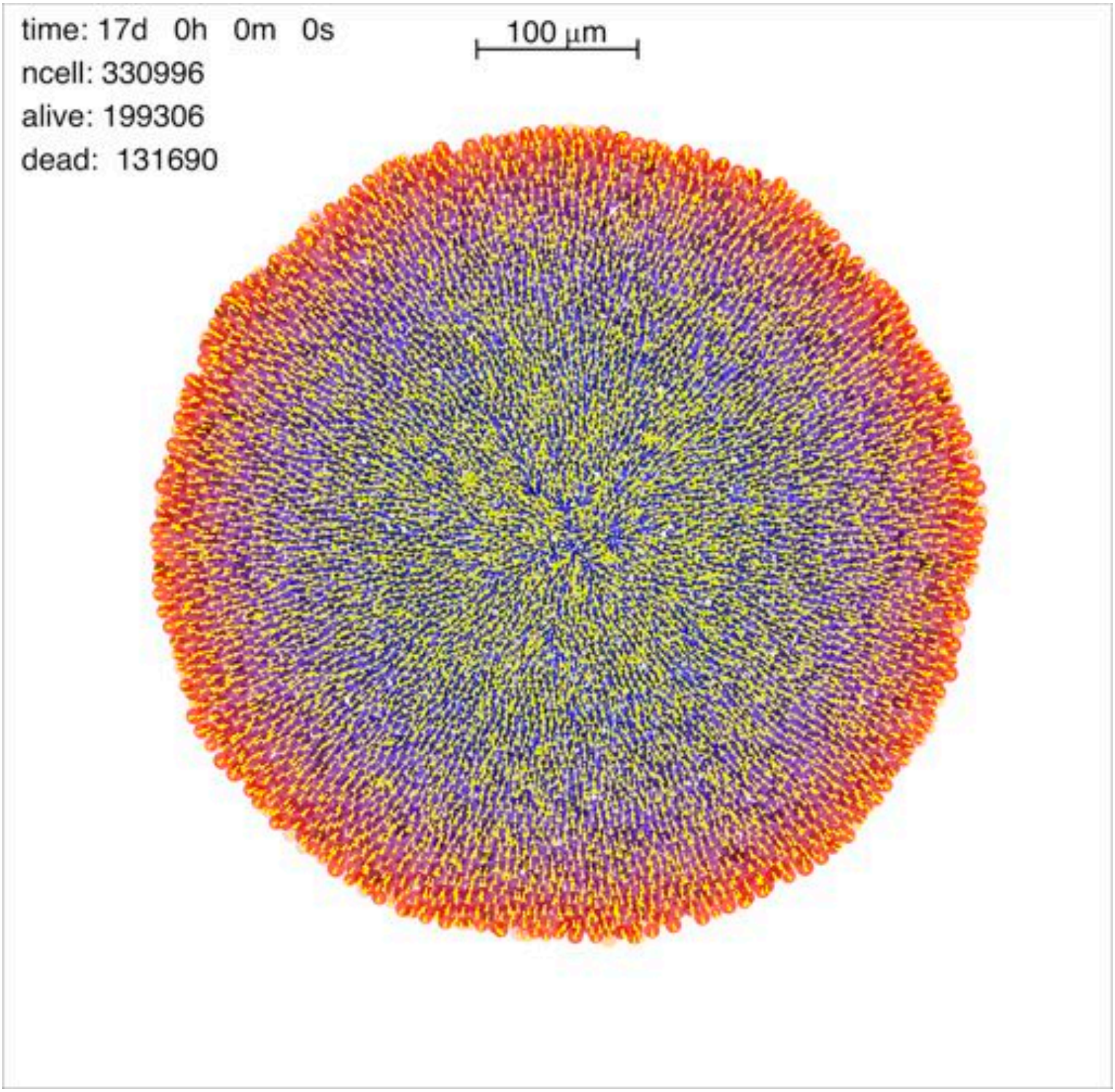
time: 17d 0h 0m 0s
ncell: 330996
alive: 199306
dead: 131690
100 μm

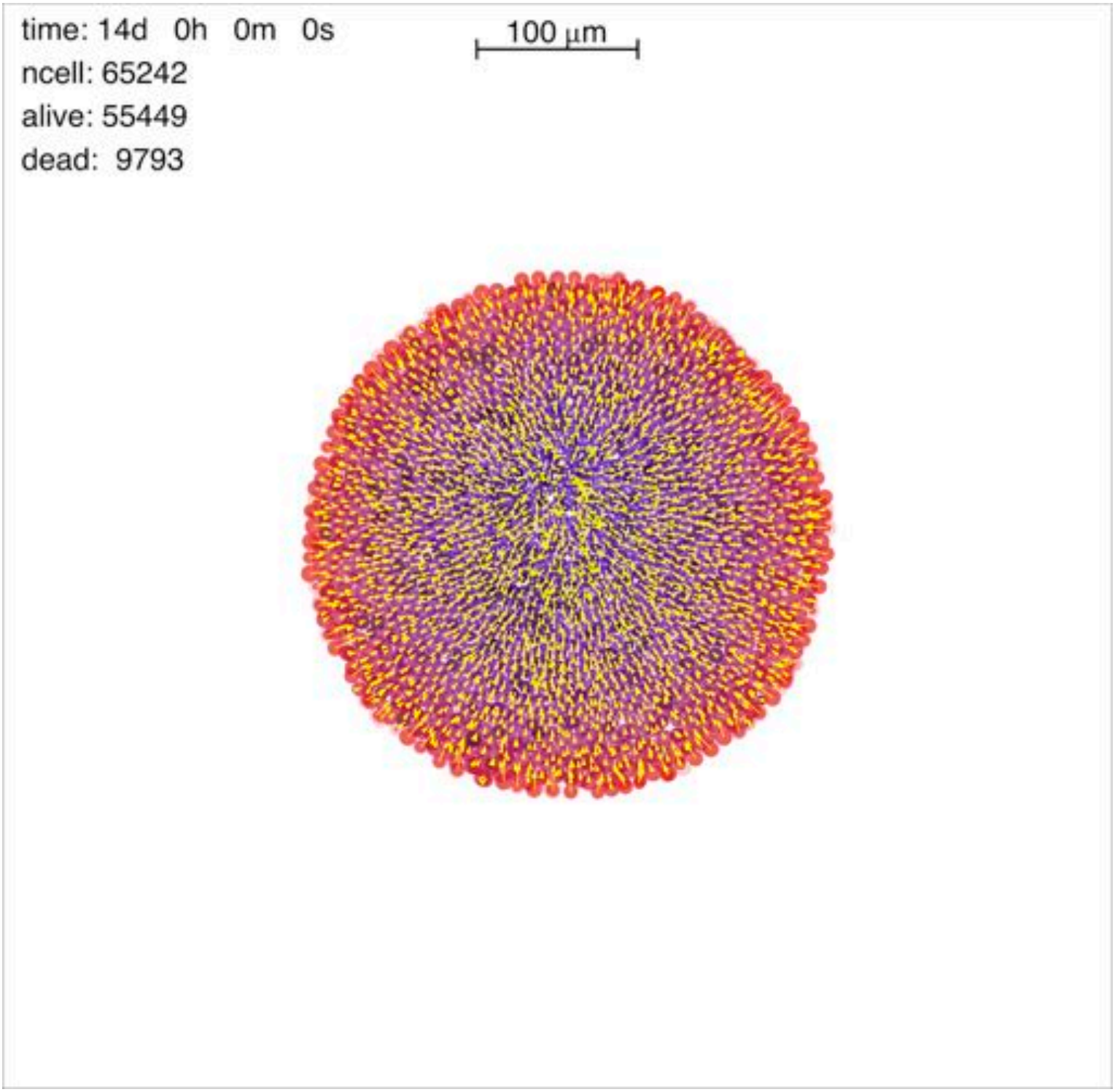
time: 14d 0h 0m 0s
ncell: 65242
alive: 55449
dead: 9793
100 μm

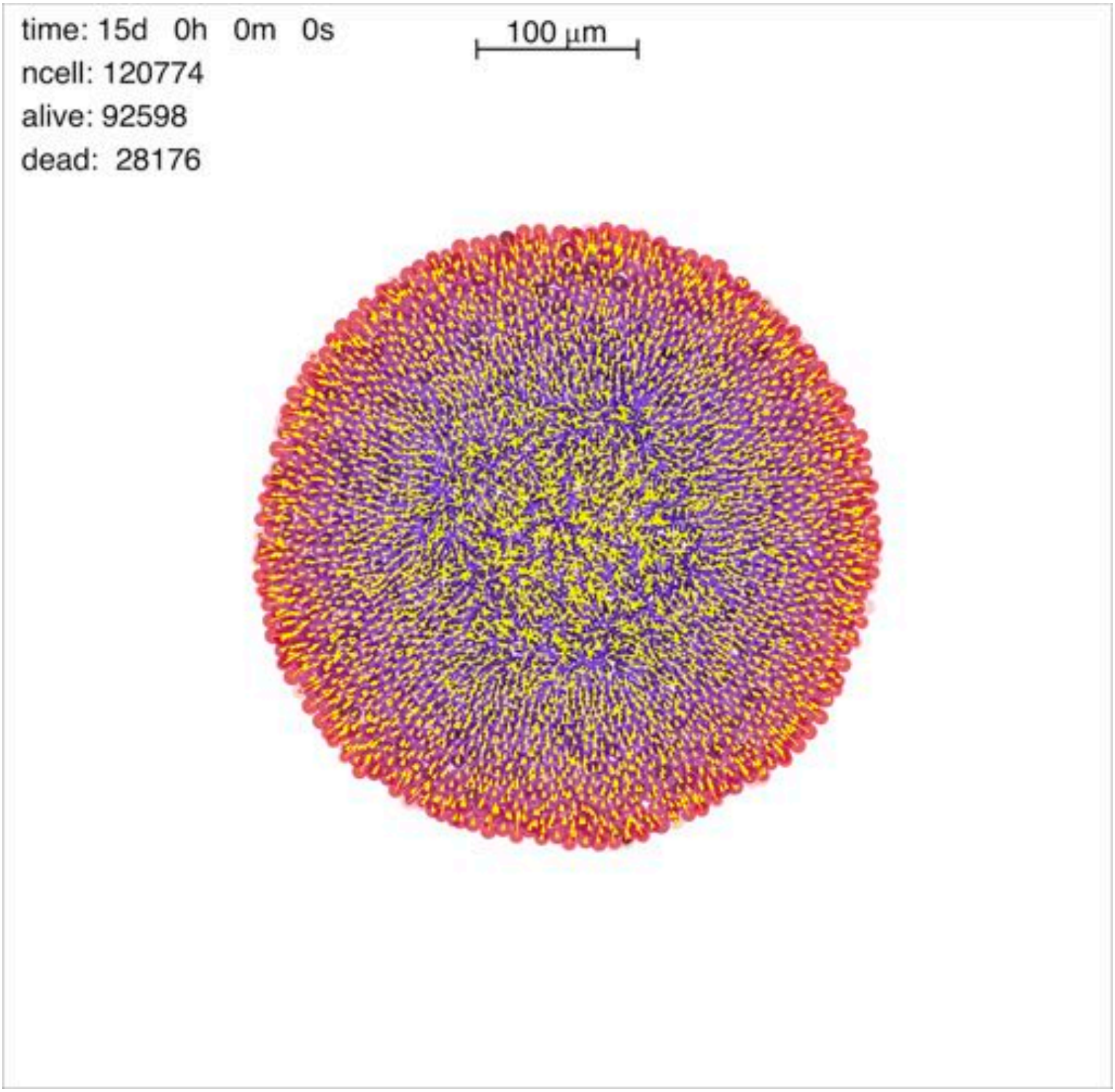
time: 15d 0h 0m 0s
ncell: 120774
alive: 92598
dead: 28176
100 μm

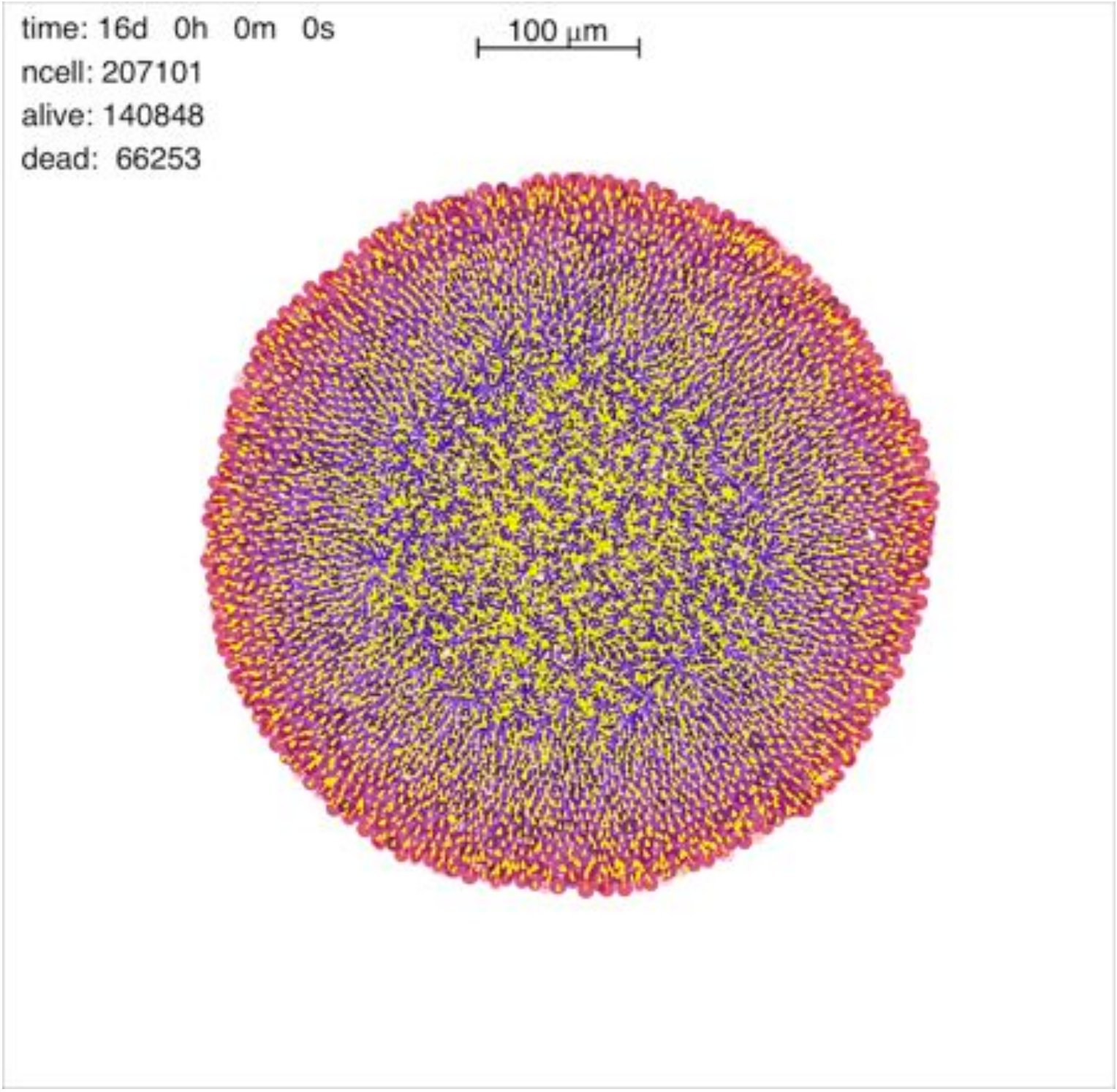
time: 16d 0h 0m 0s
ncell: 207101
alive: 140848
dead: 66253
100 μm

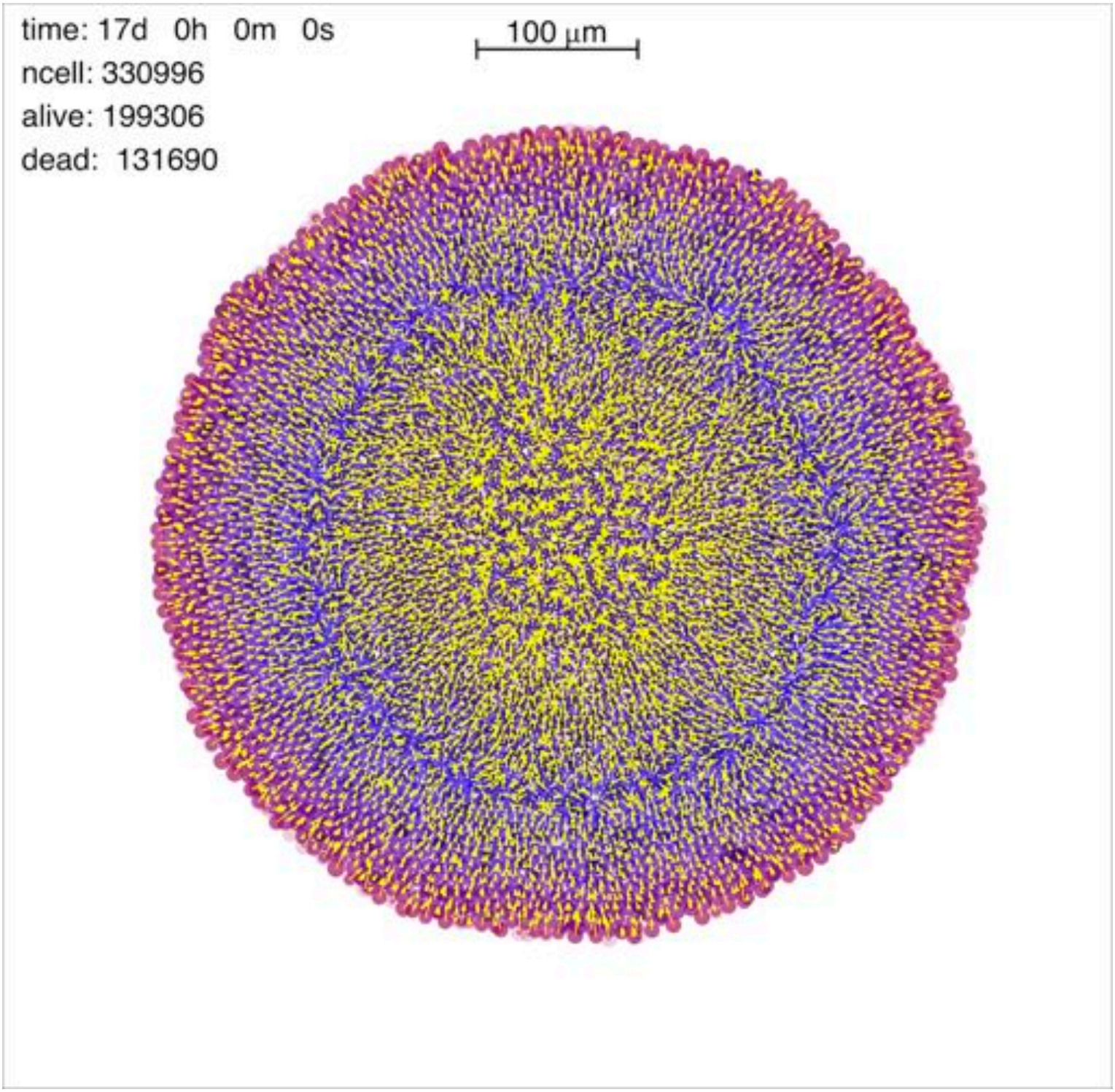
time: 17d 0h 0m 0s
ncell: 330996
alive: 199306
dead: 131690
100 μm

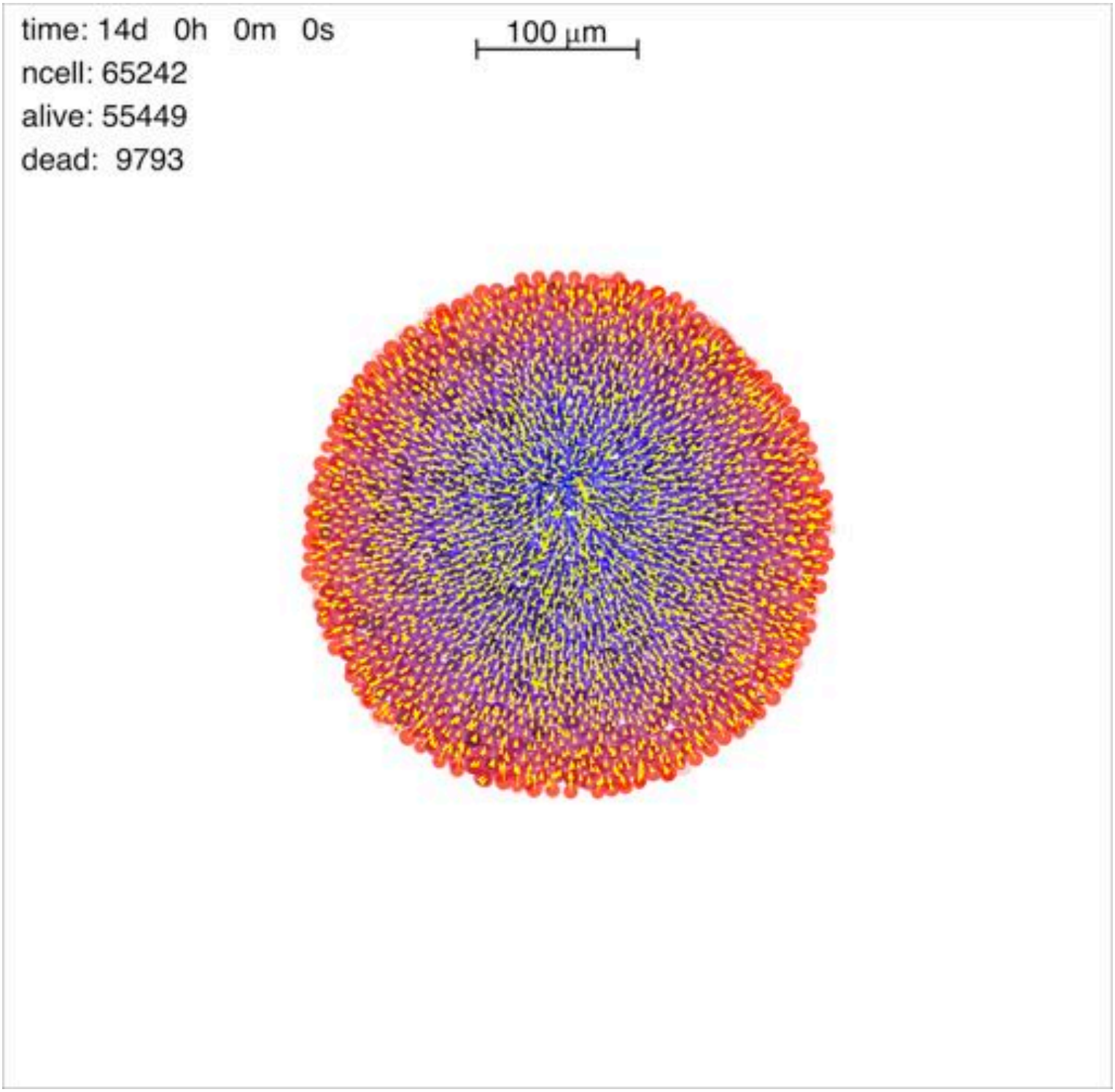
time: 14d 0h 0m 0s
ncell: 65242
alive: 55449
dead: 9793
100 µm

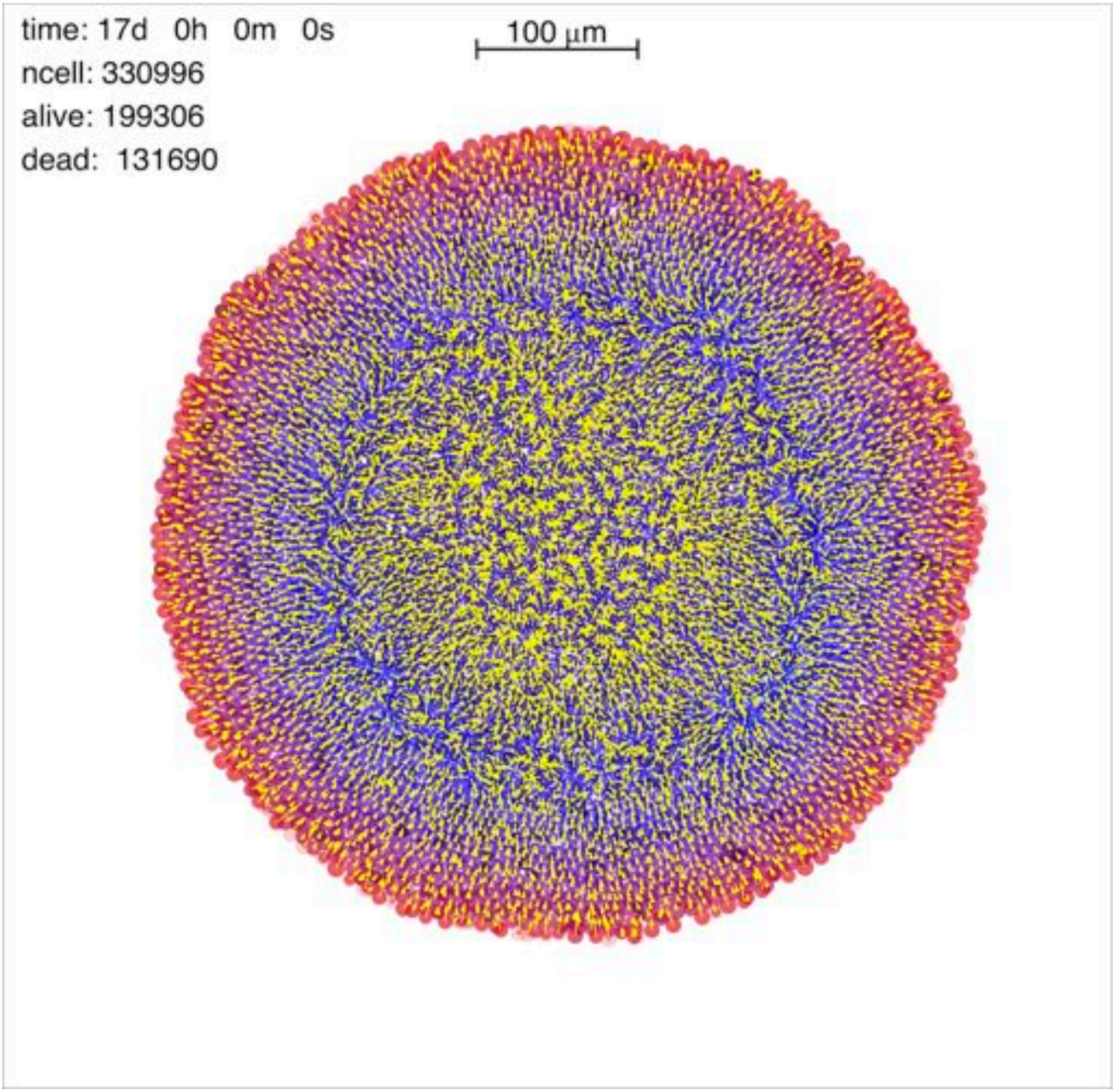
time: 17d 0h 0m 0s
ncell: 330996
alive: 199306
dead: 131690
100 µm

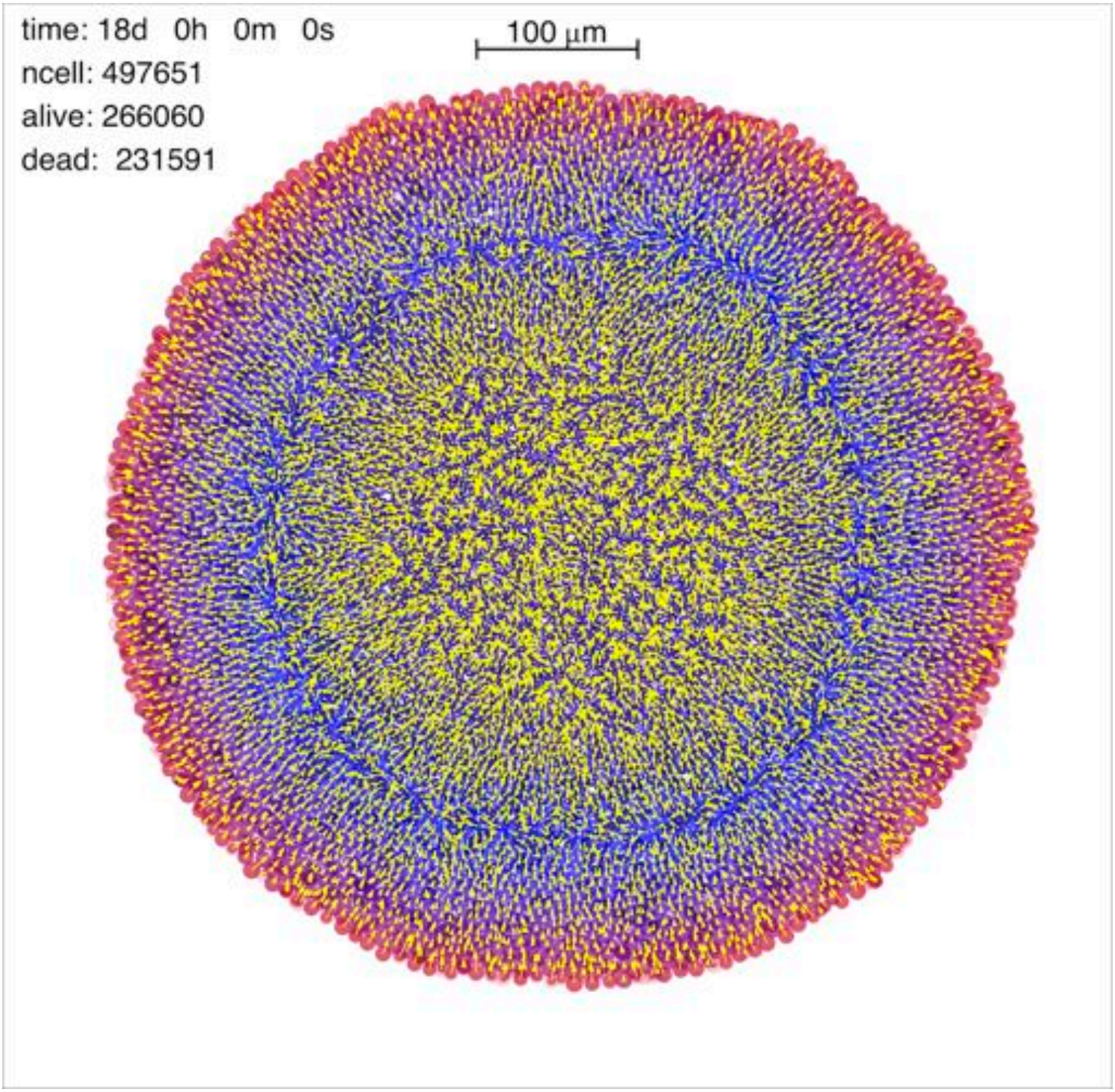
time: 18d 0h 0m 0s
ncell: 497651
alive: 266060
dead: 231591
100 μm

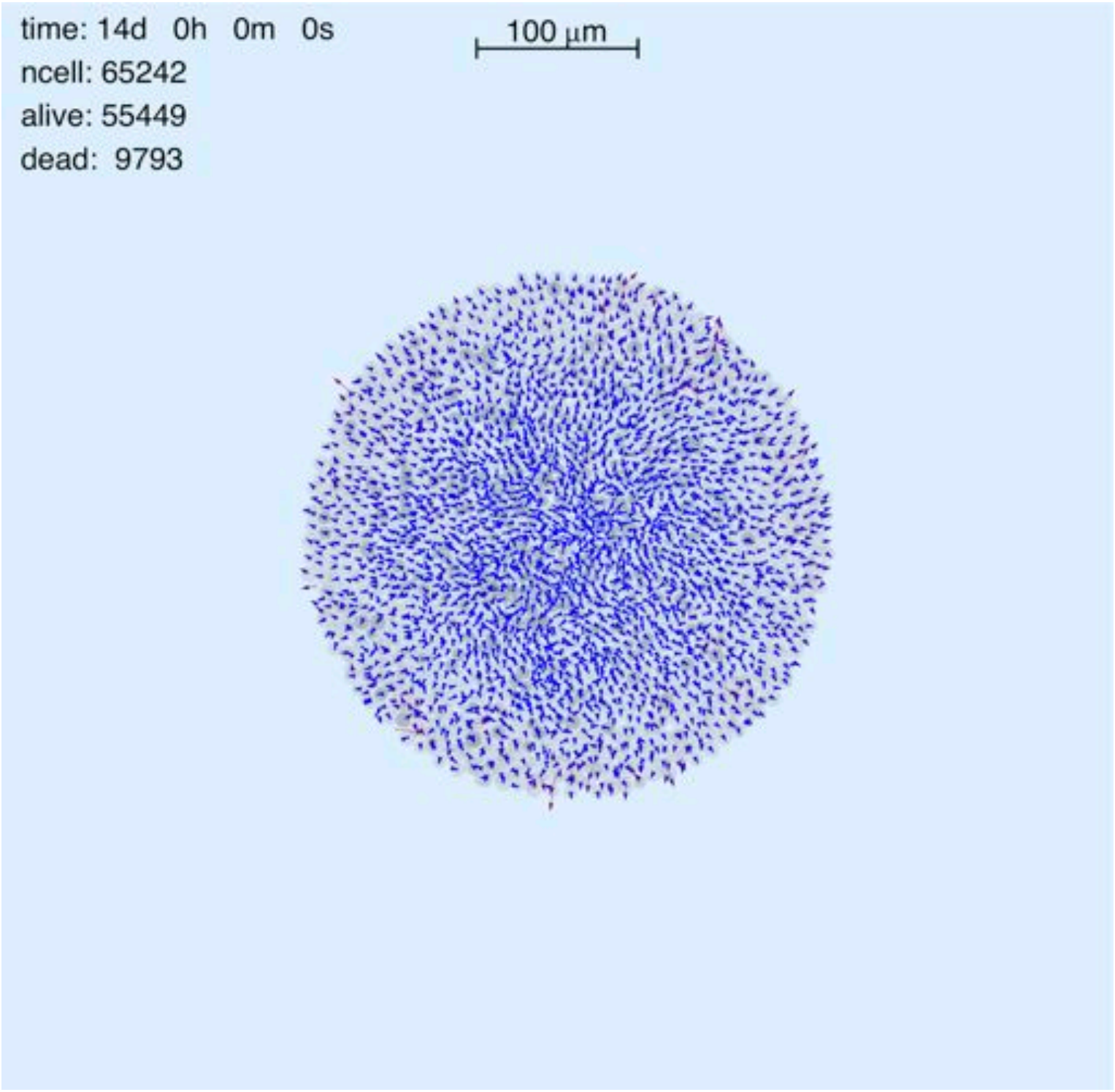
time: 14d 0h 0m 0s
ncell: 65242
alive: 55449
dead: 9793
100 µm

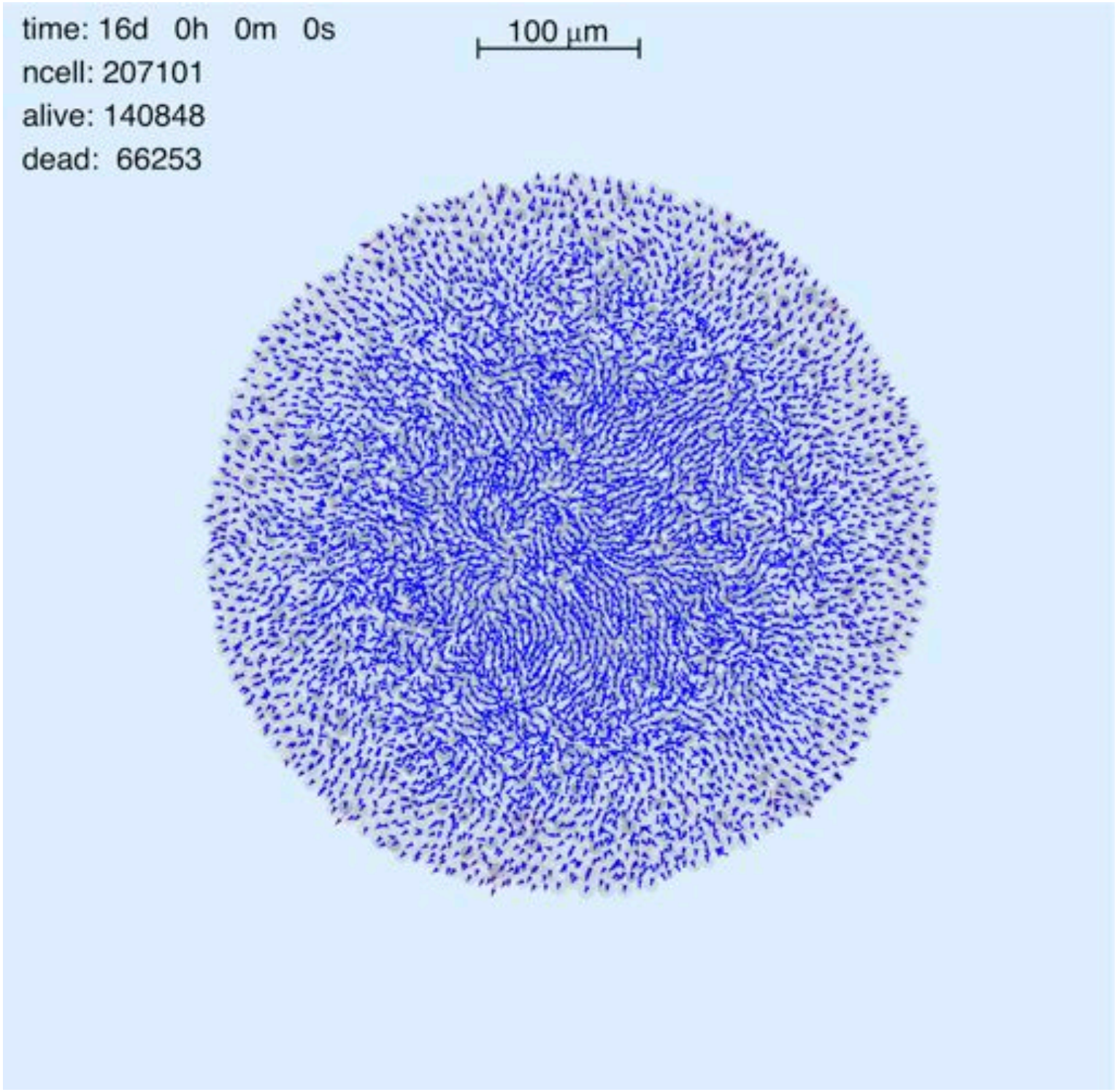
time: 16d 0h 0m 0s
ncell: 207101
alive: 140848
dead: 66253
100 μm

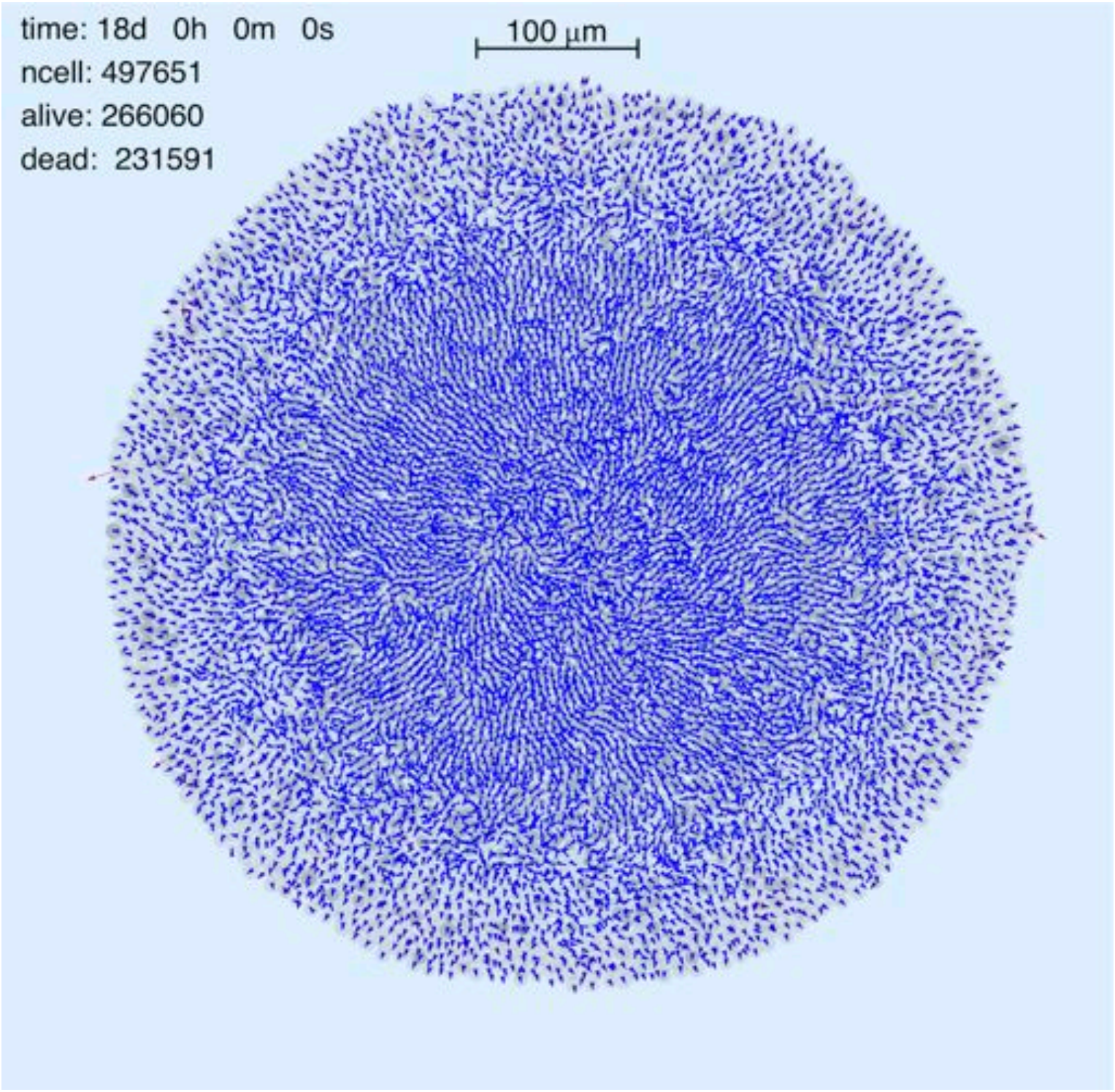
time: 18d 0h 0m 0s
ncell: 497651
alive: 266060
dead: 231591
100 μm